CHARACTERIZATION AND STABILITY OF GOLD NANOCAGES FOR USE AS CONTRAST AGENTS IN OPTOACOUSTICS

BY

SHIV VEER SINGH

A Thesis

Submitted to the Graduate Faculty

in Partial Fulfillment of the Requirements

for the Degree of

MASTER OF SCIENCE

Molecular and Macromolecular Sciences

Departments of Physics and Chemistry

Faculty of Science

University of Prince Edward Island

Abstract

Optoacoustic (OA) imaging is a new technique for cancer detection and non-invasive monitoring of cancer therapeutics. This technique is the combination of both optical and ultrasound modalities, in which tissue is irradiated with nanosecond laser pulses. The delivered optical energy is absorbed and converted into heat, leading to thermaoelastic expansion, which produces acoustic waves. Generated sound waves are then detected by ultrasonic transducers to form an image. In order to enhance optoacoustic signals in tissues, gold nanocages (AuNCs) can be used as contrast agents due to their tuneable optical properties in the near infrared region. Gold nanoparticles are biocompatible and their surface chemistry is well known, therefore they can be easily functionalized to targeting specific cells.

This work involved three linked investigations involving the synthesis, stability testing and optoacoustic contrast capabilities of AuNCs. Silver nanocubes were synthesized to be used as templates for AuNCs synthesis. More then 95% purity was required but only 20-30% purity was achieved in our experiments due to the sensitivity of the reaction. Gold nanocages of 40-45nm were acquired from Dr. Younan Xia (Georgia Tech).

For all OA investigations the system consisted of a Nd:YAG pumped Ti:S laser, which can operate at either 775 nm or 1064 nm, an 8 element annular array transducer with 5 MHz central frequency and bifurcated optic fibre bundles to introduce light to the target. A 6 ns pulse duration and 10 Hz repetition rate were used.

For the stability study, different pulse energies (5mJ, 10mJ) were used and at each energy, three different AuNCs concentrations were exposed for 1 min, 3 min and 5 min. Optical absorption measurements and TEM imaging confirmed conformational changes in AuNCs at both energies. For contrast investigations, three different AuNCs concentrations (8.0 X 10^{11} particles/ml, 2.7 X 10^{11} particles/ml and 1.6 X 10^{11} particles/ml) were tested against fluence, of 0.016 J/cm^2 at 775nm using seven 1% Intralipid phantoms with different background absorption, μ_a (0.03cm^{-1}, 0.1 cm^{-1}, 0.5 cm^{-1}, 1.0 cm^{-1}, 1.5 cm^{-1}, 2.0 cm^{-1}, 4.0 cm^{-1}). For the proof of principle study, pork loin tissues of 5mm 10mm thickness were used as background phantoms. A single AuNCs concentration (2.66 X 10^{11} particles/ml) and 9.2mJ laser energy (0.014 J/cm^2) at 775nm was used. Results demonstrate that AuNCs show relevant contrast, even at the highest absorbing background (4.0 cm^{-1}) and for the maximum pork loin thickness (10mm) tested. Results from 1% Intralipid also demonstrate that there were no conformational changes in AuNCs after the illumination. Therefore, the contrast study indicates that AuNCs could be used as contrast agents by knowing specific parameters, such as background optical properties, AuNCs concentration and required laser fluence.

Acknowledgements

It is a great pleasure to thank those who made this dissertation possible. First and foremost, I would like to show my gratitude to my supervisor, Dr William Whelan, for all of his support over the past three years. I have had the opportunity to gain experience in a wide spectrum of research and academics, thanks to the doors he has opened. Without his support, this dissertation would not have been possible. I sincerely thank him for believing in me and giving me invaluable guidance, stimulating suggestion, and encouragement, which motivated me throughout this research process. I am not from physics background but he gave me confidence to achieve the goals of this research work. Actually, I cannot thank him enough for what he has done for me in the past three years. Thank you, Dr. Whelan for all your support.

Many thanks to my co-supervisor Dr. Rabin Bissessur for all the help on the chemistry side of this project. I am thankful for both the use of his laboratory and equipment, as well as his guidance in the experimental, technical, and academic aspects required for this thesis. I would also like to thanks my supervisory committee members, Dr. Serge Grabtchak and Dr. Brian Wagner, for their support and advises whenever I required throughout the length of this degree. I really appreciate the time and effort they both put in reading and providing comments on this thesis. Thank you to my external examiner, Dr. William Montelpare, for agreeing to read this document and attending my defense. Thanks to Dr. Younan Xia for collaborating and providing gold nanocages for research work.

I am deeply indebted to Dorota Wadowska for her immediate help in TEM imaging whenever I required during my research. I would like to extend my thanks to Dr. Christian Lacroix for providing me the access to SEM and also trained me to use the device.

Thanks to all my lab mates, Tyler Palmer, Annie, Michelle Patterson, Evans Monyoncho, Jonathan Horrocks and Christian Agatemor for the good time I spent with all. I would also like to mention the names of Dawna Lund, Janette Paquet, Janice Murphy and Stephen Scully for their support and help. My special thanks to Dr. Ashok Chauhan, my friend since last eight years, for encouraging and helping me with all physics based problems and providing me moral support whenever I need.

Finally, not to forget the contribution of my family and friends, I would like to thank all my family members and friends for their continuous altruistic support and always standing by my side during my ups and downs. Without their co-operation, patience and trust, I would not have been able to accomplish my work.

Table of contents

CHAPTER 2: SYNTHESIS OF GOLD NANOCAGES USING SILVER NANOCUBES AS TEMPLATE

List of figures

List of tables

Chapter 1: Introduction

1.1 Overview

Optoacoustic imaging (OAI) is a hybrid biomedical imaging modality based on the optoacoustic effect. In optoacoustic imaging, laser pulses are delivered into biological tissues. Some of the delivered energy will be absorbed and converted into heat, leading to transient thermoelastic expansion and thus wideband (e.g. MHz) ultrasonic emission. The generated ultrasonic waves are then detected by ultrasonic transducers to form images. This imaging method has been proposed as real-time, noninvasive method for medical imaging and monitoring laser thermal therapy. Nobel metal nanoparticles are widely used contrast agents for imaging purposes. Among all other metal nanoparticles, gold nanocages (AuNCs) gained importance for their easily tunable localized surface plasmon resonances (LSPR) in NIR region, porous walls, hollow interior and biocompatibility.

This thesis includes the synthesis of silver nanocubes (work as a template for gold nanocages synthesis), an investigation of the stability of AuNCs against pulsed laser radiation, an investigation of the contrast properties of AuNCs using Intralipid based phantoms and porcine muscles phantoms. This chapter will provide background on current medical imaging techniques, OA and its applications, contrast agents, polyol and galvanic replacement reactions and mechanisms, and a description of light and acoustic propagation in tissue.

1.2 Current medical imaging techniques

In modern medicine, medical imaging has undergone major advancements. Today, this ability to achieve information about the human body has many useful clinical applications. Over the years, different types of medical imaging have been developed, each with their own advantages and disadvantages. Diagnostic imaging lets doctors look inside our body for clues about a medical condition. A variety of machines and techniques can create pictures of the structures and activities inside our body. The type of imaging used depends on the symptoms and the part of our body being examined. Some of the recent and widely used imaging techniques include X-Ray, Computed Tomography (CT), Magnetic Resonance Imaging (MRI), ultrasound, optical coherence tomography (OCT), etc. Optoacoustic imaging is one of the most recent and advanced imaging techniques specifically for soft tissues.

An X-ray is high-energy radiation that can easily penetrate materials such as skin and tissues but cannot easily penetrate metals and bone. X-ray is the most common energy source for medical imaging. This is one of the cheapest medical imaging techniques also, but has a few limitations, including radiation. Ionizing radiation can cause cell damage and lead to the risk of cancer in future. X-rays also has limited detection ability, so it can't detect deeper structures very well. Computed tomography (CT), involves using X-ray equipment to form a three dimensional image from a series of images taken at different angles around the body[1]. Since a CT scan provides a detailed cross-sectional view of structures, the final picture is far more detailed than an X-ray image. Concerns about CT scans include the risks from exposure to ionizing radiation and possible reactions to the intravenous contrast agent, or dye, which may be used to improve visualization. Magnetic resonance imaging (MRI) uses powerful magnets and radio waves to produce detailed images of the body. The

human body is mostly water, which contains hydrogen atoms. The magnet in an MRI machine produces a strong magnetic field (0.5 – 3.0 tesla) that interacts with the hydrogen atoms[2]. A combination of the magnetic field and different radio frequencies makes it possible to generate an image. MRI is useful for imaging the structure and function of the brain[3], heart and liver[4], soft tissues[5], and the inside of bones[6]. MRI involves risk to patients who have metallic implants, including pacemakers, prosthetic cardiac valves, surgical clips, orthopedic appliances, penile implants, cochlear implants, intravascular filters, stents, coils, dental materials and shunt connectors[7]. Hence, they are typically not candidates for MRI procedures.

Ultrasonic imaging is the second most used imaging modality in medicine (the first being x-rays)[8]. It is estimated that over 25% of all medical imaging procedures involve ultrasound[9]. Ultrasound imaging uses high-frequency (1-20 MHz) sound waves to produce images of body tissues and organs. A device called a transducer produces the sound waves. The transducer is placed on the skin. Sound waves enter the body and are reflected back by internal body structures, much like an echo to the transducer. These reflected sound waves form an image of the body structure, which is recorded on a screen. Because images can be blurred by the presence of air or gas, ultrasound is not recommended for imaging the intestinal area [10]. Ultrasound is used to study soft tissues[11] and major organs in the body. It is not recommended for studying bone because sound wave penetration in bone is limited. Ultrasound is also used in the diagnosis of heart problems[12]. An echocardiogram can be used to find out if there is any abnormality in the heart or blood vessels that could lead to problems such as stroke. Ultrasonic imaging is used extensively in obstetrics. For example, the size and weight of a baby can be estimated

by measuring the diameter of the head, abdominal circumference and femur length on an ultrasound image[9].

Optical tomographic techniques are of particular importance in the medical field, because these techniques can provide non-invasive diagnostic images. Tomographic techniques generate 3D images of target inside the body. There are two well developed optical tomography techniques: diffuse optical tomography (DOT), and optical diffraction tomography (ODT). The vast majority of applications of these techniques are in the biomedical field[13]. Diffuse Optical Tomography (DOT) and Imaging (DOI) are non-invasive techniques that utilize light in the near infrared spectral region to measure the optical properties of tissues[14]. The techniques rely on the object under study being at least partially light-transmitting or translucent, so it works best on soft tissues such as breast[15] and brain tissue[15]. By monitoring spatial-temporal variations in the light absorption and scattering properties of tissue, regional variations in oxy- and deoxy-hemoglobin concentration as well as cellular scattering can be imaged[16]. Based on these measurements, spatial maps of tissue properties such as total hemoglobin concentration, blood oxygen saturation and scattering can be obtained using model-based reconstruction algorithms. DOT and DOI have been applied in various deep-tissue applications including breast cancer imaging[17], brain functional imaging[18] etc.

Optical coherence tomography (OCT) is physically based on ODT. OCT is analogous to ultrasound imaging, except that it uses light (laser) instead of sound. OCT can function as a type of optical biopsy[19] and is a powerful imaging technology for medical diagnostics because unlike conventional histopathology which requires removal of a tissue specimen and processing for microscopic examination, OCT can provide images of tissue *in situ* and in real time[20]. OCT images are two-dimensional data sets that represent the optical backscattering in a cross-sectional plane through the tissue. Image resolution of 1 to 15 μm can be achieved one to two orders of magnitude better than conventional ultrasound[21]. In the late 90s, numerous developments in OCT technology were made. High speed real time OCT imaging has been demonstrated with acquisition rates of several frames per second[22][23]. High resolution and ultra high resolution OCT imaging have been demonstrated using novel laser light sources and axial resolutions as high as 1 μm have been achieved[24][25][26]. Cellular level OCT imaging has recently been demonstrated in developmental biology research[27]. OCT has been interfaced with catheters, endoscopes and laparoscopes which permits internal imaging[28][29].

The above mentioned medical imaging techniques cover a whole spectrum of possible modalities that can be made to suit the demands of the clinician to make a good diagnosis. But everything comes with a price. All of these techniques have their advantages, but moreover their disadvantages. Ultrasound imaging on the other hand is safe in terms of minimal side effects, is low in cost, can achieve real-time imaging, but suffers from limited contrast.

A possible addition to the spectrum would be a technique that can compensate for the downsides of ultrasound imaging and not forfeit too much of the advantages this technique already has. Optoacoustic imaging (OAI) is one of these new techniques. It provides

contrast between tissues structures based on the optical absorption of pulsed laser light. This technique has high potential in terms of providing functional information, high resolution, fast scanning speed, and at a relative lower cost per procedure compared to CT ($ 600-$1100) and MRI ($900-$1900)[30].

1.3 The optoacoustic effect

The history of optoacoustics also known as "photoacoustics" dates back to the 19th century[31], when A. G. Bell presented his invention, the photophone, an early wireless communication device[31]. He used modulated sunlight to transmit spoken messages. The usability of the device was limited by the light source, the sun, which was one of the most readily available light sources back then. Even though a first prototype of the system seemed to work, it could not compete with the spreading wired telegraph and telephone. The optoacoustic effect disappeared from research for want of a better light source. With the invention of the laser in the sixties, new high power light sources became available, and optoacoustic research was revived with a first focus on chemical spectroscopy of gases[32][33]. With periodic optoacoustic excitation at the resonant frequency of the gas container and lock-in detection these devices can trace very small concentrations down to parts per billion (PPB) levels[32][34][33].

The optoacoustic effect can be defined as the conversion of absorbed optical (or electromagnetic) energy to acoustic energy. There is a considerable literature on optoacoustic signal generation and the physical effects, which are responsible for the optoacoustic effect[35][36][37][38]. The thermoelastic effect[39] seems to be more efficient with optical energy compared to the various other energy sources (e.g. microwave,

RF) by which acoustic waves can be generated. The absorption of optical energy leads to localized heating of the object, and subsequent thermal expansion will generate an initial pressure distribution inside the object. This initial pressure distribution finally results in outwards traveling pressure waves. Figure 1.1 shows the schematic diagram of the principle of OA wave detection.

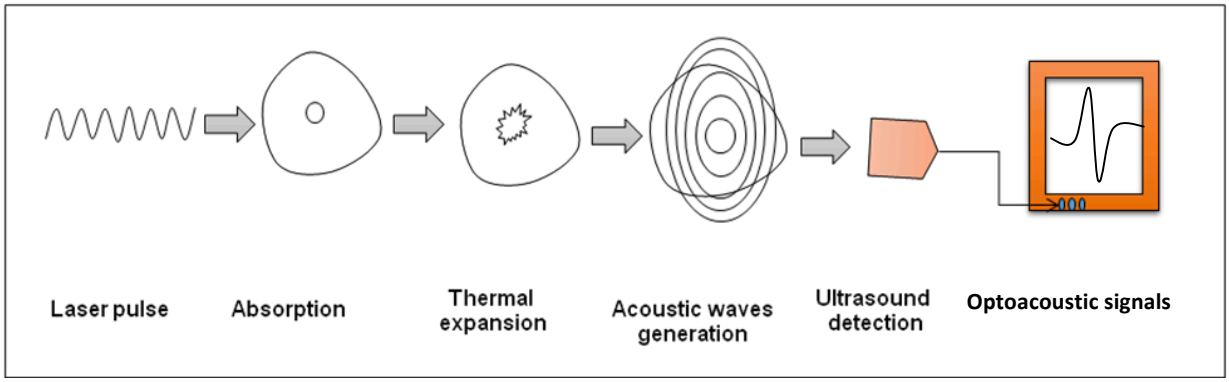

Figure 1.1: Schematic diagram showing the principle of optoacoustic wave detection

To generate optoacoustic waves efficiently, both thermal and stress confinement conditions should be satisfied. The thermal confinement condition is satisfied when the laser pulse duration (τ_p) is much shorter than the thermal relaxation time (τ_{th}). The thermal relaxation time after absorbing a laser pulse of length τ_p is given by[40]

$$\tau_{th} = \frac{L_p^{\ 2}}{4D_T} \tag{1.1}$$

where D_T is the thermal diffusivity of the sample (cm^2/s) and L_p is the characteristic linear dimension (cm) of the tissue volume being heated. Stress confinement is satisfied when the duration of the laser pulse (τ_p) is shorter than the time it takes for the stress to transit the heated region (τ_s) given by[41]

$$\tau_s = \frac{L_p}{c} \tag{1.2}$$

where c is the speed of sound in tissue. For example, to successfully image a target with L_p = 150 μm, c = 1.5 X 10^5 cm/s, and $D_T \approx 1.4\times10^{-3}$ cm^2/s, equations 1.1 and 1.2 indicate that τ_{th} ≈ 40 ms and τ_s ≈ 100 ns[40]. Hence, the laser pulse width must be less than 100 ns to satisfy the stress confinement criterion for these particular tissue properties. When both stress and thermal confinements are satisfied, the optoacoustic maximum pressure, p_0, at the pressure source can be expressed by:

$$p_o = \Gamma \mu_a \phi \tag{1.3}$$

where Γ is the Grüneisen coefficient, a dimensionless quantity that represents thermoacoustic efficiency

$$\Gamma = \frac{\beta c^2}{C_p} \tag{1.4}$$

where μ_a is the optical absorption coefficient [cm^{-1}], Φ is the laser fluence [J/cm^2], β is the volume expansion coefficient [K^{-1}], c is the speed of sound [cm/s], and Cp is the heat capacity at constant pressure [J/(kg K)][42][43][44].

1.4 Light Propagation in Tissues

The origins of the idea of using light to investigate the interior of the human body lie in the 19th century. However, the implementation of routine optical imaging of biological tissue *in vivo* has proven evasive. This is mainly due to one highly disadvantageous property of biological tissue: tissue is not a homogeneous medium but a complicated mixture of materials and structures of all sizes. Light absorption in tissues at visible and near infrared wavelengths is much lower than light scattering. As a result, a significant proportion of the light used to illuminate tissue is scattered and the effective path lengths of photons in the medium significantly increased. In combination this leads to a limited penetration in tissue on the order of a few centimeters for multiply scattered light. In the field of optical imaging of biological tissues, methods are generally differentiated by the photon wavelength and pulse length.

Four different optical parameters are used to describe optical propagation in bulk medium: the refractive index n (which describes how light can change direction at interfaces), the scattering coefficient μ_s, the absorption coefficient μ_a and the scattering anisotropy g.

Biological tissue does not have a constant refractive index throughout the medium. However, one can treat the refractive index as constant by using the effective refractive index of the medium. For most soft biological tissues the effective refractive index is in the range of 1.33 to 1.6[45].

The scattering coefficient μ_s is defined as the probability of a photon being scattered per unit infinitesimal path length (cm^{-1}). The average distance a photon travels between scattering events is given by the reciprocal of the scattering coefficient and called the scattering mean free path[46]:

$$l_s = \mu_s^{-1} \tag{1.5}$$

Similarly to the scattering coefficient, the absorption coefficient μ_a is the probability of a photon being absorbed per unit infinitesimal path length (cm^{-1}). The average distance a photon travels until it is absorbed is then defined by the reciprocal of the absorption coefficient and called the mean absorption length[46]

$$l_a = \mu_a^{-1} \tag{1.6}$$

Scattering anisotropy, g, describes the average cosine of the polar scattering angle. For isotropic scattering (intensity of light radiated is the same in all direction), g, is equal to zero and for purely forward scattering g is equal to 1. Most biological tissues have a scattering anisotropy of about 0.9[47]. The reduced scattering coefficient, μ_s', is a lumped property, that incorporates the scattering coefficient, μ_s, and the anisotropy, g.

$$\mu_s' = (1-g)\mu_s \tag{1.7}$$

With optoacoustics knowledge of the light intensity is needed to understand the generation of acoustic waves according to equation (1.3). The light intensity as a function of depth, Z, for an uncollimated light source incident on a block of tissue is given by:

$$I(Z) = I_o e^{-\mu_{eff} z} \tag{1.8}$$

where $I_\circ$ is incident light and μ_{eff} is the effective attenuation coefficient, defined as:

$$\mu_{eff} = \sqrt{3\mu_a(\mu_a + \mu_s')} \tag{1.9}$$

Another important parameter is "optical penetration depth", δ, which is the reciprocal of μ_{eff} [48]

$$\delta = \frac{1}{\mu_{eff}} \tag{1.10}$$

For optoacoustics, photons themselves do not act as carriers of information about the medium but merely serve as a source of energy for the optoacoustic effect. The information about the medium is carried by the generated acoustic waves. Therefore, the complexity of the paths of the photons in the medium is of importance only in so far as it is related to the distribution of luminous energy in the medium. All the parameters discussed above are important to understand the optical propagation in tissues.

1.5 Acoustic propagation in tissues

Sound, by definition, consists of mechanical vibrations propagating through an elastic medium. These mechanical vibrations are caused by periodic changes in the pressure of the medium, which are in turn caused by forces acting on the individual molecules themselves. Sound propagates because these molecular vibrations are traveling from one molecule to another in such a way that is periodic in nature. The frequency of a sound wave is the number of cycles a given molecule oscillates through per second. The elastic medium can be a solid, liquid or gas. The only real requirement is that there are molecules available to pass on the vibrations. Unlike electromagnetic wave propagation, sound waves are unable to travel in a vacuum. The important acoustic propagation properties for soft tissues are acoustic velocity, acoustic impedance and acoustic attenuation. There are also some tissue properties, which are responsible for acoustic propagation, which include elasticity, density and compressibility.

Elasticity is the ability of an object to return to its original shape after a force has disturbed it. The amount of distortion experienced by the object is largely determined by the molecular interactions within it. The same can be said for tissues. An ultrasound wave traveling through tissues creates tiny elastic deformations of molecules, and is subsequently detected by the transducer and formed into an image[49]. Density (ρ) is another tissue property that will affect the propagation of ultrasound waves. An increase in density will slow the rate of sound travel through the medium. This makes sense if one considers that a higher density means more mass per volume and thus more molecules for the sound wave to attempt to disturb. Compressibility (K) of the medium is the fractional decrease in volume when a pressure is applied to it. A denser medium experiences a

smaller decrease in volume when a constant pressure is applied to it, and thus would have a low compressibility. The converse can be said for low-density media.

The density ρ, compressibility K, combine to determine the speed c, of sound propagation through any tissue[49], according to:

$$c = \frac{1}{\sqrt{(K\rho)}} \tag{1.11}$$

The average velocity of ultrasound waves in soft tissues is 1540 m/s. See Table 1.1 for the speed of sound in various tissues.

Acoustic Impedance (Z) is the product of the medium's density, ρ and sound velocity, c,

$$Z = \rho c \tag{1.12}$$

Acoustic impedances for various tissues are listed in Table (1.1).

Material	Density (Kg/m^3)	Velocity (m/s)	Acoustic impedance ($Kg/m^2/s \times 10^{-6}$)
Air	1.2	330	.0004
Water (20^0 C)	1000	1480	1.48
Liver	1060	1550	1.64
Muscle	1080	1580	1.70
Fat	952	1459	1.38
Brain	994	1560	1.55
Kidney	1038	1560	1.62
Spleen	1045	1570	1.64
Blood	1057	1575	1.62
Lung	400	650	0.26
Aqueous humor	1000	1500	1.50
Vitreous humor	1000	1520	1.52

Table-1.1: Velocity and acoustic impedance of sound in various materials[49].

Impedance mismatching is an important aspect of ultrasonic imaging. If two adjoining media have the same acoustic impedance, nothing happens, the wave simply passes through the interface. But the same cannot be said if the two media have different impedances. In this case some portion of the sound wave is reflected at the interface of the two media.

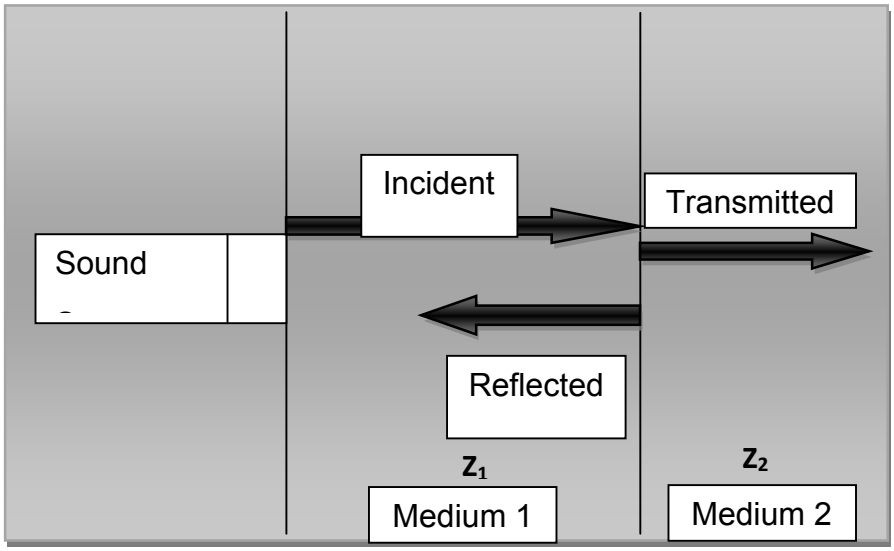

Figure 1.2: Schematic diagram showing various phenomena of sound in different media for sound waves that are incident normal to an interface.

The reflection is due to impedance mismatching. If an ultrasound beam is directed towards an interface, say tissue-air or tissue-bone, then part of it will be reflected back towards the source. The *reflection coefficient*, α_R, is a value that relates the acoustical impedances in such a way that when multiplied by 100%, it gives the percentage of sound reflected. In addition to a portion of the sound wave being reflected, the remainder is transmitted through the interface. As can be seen in the (figure 1.2), at the interface of medium 1 and medium 2, some sound is reflected and some is transmitted.

Similar to reflection, there is also a *transmission coefficient,* α_T , that leads to the percentage of sound transmitted through the interface[50]. The coefficients are given by [122].

$$\alpha_R = \left(\frac{Z_2 - Z_1}{Z_2 + Z_1} \right)^2 , \quad \alpha_T = \frac{4Z_1Z_2}{(Z_2 + Z_1)^2} \tag{1.13}$$

where Z_1 and Z_2 are impendences.

This impedance mismatching is what allows the visualization of soft tissues to occur using conventional ultrasound imaging[51].

When ultrasound waves are propagating through tissues they are attenuated. Attenuation refers to the reduction in intensity of the ultrasound beam as it passes through tissue. Attenuation is an important concept because it limits the penetration of sound and thus the depth of an image that can be obtained via ultrasound imaging. The main contributing factors to attenuation are absorption and scattering.

Absorption is the process whereby ultrasonic sound energy is converted into another form of energy; mainly heat. There are a number of factors that influence absorption. They include: the sound frequency and the viscosity of the medium. In order for sound waves to travel, the molecules in the tissue must be able to move in order to transfer energy. Viscosity is the resistance of a material to flow. A low viscosity medium moves more freely, and thus a high viscosity medium will produce more heat due to friction. If the frequency is increased, the molecules move more often in order to compensate. This in turn generates more friction and more heat. The frequency and the absorption rate are directly related quantities.

Scattering is responsible for speckle in the ultrasound image and gives information about the texture of the tissue[52]. When an ultrasound beam strikes a surface, which is in most cases irregularly shaped, the interface acts as a collection of tiny sound sources, producing reflections in multiple directions. Scattering has a very strong frequency dependence, which makes it useful in determining tissue identities. When the frequency is varied, the scattered reflections change in such a characteristic way that makes it possible to differentiate one tissue from another[53].

In general, the longer path length means higher attenuation. Also, the attenuation coefficient increases with increasing frequency. For soft tissues, there is about 1/2 dB of attenuation per centimeter for each MHz of frequency[54]. Table 1.2 shows attenuation of different materials.

Material	Attenuation (dB/cm)/MHz
Blood	0.18
Fat	0.6
Kidney	1.0
Muscle (across fibers)	3.3
Muscles (along fibers)	1.2
Brain	0.85
Liver	0.9
Lung	40.0
Aqueous humor	0.022
Vitreous humor	0.13
Water	0.0022

Table 1.2: The attenuation of different materials including soft tissues[50].

1.6 Optoacoustic Imaging

Ultrasound waves are used in optoacoustic imaging (OAI) because of their desirable physical properties, such as deeper tissue penetration (~ 5.2 cm)[55]**.** The combination of high ultrasonic resolution with good image contrast because of differential optical absorption is quite advantageous for imaging purposes. When compared with fluorescence

imaging, in which the scattering in tissues limits the spatial resolution with increasing depth, optoacoustic imaging has higher spatial resolution and deeper imaging depth, because scattering of the ultrasonic signal in tissue is much weaker[56]**.** When compared to ultrasound imaging, in which the contrast is limited because of the mechanical properties of biological tissues, optoacoustic imaging has better tissue contrast, which is related to the optical properties of different tissues. In addition, the absence of ionizing radiation also makes optoacoustic imaging potentially safer than other imaging techniques, such as computed tomography and radionuclide-based imaging techniques[57].

Systems for optoacoustic imaging require two primary components: a pulsed energy source and an acoustic detector. Usually, a pulsed nanosecond laser is used as the energy source. The laser pulse is delivered to the tissue through a combination of optical fibers and/or mirrors. Acoustic detectors can be single element or array-based ultrasound transducers of various central frequencies[58]. An ultrasound receiver is required to receive optoacoustic signals, and a microprocessor is used to handle data acquisition, image reconstruction and display.

Basically there are two light delivery and detection modes in optoacoustic imaging. When the light delivery and the detector are in opposite directions, it is called “forward” mode[59]. Forward mode is simple to implement, but *in vivo* applications are limited by the thickness of the tissues to be imaged. In the backward mode geometry, delivery of laser light and receiving of the signals occurred at same side[59] as it is not limited by the thickness of the anatomy.

Blood is the major optical absorbent in biological tissues. Therefore, the OA signal is mainly due to the differential concentration of blood. The absorption coefficient of hemoglobin is

several orders of magnitude greater than the absorption of surrounding tissue. Hemoglobin linked with oxygen (oxyhemoglobin) and hemoglobin without oxygen (deoxyhemoglobin) has different absorption spectra, as presented in Figure 1.3(a). Careful selection of the excitation wavelength can yield important information on oxygenation saturation. Spectral range higher than the cell's absorption has no dependence on saturated oxygen (SO2)[60]. Figure 1.3(b) shows the absorption spectra of the major absorbers in biological tissues: water, melanin and blood. This figure shows why NIR is preferred over other wavelengths for tissue imaging as absorption by water is minimal in this region of the spectra, and absorption by blood is large.

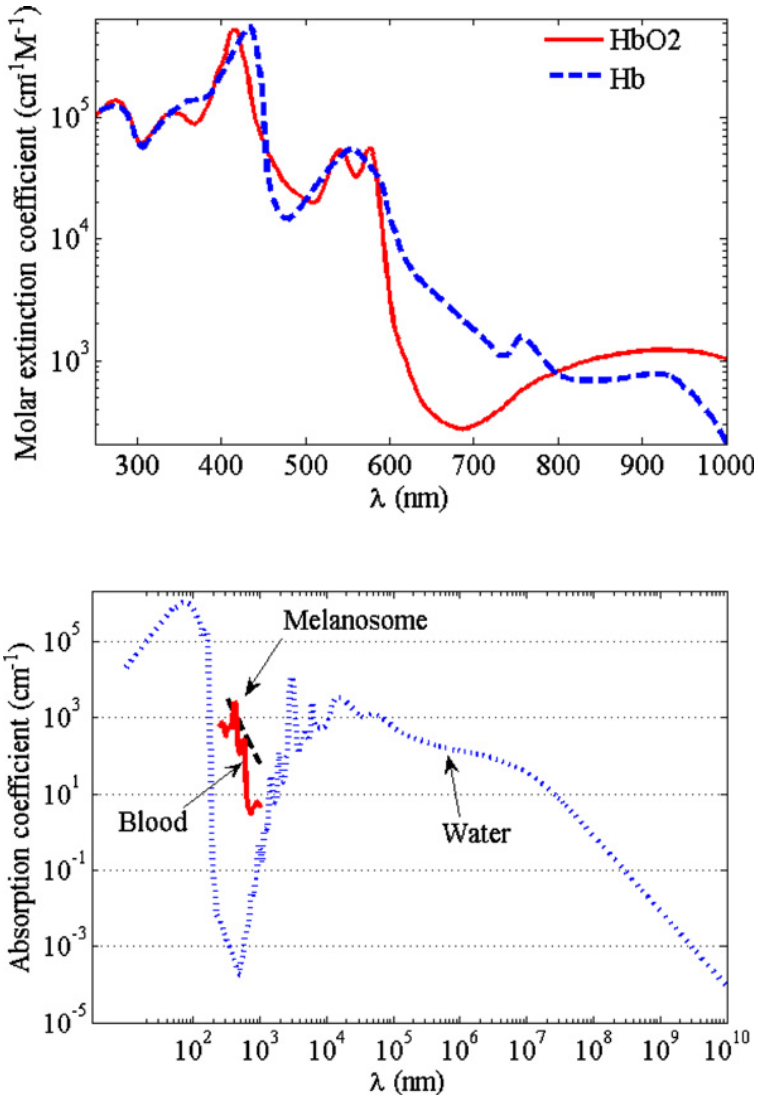

Figure-1.3: (a) Absorption spectra of oxyhemoglobin (HbO2) and deoxyhemoglobin (Hb). (b) Absorption coefficients of blood, melanosomes and water[44].

Optoacoustics has several applications such as cancer detection[61][62], small animal imaging[63], monitoring of angiogenesis and identification of atherosclerosis plaques[64]. The most promising application of OA is cancer detection, specifically breast cancer[65][66] and recent work on the detection of prostate cancer[67][68]. OA is also being investigated to monitor thermal therapy[69]. The basic mechanism of cancer detection is based on the absorption of light by hemoglobin. To fully understand how blood vessel imaging is useful,

the mechanisms of cancerous tumors growth have to be explained. Generally, cell population is controlled by the body with certain factors that cause the cells to die (apoptosis) when they are not needed. By not responding to these signals, the cancerous cell will be uncontrollable. If it can replicate indefinitely, which is not the case for most cells, it will grow to become a cancer[69]. A large number of cancerous cells are called tumor. But to fuel this exponential growth, the tumor needs nutrients and oxygen[69] which are supplied by blood vessels. The process involves the creation of new blood vessels and is called angiogenesis[69]. This results in a large volume of blood vessels in and around the tumor. This higher concentration of blood around the cancer can be used to efficiently detect it[70][71]. Another important aspect to note is that, in general, there are not enough blood vessels to fuel the entire tumor[69]. Therefore, the overall oxygenation ratio is lower, meaning there is more deoxyhemoglobin.

Oraevsky *et al.* and Ermilov *et al.* have demonstrated promising work in the field of breast cancer detection. Oraevsky *et al.*[72][61]have developed an imaging system [laser optoacoustic imaging system (LOIS)] that uses two different lasers, a Nd:YAG laser operating at 1064 nm and an Alexandrite laser operating at 755 nm along with a hemicylindrical array of transducers. The choice of laser is founded on the difference in absorption by blood and the required penetration depth. For blood, deoxyhemoglobin absorbs more in the range of 755 nm, while oxyhemoglobin absorbs more 1064 nm light. By imaging with these two wavelengths, quantitative information of the tissue's oxygenation saturation can be extracted from the OA data. Figure (1.4) shows the schematic diagram of Ermilov's LOIS-64 imaging system.

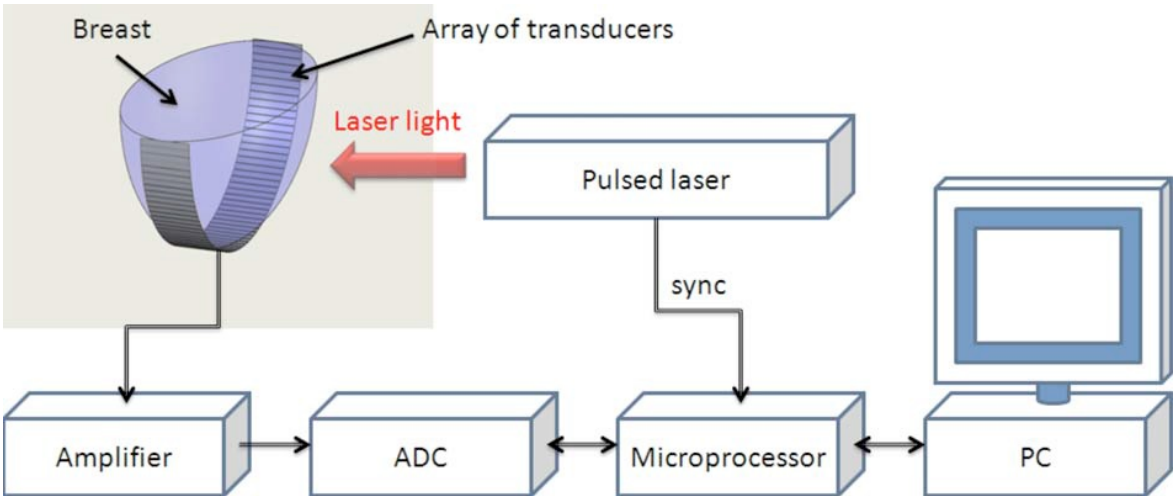

Figure 1.4: Schematic diagram of LOIS-64[61]. Reprinted with permission, *Journal of Biomedical Optics,* (2009).

Lao *et al.* (2008) monitored tumor growth of subcutaneous inoculated breast cancer tumor cells in a mouse over a 20 day period using a 532 nm laser (figure 1.5)[73]. They found that morphological vascular features of early tumor growth could be detected using OA imaging. Total acquisition time for each image was approximately 18 minutes and changes in the morphology and optical absorption of the vessels were observed over the duration the experiment.

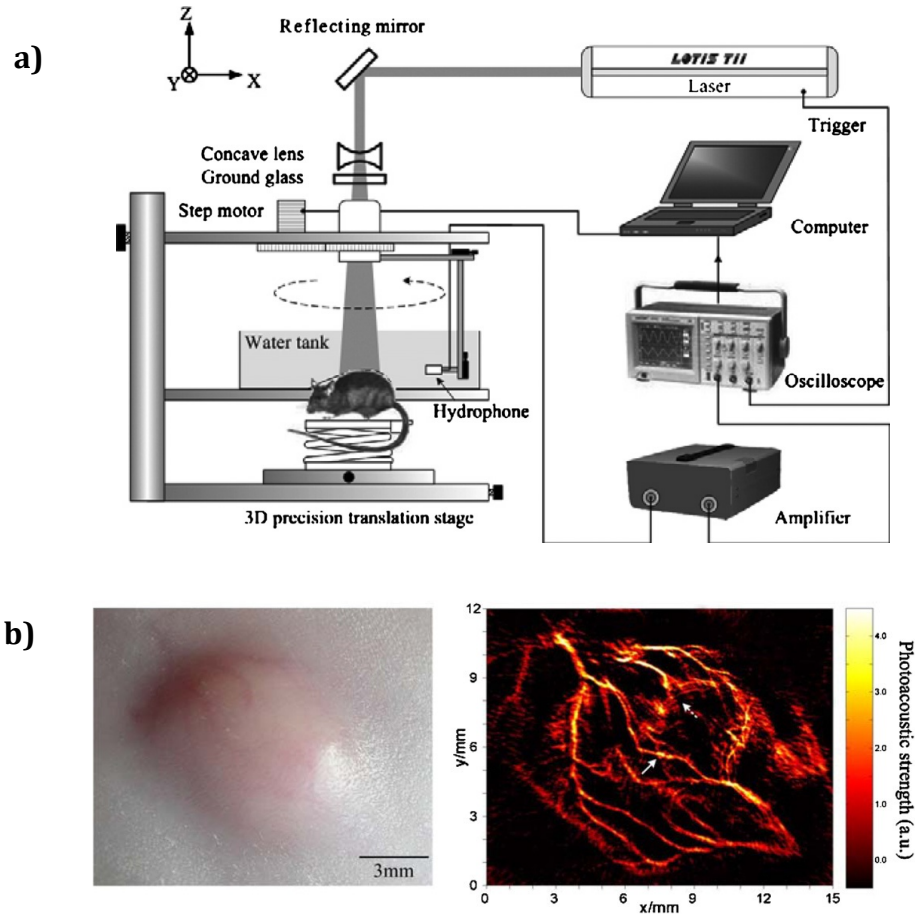

Figure 1.5: a) Schematic diagram of the photoacoustic imaging system used by Lao et.al (2008), and b) photograph of tumor nodule (left) and corresponding optoacoustic image (right)[73]. Reprinted with permission, *Physics in Medicine and Biology,* Volume 53, Issue 15, Pages 4205 and 4207, Figure 1 and 3 (2008).

Laufer *et al.* [74] demonstrated the use of a novel all-optical photoacoustic scanner for imaging the development of tumor vasculature and its response to a therapeutic vascular disrupting agent. The system was used to noninvasively image human colorectal tumor xenografts implanted subcutaneously in mice (figure 1.6)[74]. Label-free three-dimensional *in vivo* images of whole tumors to depths of almost 10 mm with sub-100-micron spatial resolution were acquired in a longitudinal manner. This enabled the development of tumor-related vascular features, such as vessel tortuosity, feeding vessel

recruitment, and necrosis to be visualized over time. Acquisition time for each image was approximately 8 minutes.

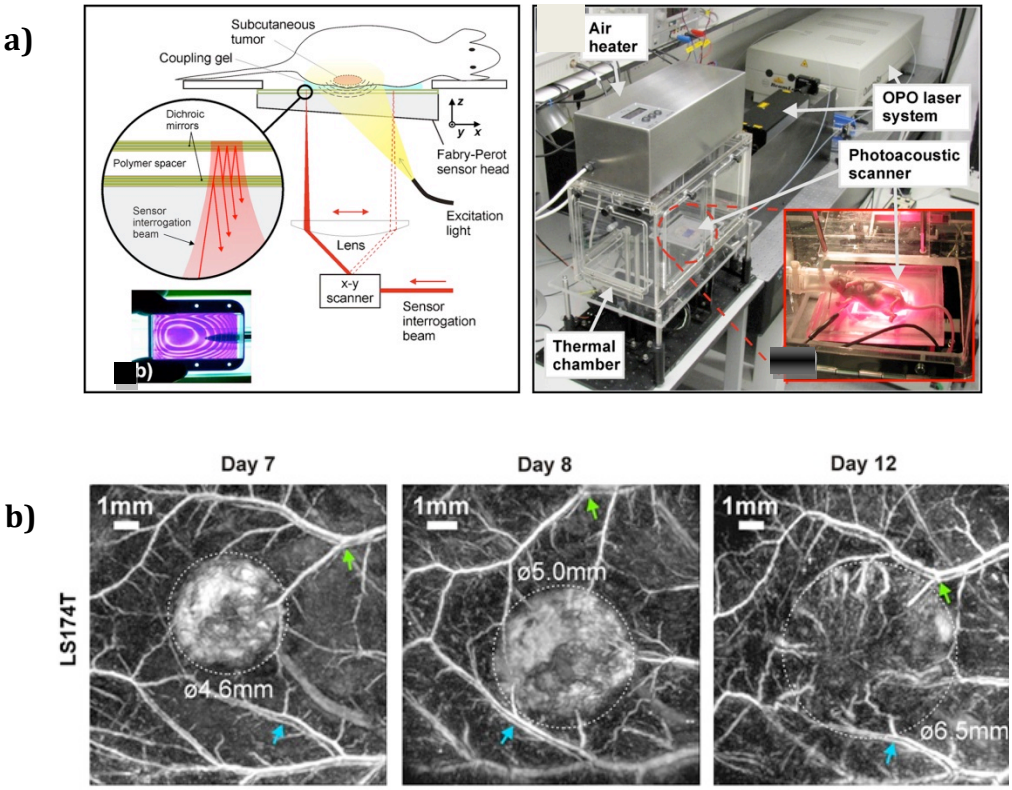

Figure 1.6: a) Schematic of the optoacoustic imaging system used by Laufer et.al (2012) and (right) a photograph of the imaging system showing the system in operation and the anaesthetized animal. b) Optoacoustic images (maximum intensity projections) showing the development of human colorectal tumour LS174T and the surrounding vasculature between day 7 and 12 post inoculation. The dashed lines indicate the tumour margins. The arrows show common vascular features in the images[caption is copied as it is][74]. Reprinted with permission, *Journal of Biomedical Optics,* Volume 17. Issue 5, Figures 1 and 4 (2012).

The majority of the OA systems recently described in the literature, with the ability to image in real time and with the highest resolution and deep penetration, used spherical or cylindrical detection geometries[75][76]. For example, Brecht et.al (Fairway Medical Technologies, Inc., 2009) developed a system for three-dimensional whole-body optoacoustic tomography of small animals for applications in preclinical research. The

tomographic images were obtained while the objects of study (phantoms or mice) were rotated within a sphere outlined by a concave arc-shaped array of 64 piezocomposite transducers. Two pulsed lasers operating in the near-IR spectral range (755 and 1064 nm) with an average pulsed energy of about 100 mJ, a repetition rate of 10 Hz, and pulse duration of 15 to 75 ns were used as optical illumination sources. Both kidneys were visualized along with the spleen and a partial lobe of the liver with spatial resolution of approximately 0.5 mm (figure 1.7).

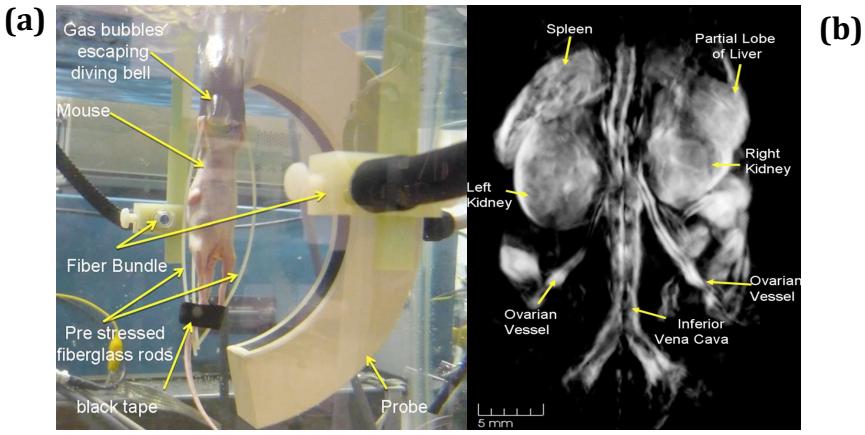

Figure 1.7: Optoacoustic whole body scanner with spherical detection geometry. a) Experimental setup showing 64 elements arc array. b) Three dimensional image of a nude mouse acquired using 775 nm illuminations[75]. Reprinted with permission, *Journal of Biomedical Optics*, Volume 14, Issue 6, Figures 1 and 6 (2009).

Optoacoustic imaging (OAI) can also be used to identify atherosclerotic plaques. Atherosclerosis is a systemic disease in which lipid accumulates in arterial walls and form atherosclerotic plaques. Inflammation also occurs and leads to an increase in blood content in the plaque. The major complication of atherosclerosis is a rupture of the plaque which will form a thrombus that can block blood flow in the artery, leading to the death of the tissue fed by the artery[77]. The vulnerability of a plaque to rupture depends on the content

of the plaque. Thus, information on the content of the plaque will allow identification of the vulnerable plaques and take action before it ruptures. A group from the University of Texas led by S. Sethuraman and SY Emelianov [78][64][79] demonstrated a new device for intravascular optoacoustic using a commercial intravascular ultrasound probe. This probe consists of a catheter with a high frequency (40 MHz) transducer at the tip. Such high frequency can be used because the required imaging depth is small since the plaques are usually a few millimeters thick. Ex vivo studies on cholesterol fed rabbits show that optoacoustic tomography can be used to identify atherosclerotic plaques[80].

1.7 Contrast agents

Optoacoustic imaging (OAI) provides good image quality (image resolution around 60 μm)[81] for various applications without using any exogenous contrast agents. However, the use of an exogenous contrast agent can greatly enhance image contrast. A long list of contrast agents for biomedical imaging is available, but each has pros and cons. The optical absorption of endogenous tissue is at a minimum in the near-infrared (NIR) region from 700 to 1100 nm known as the therapeutic optical window due to the maximum depth of penetration in tissues.

While selecting a contrast agent for OAI, one should carefully consider the absorption spectrum, toxicity, size, shape, composition, surface chemistry, targeting moieties, and stability. The list of OAI contrast agents start with dyes and then noble metals (gold, silver) nanoparticles, carbon nanotubes, nanobeacons and more recently microbubbles[82].

Indocyanine green (ICG), IRDye800CW, AlexaFluor-750 and Methylene blue are some common dyes used for OAI[83]. These are biocompatible and are absorbing in the visible-NIR optical window. These dyes are typically small molecules on the order 1 nm and are

able to quickly clear from the body through the renal system. Despite all the advantages, these dyes also have some limitations, such as poor photostability[84], low quantum yield[85], insufficient stability in biological system, low detection sensitivity[85] etc.

Noble metal nanoparticles are widely investigated as optoacoustic contrast agents, due to their strong and tunable optical properties that result from Surface Plasmon Resonance (SPR). The SPR effect of metal nanoparticles provides them an optical absorption which is five orders of magnitude higher than dyes[86]. Plasmonic nanoparticles have been synthesized in different shapes and sizes, each with unique optical characterization. Choice of nanoparticles is based on the application such as imaging depth, optical wavelength range and biological interaction. Gold nanospheres are the most basic shape that can be synthesized[87]. Their peak absorption (approximately 520 nm) lies to the left of the therapeutic optical window, in a wavelength region where blood and melanin absorb strongly. Nanorods are extensively used in OA imaging studies because of their relatively simple synthesis and tunable absorption in the NIR region[88][89][90]. Gold nanoshells (which consist of a spherical silica core surrounded by a thin layer of gold) have also been used for OA imaging contrast[91][92]. However, nanoshells exhibit significantly more scattering than absorption and a broad optical spectrum, making them less effective OA contrast agents than nanorods[93]. Gold nanoplates also show promise for OA imaging at NIR wavelengths[94]. Recently, Dr. Pan and Lanza[95] introduced molecular OA imaging with colloidal gold nanobeacons. Gold nanobeacons are a robust nanoparticle platform that entraps multiple copies of tiny spherical gold nanoparticles (2–4nm) within a larger colloidal particle encapsulated by biocompatible synthetic or natural amphilines. The utilization of numerous small gold particles greatly amplifies the signal without exceeding the 6nm renal elimination threshold size of humans, while the large particle dimension is

optimal for vascular imaging, such as specific delineation of angiogenesis from small but maturing microvessels[96].

Single-walled carbon nanotubes (SWNTs) are nonplasmonic nanoparticles that can also be used in OA imaging. SWNTs absorb over a broad spectrum, including the optical window, resulting in a large OA signal[97]. Similar to plasmonic nanoparticles, SWNTs can be modified to expand their capabilities. For example, gold-coated SWNTs have been shown to produce an OA signal that is commensurate with that generated by gold nanorods and much larger than the signal resulting from plain SWNTs[98]. Alternatively, dyes can be attached to SWNTs resulting in greater absorption than the dye or SWNTs alone[99].

Microbubbles have become well established over the past 20–30 years as the most effective type of contrast agent particle available for ultrasound imaging[100]. They have been successfully employed with a wide range of imaging techniques, and their potential for therapeutic applications is currently under investigation. However, while a fairly substantial amount of theoretical and experimental research has been conducted, their behavior is by no means fully understood. Jian *et al.* [101] recently introduce OA contrast opportunities associated with theranostic multifunctional micro- and nanobubbles. Their work, although still early, describes an approach based on encapsulation of highly absorbing optical contrast agents, such as gold nanoparticles, India ink and Indocyanine green, for development of multimodal imaging contrasts[101].

Gold nanocages, invented by Younan Xia and colleagues at Washington University are a new type of nanostructure that have hollow interiors and ultrathin porous walls[102]. They are typically between 30–100 nm in diameter. The structures can be designed to absorb strongly and scatter light in the near-infrared (IR) region of the electromagnetic spectrum

(from 700–900 nm). Their compact size, bio inertness[103] and well-defined surface chemistry[104], combined with a strong and highly wavelength-tunable optical absorption in the near-infrared window of soft tissues[104], make them particularly attractive as exogenous contrast agent. Like gold nanorods and nanoshells, the optical properties of gold nanocages can be precisely tuned to the specific wavelength in the electromagnetic spectrum[105]. Compared with the former two nanostructures, nanocages can have stronger absorption in the near infrared while maintaining their relatively small dimensions (e.g., 30-40 nm in edge length)[105]. This feature makes gold nanocages a class of ideal contrast enhancement agents for use with optical imaging modalities like optoacoustic imaging. Gold nanocages can also be easily bioconjugated with antibodies for selective targeting of cancer cells[106]. Exposure of the nanocages to light can convert the absorbed photons into phonons, leading to a temperature increase of the lattice[105]. Heat dissipation from the hot particles may selectively cause damages to the targeted cancer cells[107] and is being investigated as a therapy[108].

1.8 Polyol synthesis

There has been extensive research into the synthesis of metal particles by the polyol process. Over the past decade the polyol process has been used to prepare elemental Co, Ni, Cu, Ag, Au, Pt, Pd, Cd, and Fe and also bimetallic alloys of CoNi, AgPd, AuPt, and FePt[109]. Papers also highlight the formation of metal oxides such as Fe_3O_4, $CoFe_2O_4$, $CuFe_2O_4$, and $ZnFe_2O_4$[109]. More recently, the polyol process has been used to prepare aqueous ferrofluids as MRI contrast agents[110], bimetallic core/shell nanoparticles for catalysis[111], TiO_2 nanocomposites for monolithic dye sensitized solar cells[112], cobalt carbide nanoparticles for permanent magnet research[113], and Ag and Ag@Au nanoparticles for surface enhanced Raman scattering[114].

The polyol process refers to a polyalcohol that acts not only as a solvent but also as a mild reducing agent, and when coupled with a base, it serves as a perfect medium for the reduction of metal salt precursors. In this process, a solid inorganic precursor is suspended in a liquid polyol. The solution is then stirred and heated to a given temperature, which can reach the boiling point of the polyol for less easily reducible metals. The starting materials can be hydroxides (e.g., Cu $(OH)_2$), nitrates (e.g., $AgNO_3$), oxides (e.g., Cu_2O), chlorides (e.g., $FeCl_2$) or acetates (e.g., Ni $(CH_3COO)_2$). The reduction to metal can be achieved in various polyol such as ethylene glycol (BP: 197.3 ^{0}C), propylene glycol (BP: 188.2 ^{0}C), diethylene glycol (BP: 244 ^{0}C), tetraethylene glycol (BP: 327 ^{0}C), and butylene glycol BP: (207.5 ^{0}C).

The choice of which polyol is used for the reduction of metal precursors is determined by the boiling point and reduction potential of the glycol; for example, easily reducible metals (Pt, Pd, and Cu) do not require high heat and can be reduced in propylene glycol (BP~188 ^{0}C), while less easily reducible metals (Co, Fe, and Ni) require higher temperature for which

tetraethylene glycol may be suitable (BP 327 ^{0}C). Although the physical properties such as size, shape, and crystal structure of the particles have been controlled by manipulating synthetic conditions influencing the nucleation and growth steps, there are limited attempts to fully understand the polyol reaction mechanism[115]. Consequently, nanoparticles are often synthesized through trial and error or combinatorial methods, running large numbers of experiments and systematically varying the parameters. Larcher *et al.* utilized theoretical calculations to prepare a thermodynamic approach to a mechanism for the polyol process[116].In their calculations they assumed that precursor reduction results in the total oxidation of ethylene glycol into CO_2 and H_2O. In this situation, above the boiling point (200 ^{0}C), the ethylene glycol has the maximum reducing power[117].

As mentioned earlier in this chapter there were limited attempts to fully understand the polyol reaction mechanism, but then Dr. Younan Xia[102] and his group developed polyol synthesis as a simple, robust and versatile method for producing silver nanocubes as monodispersed samples and he also published the mechanism behind this method. Ethylene glycol, PVP and inorganic salt precursor ($AgNO_3$) were the main reagent for this study[118].

The main feature of the reaction mechanism is that the reduction reaction proceeds *via* the solution rather than the solid phase. Therefore, the metal particles are formed by nucleation and growth from solution.

The formation of the main product, *i.e.* diacetyl, can be explained in terms of a double oxidation of acetaldehyde, previously produced by dehydration of ethylene-glycol[119], as follows:

$$CH_2OH - CH_2OH \xrightarrow{-H_2O} \underset{\text{Acetaldehyde}}{CH_3 - CHO} \qquad (1.14)$$

$$2CH_3CHO \xrightarrow{2M\ (I)} 2M + 2H^+ + \underset{\text{(diacetyl (butane-2, 3 dione)}}{CH_3 - CO - CO - CH_3} \qquad (1.15)$$

According to this mechanism, the polyol acts as a solvent for the starting inorganic compound due to the rather high dielectric constant of these organic media. In particular, silver nitrate is soluble in ethylene glycol to such an extent that a complete dissolution is observed as the first step of the reaction.

An envelopment of reduced metal atoms within a suitable layer could act as a protection for the nanometric particles during their growth[120][121][122]. A number of organic materials are known to work as protective agents for preventing colloid sintering[123]. Among them poly (N-vinylpyrrolidone) (PVP) exhibits the best protecting properties[124]. Prevention of particle sintering can be achieved by adding a critical dosage of an organic protective agent, which covers the particles and inhibits any possibility of silver-silver particle bond formation. The presence of this agent at the solid/liquid interface does not interfere with the silver discussion-surface deposition process since the particles grow to a definite size. Beside this steric stabilizing activity, PVP allows the reaction to happen also at room temperature and decreases the particle size[124]. Polyvinylpirrolidone is a homopolymer whose individual unit contains an amide group. The N and O atoms of this polar group probably have a strong affinity for the silver ions and metallic silver. A PVP macromolecule in solution, which most likely adopts a pseudo-random coil conformation,

may take part in some form of association with the metal atoms, thus increasing the probability of nucleus formation. It should be pointed out that ethylene-glycol can also act as a protective agent but in the polyol process it is not able to prevent particle sintering because of the high temperatures required for the reaction. Moreover, the presence of PVP also decreases the mean particle size. This effect can be explained according to the above described reaction mechanism. Because of the PVP presence, the rate of spontaneous nucleation increases, and a higher number of nuclei are formed during the nucleation burst. Thus, the number of final particles increases as well, and for a given amount of precipitated metal, the mean particle size therefore decreases[125].

Wiley and Xia conducted an experiment, in which small gold nanoparticles were attached as markers to the surfaces of silver nanowires through the dithiol linkage, and verified that PVP interacted more strongly with silver atoms on the {100} facets than those on the {111} facets[120]. This binding specificity can be attributed to the difference in surface atom density, 1.20×10^{19} versus 1.38×10^{19} m^{-2} for the {100} and {111} planes.

The reduction of $AgNO_3$ by ethylene glycol at 150 ^{0}C led to the formation of elemental silver (step I in Figure 1.8) at a moderate rate, because of the strong dependence of the reducing power of ethylene glycol on the reaction temperature[120]. Clusters[126] of a critical size (or nuclei) appeared (i.e., nucleation, steps II and III in Figure 1.8) once the concentration of zero-valent silver reached a critical value. This depiction is built upon La Mer's model for the nucleation of monodispersed sols in a homogeneous system. The hot solution consistently turned yellow as the $AgNO_3$ and PVP solutions were introduced, indicating the formation of silver nanoparticles with a roughly rounded profile, since such particles display a distinctive SPR peak around 400 nm[127]. In the subsequent growth process (step

IV in Figure 1.8), silver atoms generated from the reduction of $AgNO_3$ diffused to the surface of nuclei and positioned themselves at active surface sites, forming metallic bonds with their neighbors. By adjusting the molar ratio between PVP and $AgNO_3$, the thickness of PVP coating and the location of PVP chains on the surface of a seed could both be modified. This modification, in turn, altered the resistance of each facet to growth (addition of silver atoms), and led to the formation of silver nanostructures with distinct shapes. The drawings on the right side of Figure 1.8 summarize three types of silver nanostructures that have been successfully synthesized by means of this PVP-mediated polyol process.

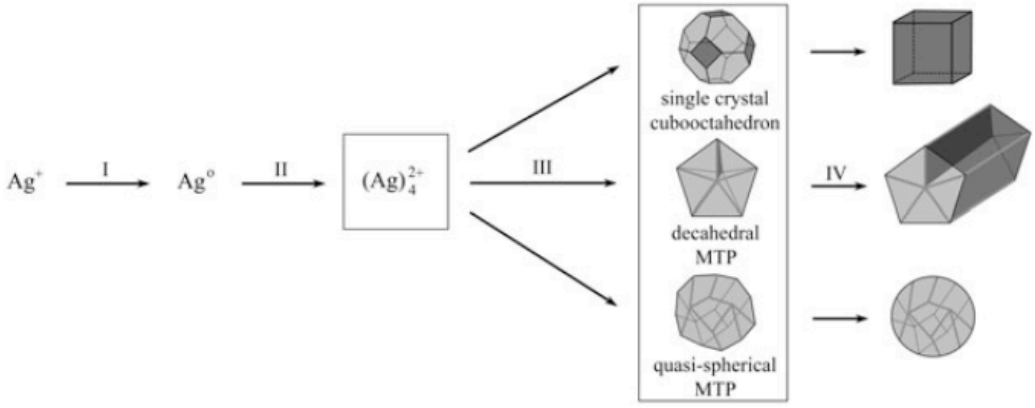

Figure1.8: Schematic illustrating the reduction of silver ions by ethylene glycol (I); the formation of silver clusters (II); the nucleation of seeds (III); and the growth of seeds into nanocubes, nanorods or nanowires, and nanospheres (IV). The formation of metal clusters and seeds with different cystallinities depicted in the boxes is currently being studied. This article focuses on the growth of silver nanostructures with well-defined and controllable shapes. The surfaces marked in light and dark gray represent the {111} and {100} facets, respectively. The light gray lines and dark grey interior planes represent the twinned boundaries and twinned planes, respectively. Figure caption copied as in[128].

Maybe the most attractive morphology yet synthesized by this polyol process is the nanocube. To produce this type of nanostructure, the concentration of $AgNO_3$ in the final solution must be relatively high (0.125–0.25m), and the molar ratio between PVP and

$AgNO_3$ must be low (at ~1.5)[129]. These conditions result in fast nucleation and growth of the silver seeds, and may therefore have reduced the time available for twin defects to form. In addition, since twinning is only favorable when the surface energy of the {100} facets is greater than that of the {111} facets[130]. The presence of PVP can serve to reduce the driving force for twin formation through its selective interaction with the {100} planes. Once a large proportion of single-crystal seeds form, selective adsorption of PVP on the {100} facets will lead to preferential addition of silver atoms to the {111} facets. As the growth rate in the <111> direction is greater than that in the <100> direction, the {100} sides of the cube will become enlarged at the expense of the {111} corners[131]. After the cubic shape is formed, each face of the silver nanocube will have the same growth rate, and further growth will mainly increase the size with no significant morphological variation.

1.9 Galvanic replacement reaction

Galvanic replacement is one of the simple and effective methods for generating metal nanostructures with hollow interiors. The driving force for the galvanic replacement reaction is the electrical potential difference between two metals, with one metal acting principally as the cathode and the other metal as the anode. For example, a piece of zinc (Zn) plate placed in an aqueous 1 M Zn^{2+} solution attains a potential of approximately -0.76 V relative to the standard hydrogen electrode (SHE)[132]. When immersed in a solution containing Cu^{2+} ions, the zinc begins to dissolve and elemental copper (Cu) starts to form as a result of the higher reduction potential of Cu^{2+}/Cu (0.34 V versus SHE) and the coupling of the two half reactions: $Cu^{2+} + 2e^- \rightarrow Cu$ and $Zn \rightarrow Zn^{2+} + 2e^-$. The rates of these two reactions must be the same to preserve electroneutrality. Once a continuous coating of copper has been formed on the surface of the zinc plate, further reaction can be prevented[133].

Significantly, the Zn^{2+}/Zn and Cu^{2+}/Cu system can be replaced with noble metal systems, e.g. silver (Ag) nanostructures and chloroauric acid ($HAuCl_4$), opening up the possibility for preparing noble metal nanostructures with hollow interiors. Since the standard reduction potential of $AuCl_4^-/Au$ (0.99V versus SHE) is higher than that of Ag^+/Ag (0.8V versus SHE), Ag nanostructures suspended in the solution can be oxidized by $HAuCl_4$ according to the following redox reaction:

$$3Ag_{(s)} + AuCl^-_{4\ (aq)} \rightarrow Au_{(s)} + 3Ag^+_{\ (aq)} + 4Cl^-_{\ (aq)} \qquad (1.16)$$

The reaction starts with the formation of a pinhole on one of the six faces of each cube as Ag is being removed owing to oxidation[134]. With the progression of this corrosion process, the pitting site continues to serve as the anode where Ag is oxidized and electrons are exposed. Released electrons then migrated to nanocubes surfaces and captured by $AuCl_4^-$ ions to generate Au atoms via reduction as Ag and Au have the same face centered cubic structure and essentially identical lattice constant. Therefore Au atoms prefer to nucleate and grow on the surface of Ag nanocubes. In the beginning, the incomplete layer of Au prevents the underneath Ag template from being dissolved and also allows the initially generated pinhole to serve as a primary site for Ag dissolution [step 2 in figure 1.9(a) and 1.9(d)] that eventually turns a nanocube into a nanobox with an empty interior. Later on, the surface pinhole gradually closes due to different mass transfer processes, including the lateral diffusion of Au atoms around the edge of the opening.

After the sufficient addition of $HAuCl_4$, the void space achieves its maximum size, which completely closes the pinhole and turned a nanocube into a nanobox with uniform wall thickness [step 3 in figure 1.9(a) and 1.9(e)]. Elevated temperature gives rise to Ag-Au alloy

during replacement reaction[135]. In this case, the composition profile of the Au/Ag alloyed wall should evolve with time, in accordance with Fick's second law. The relevant solution for the inter-diffusing interface, with mutually soluble components, can be expressed as.

$$C_{(x,\,t)} = 0.5 + 0.5\mathrm{erf}\,\{x/\,[2(Dt)^{1/2}]\} \qquad (1.17)$$

(erf = error function)

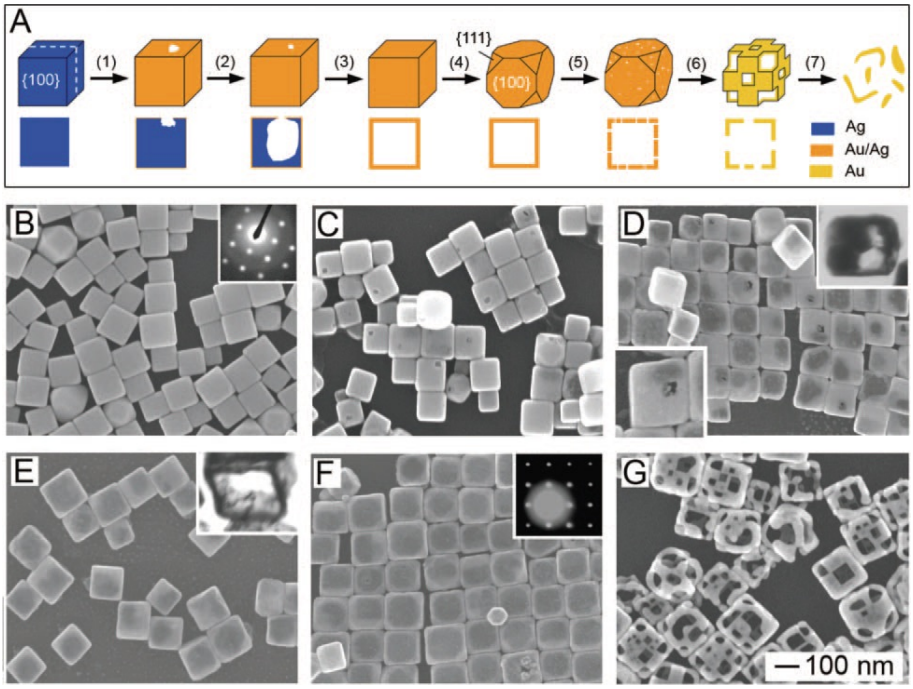

Figure 1.9: (a) Schematic illustration summarizing all major morphological and structural changes involved in the galvanic replacement reaction between a sharp Ag nanocube and $HAuCl_4$. The cross-sectional views correspond to the plane along dashed lines. (b) SEM image of the sacrificial templates – Ag nanocubes; (c)–(g) SEM images for the hollow nanostructures obtained from galvanic replacement reaction at steps 1, 2, 3, 5 and 6 of (a), respectively. Insets of (d) (e) are the transmission electron microscopy (TEM) images, and insets of (b), (f) are the electron diffraction patterns for the corresponding nanostructures. The volumes of 1mM $HAuCl_4$ solution added to the suspension of Ag cubes in 5mL water are 0, 0.05, 0.30, 0.50, 0.75, and 2.25mL for sample (b) through (g), respectively. The concentration of Ag for the initial nanocube suspension was ~0.8mM, as determined with atomic emission spectroscopy. The 100nm scale bar applies to all SEM images Figure caption copied as in [Xianmao Lu, USA][133].

Here, D is the inter-diffusion coefficient (m^2s^{-1}), and C is the atomic fraction of Au as a function of time (t) (sec) and distance (x) (meters) separated from the interface. D is strongly dependent on both temperature and film thickness, and the magnitude of D can be significantly increased with an increase in reaction temperature or a decrease of thickness for the Au layer[135][136]. The dependence of D on the thickness of Au layer has been attributed to the high surface energy of a nanostructure at small size and the rich vacancy defects at the bimetallic interface[137]. D is on the order of 10^{-24} m^2/s at room temperature

when 2.5 nm Au nanoparticles are coated with 1 nm Ag layers[136]. According to the Arrhenius equation:[138]

$$D = D_0 \exp\left(\frac{-\Delta H_a}{kT}\right) \tag{1.18}$$

The value of D is estimated to be on the order of 10^{-19} m^2/s at 100°C. In this case, the activation enthalpy, ΔH_a, is taken as 1.58 eV[139]. Since the Au layer formed during early stages of the galvanic replacement reaction (steps 1, 2, and 3 in Figure 1.9) was thinner than 2.5 nm, the inter-diffusion coefficient is assumed to be $\sim 10^{-19}$ m^2/s during the formation of Au/Ag alloy walls of the nanoboxes. According to equation (1.17), the alloy layer can contain as much as 10 per cent Ag, even though the nanobox has only been annealed at 100°C for 20 s. It is worth noting that the diffusion coefficient of Ag in Au is different from that of Au in Ag. It has been shown that Ag diffuses about 30%; faster in Au than Au diffuses in Ag[140], resulting in the Kirkendall effect, which creates a net mass flow towards the Au/Ag alloy shell instead of the un-reacted Ag template[140]. Consequently, the shell composed of an Au/Ag alloy is well maintained without volume shrinkage. The Au shell has morphology similar to that of the Ag template, with the void size mainly determined by the dimension of the template. On the basis of the stoichiometry relationship shown in equation (1.16), the wall thickness of each Au nanoshell should be approximately one tenth of the lateral dimension of the corresponding Ag template[141].

When more $HAuCl_4$ is added to the reaction system, the Ag atoms in the Au/Ag nanoboxes are then selectively removed through a dealloying process[142]. At this stage, numerous defects, or lattice vacancies, are formed because reaction stoichiometry, i.e. equation (1.16), which dictates that the removal of three Ag atoms corresponds to the deposition of only

one Au atom. The resultant vacancies lead to negative curvatures for the solid walls, causing the interfacial area and the surface energy to increase[143]. To release these lattice vacancies, the nanobox will reconstruct its morphology via a process similar to Ostwald ripening[144]. As a result, each corner of the box becomes truncated to form a new face bounded by one of the {111} crystallographic planes (step 4 in Figure 1.9(a) and Figure 1.9(f)). As more Ag atoms extracted by $AuCl_4$ ions from the walls of the truncated box, more lattice vacancies formed that start to coalesce and generate pinholes in the walls (step 5 in Figure 1.9(a)). Further dealloying leads to an enlargement of the lateral dimensions of the pinholes (step 6 in Figure 1.9(a) and Figure 1.9(g)). Complete dealloying will cause the porous nanobox (now commonly referred to as nanocages) to collapse into small fragments of pure Au (step 7 in Figure 1.9(a)).

At the end we can say that gold nanocage (AuNCs) is a unique structure, which can be synthesized by using two different methods, polyol method to synthesize silver nanocube template and then galvanic replacement method to make a hollow cage like structure of gold, which can be an important contrast agent in optoacoustic imaging due to its tunable absorbing properties.

1.10 Hypothesis and Objectives

One of the greatest challenges in OA imaging is detecting targets (e.g. cancers) at depth greater than 2-3cm. This is a result of high optical attenuation. Metallic nanoparticles can potentially be used to improve image contrast. Gold nanocages have yet to be fully characterized as a contrast agent for imaging. We hypothesize, that gold nanocages, with absorption in NIR region can improve detection of targets in optoacoustic imaging,

The main objectives of this thesis are:

1. To synthesize gold nanocages using silver nanocubes as templates via polyol synthesis and galvanic replacement reactions. (Chapter2)

2. To determine the stability of gold nanocages against pulsed (6ns) laser light at relevant energies. (Chapter3)

3. To determine the contrast properties of gold nanocages in 1% Intralipid based tissue mimicking phantoms (Chapter 4) and *ex vivo* tissues (porcine muscles). (Chapter 5)

Chapter 2: Synthesis of gold nanocages using silver nanocubes as template

Synthesis of gold nanocages is a two step process. The first step involves the synthesis of silver nanocubes of high purity and homogenous size. In the second step, these silver nanocubes work as sacrificial templates for the production of gold nanocages via galvanic replacement reaction.

2.1 Silver nanocubes synthesis

Polyol process has been used for the synthesis of silver nanocubes. Recently Xia *et al.* (2006) made significant modifications to this process to cut down the reaction time from 16-26 hour to 3-8 minutes[145]. Two different protocols have been used for the synthesis of silver nanocubes, published by Xia[146][147]. In the first protocol[146], silver nitrate ($AgNO_3$) was used as a silver precursor and sodium sulphide (Na_2S) as a catalyst and in the second protocol, silver trifluoroacetate (CF_3COOAg) was used as a silver precursor and sodium hydrosulfide (NaHS) as a catalyst. Researchers were using silver nitrate as the precursor for nanocube synthesis but recently, in 2010, Xia's group switched to silver trifluoroacetate[147]. Their argument for this change was that, the nitrate group may decompose at an elevated temperature typical of a Polyol synthesis to generate ionic and/or gaseous species, making the synthesis more difficult to understand and control[147].

2.2 Materials (Chemicals) used in synthesis

For the synthesis of silver nanocubes, the following reagents were used:

Chemicals	Related information
Anhydrous ethylene glycol (EG)	Sigma-Aldrich, 102466, ≥99%
Polyvinylpyrrolidone (PVP)	Mw: 55,000, Aldrich, CAS: 9003-39-8
Silver nitrate ($AgNO_3$)	≥99.99%, Sigma-Aldrich,
Silver trifluoroacetate (CF_3COOAg)	≥99.99%, CAS: 2966-50-9
Sodium sulphide ($Na_2S.9H_2O$)	Sigma-Aldrich, CAS: 1313-84-4
Sodium hydrosulfide (NaHS)	Sigma-Aldrich, CAS: 207683-19-0
Hydrochloric acid (HCl)	Reagent grade, 38%
Acetone	Reagent grade
Ethanol	Reagent grade
Chloroauric acid ($HAuCl_4.3H_2O$)	99.9%, Aldrich, CAS: 27988-77-8
Sodium chloride (NaCl)	Sigma, CAS: 7647-14-5

Table 2.1- List of chemicals used in the synthesis of silver nanocubes/gold nanocages.

2.3 Synthesis of silver nanocubes using $AgNO_3$ as a precursor[146]

2.3.1 Protocol for synthesis:

An oil bath (silicone fluid) was heated to 150^0 C with continuous stirring (approx. 300 rpm). The experimental set up shown in figure 2.1A. Four 24 ml vials were used in one synthesis batch; clean stir bars (Teflon coated, egg shaped) and 6 ml of ethylene glycol was added to each vial as the second step. A vial holder was used to suspend the vials in the heated oil bath. Vial caps were loosed to allow water vapour to escape. Ethylene glycol, in

the vials was heated for 1 hour to remove all the water. Meanwhile three different solutions were prepared:

Firstly, a PVP solution in ethylene glycol was prepared (PVP works as capping agent). For one vial, 0.03g of PVP was required to dissolve in 1.5 ml (0.18 M) of ethylene, therefore for the 4 vials; 0.14 g of PVP was dissolved in 7 ml of ethylene glycol (little excess for proper pipette technique).

Then a second, 1 ml solution of approximately 3 mM Na_2S in ethylene glycol was prepared. This solution will be used to catalyze the reduction of Ag^+ during silver cube synthesis. Initially a 30 mM solution of Na_2S in ethylene glycol was prepared by adding 0.072 g of Na_2S in 10 ml of ethylene glycol. Then a vortex mixer (Fisher, vortex Genie 2) was used to dissolve Na_2S in ethylene glycol. Next, 100 µl of 30 mM solution was transferred to another vial and 900 µl of ethylene glycol was added to make an approx. 3 mM Na_2S solution (Term approximately used for Na_2S concentration, because of the hygroscopic nature of sodium sulphide). The solution was again agitated for 5 min before the addition to synthesis reaction.

Finally, a third solution, silver nitrate in ethylene glycol was prepared to use as silver precursor. A 0.024 g of $AgNO_3$ in 0.5 ml of ethylene glycol (0.28 mM) was required for each vial. Then 0.12 g of $AgNO_3$ was added to 2.5 ml of ethylene glycol to prepare enough solution for four reaction vials. Each vial was sealed and agitated using a vortex mixer until all the silver nitrate was dissolved.

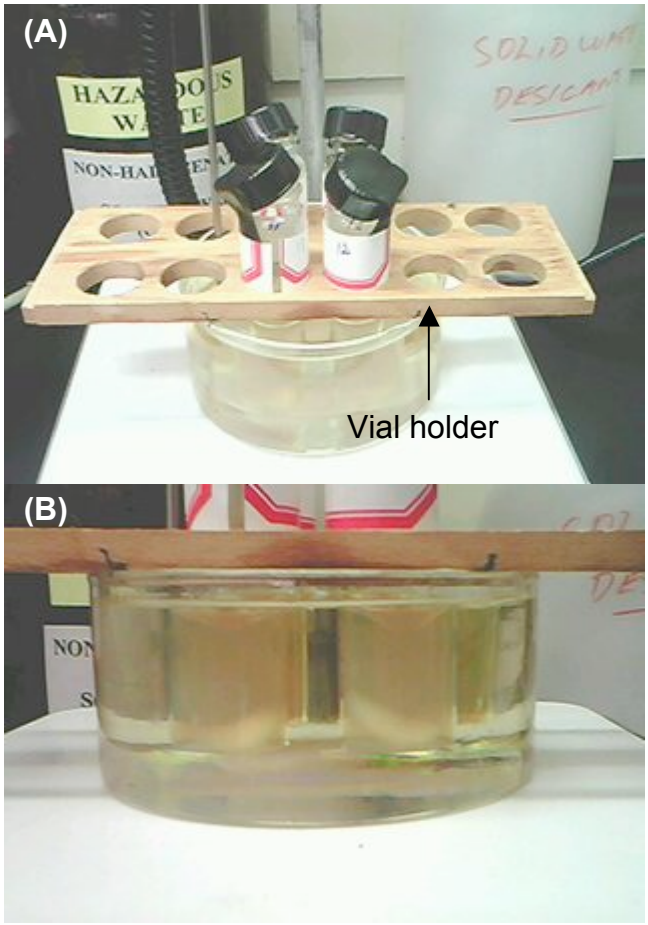

Figure 2.1: setup of synthesis reaction, showing the oil bath on hot plate and arrangement of reaction vials in oil bath (A). Desired green-ochre color after the complition of reaction (B).

Then, after 1 hour of heating of the ethylene glycol, the vials caps were removed and 4 different volumes (70, 80, 90, 100 µl) of sodium sulphide solution were added using a micropipette (VWR) into vial 1 to vial 4, respectively, and the vials were recapped loosely. After 8 min, the caps were removed again and 1.5 ml of the PVP solution was added to each vial (in two aliquots of 0.75 ml). After the addition of the PVP solution, a 0.5 ml of $AgNO_3$ solution was added immediately into each vial and the vials were loosely recapped. A series of color changes occurred upon injection of the $AgNO_3$/EG solution (step IX). Immediately after the addition, the mixture turned purple/black - transparent bright yellow (with in 1 min) - yellow-orange to orange brown (within 2-3 min) - deposition of Ag

on walls (within 5 min) - opaque, ruddy-red when viewing the reaction meniscus and green-ochre when viewed head on (within 7-10 min) (shown in figure 2.1B). And then, after 10 min, as soon as green-ochre colour occurred the reaction was quenched by placing vials in water bath at room temperature.

2.3.2 Washing of reaction content:

After cooling, the contents of the vials were transferred into their corresponding 30 ml centrifuge tubes. Vials were rinsed twice with 6 ml of acetone each time and washings were transferred to appropriate tubes. Contents in each centrifuge tube were spun down (Ultracentrifuge, Beckman Coulter) at 2000g for 25 min. Supernatant was removed and discarded by using disposable glass pipettes. And then, 2 ml of deionised (DI) water was injected into each tube and was agitated via sonication (Branson 200) to re-disperse the product. Then half of the volume was transferred to 1.5 ml volume centrifuge tubes and again centrifuged (Beckman Coulter, Optima L-90K) at 9000g for 10 min. Supernatant was removed and rest of the contents were transferred to 1.5 ml tubes and again centrifuged at 9000 g for 10 min. Washing was repeated 3 times. Finally washed products were re-dispersed in 4 ml of DI water and stored for characterization and further use.

2.4 Synthesis of silver nanocubes using CF_3COOAg as precursor[147]

2.4.1 Protocol for synthesis:

A 50 ml volume of ethylene glycol was added to a 250 ml round bottom flask (RB) (ace glass) and heated under magnetic stirring in an oil bath pre set to 150^0 C. Three different solutions were prepared during the heating period. First, a PVP solution in ethylene glycol was prepared. In a 24 ml vial, 350mg of PVP was weighed and 17.5 ml of ethylene glycol (0.364 mM) was added and then agitated via a vortex mixer to dissolve the PVP completely. Second, a 3 mM solution of 3.2 mg HNaS in 19 ml ethylene glycol was prepared. Third, a 325 mM solution of silver trifluoroacetate in a 24 ml vial was prepared by adding 359 mg of CF_3COOAg into 5 ml of ethylene glycol. A vortex mixer was used to agitate the solution for proper mixing. A HCl solution in ethylene glycol was also prepared by adding 5 µl of HCl to 20 ml (3 mM) ethylene glycol (HCl increases production of high-quality Ag nanocubes, as Cl^- ion acted as ligand for oxidative etching to eliminate twinned particles). Sodium hydrosulfide (HNaS) solution (0.6 ml) was quickly injected into the heated ethylene glycol after its temperature had reached 150^0 C. Then after 4 min, a 5 ml HCl solution was injected into the heated reaction solution. Two min after the addition of HCl solution, 12.5 ml of PVP solution was added to the reaction mixture. After 4 min, 4 ml of silver trifluoroacetate solution was injected into the reaction mixture. During the entire process, the RB flask was capped with a glass stopper except during the addition of reagents. After the addition of CF_3COOAg, the transparent reaction mixture turned to a whitish color and then quickly turned yellow within 1 min. The reaction was allowed to proceed for 30 min and its color went through three stages of dark red, reddish grey and finally brown. Finally, the reaction was quenched after 30 min by placing the RB flask into a water bath at room temperature.

2.4.2 Washing of reaction content

The same procedure was followed as mentioned in first protocol (chapter 2, section 2.3.2) and the final product was stored in DI water.

After the washing, final product from both the protocols was characterised by using different techniques mentioned in section 2.5 of the chapter.

2.5 Results and discussions

To achieve necessary shape, size and purity of silver nanocubes for the synthesis of gold nanocages 38 batches were synthesized. Optical properties of silver nanocubes were analyzed by using UV-Vis-NIR spectrophotometer (Varian, Cary-50Bio). Structural and purity information for the silver nanocubes were collected using X-ray Diffraction (XRD, D8 Advance, Bruker axs). Thermogravimetric analysis (TGA, Q500) was done to confirm the presence of PVP after the final washing because it is very difficult to remove all the PVP from synthesized cubes as PVP has very high affinity with silver. The geometric parameters of synthesized silver nanocubes were determined by the High Resolution-Transmission Electron Microscope (HR-TEM, Hitachi BioTEM 7500: Nissei-Sangyo, Rexdale, Ontario, Canada, Camera: AMT XR40 side mount, Advance Microscopy Techniques, Danvers, MA, USA).

2.5.1 Optical absorption characterization

It is known that localized surface plasmon resonances (LSPR) is based on the size of cubes and size depends upon the reaction time of the nanocube synthesis[147]. The absorption spectrum for representative synthesized silver nanocubes using protocol 1 and batch no 8 is shown in Figure 2.2.

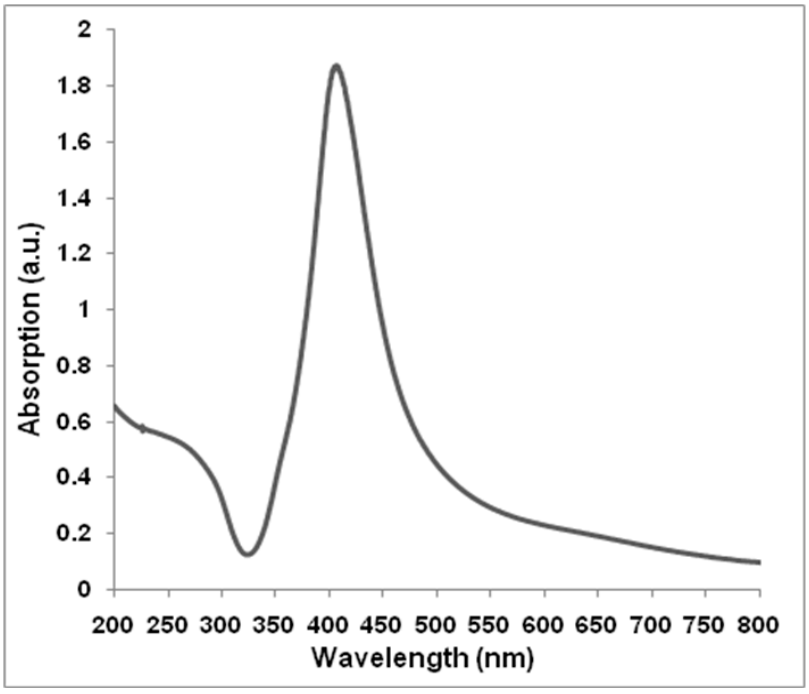

Figure2.2: Optical absorption graph of silver nanocubes obtained from a SNC-8 synthesis batch.

Figure 2.2 shows the LSPR of silver nanocubes is at 420 nm, that indicates the size of nanocubes is between 30-45 nm[147]. All the batches of Ag nanocube synthesized (using protocol 1 and 2) had similar LSPR. However, optical absorption cannot confirm the exact shape of the metal nanopartcles.

2.5.2 X-ray diffraction measurements of Ag nanocubes

X-ray powder diffraction (XRD) is a rapid analytical technique primarily used for phase identification of a crystalline material and can provide information on unit cell dimensions. In this thesis, XRD is used to determine the crystallinity and purity of silver nanocubes. For the sample preparation, a few drops of silver nanocube solution were spread on a glass slide and air dried before using.

A representative of the X-ray diffraction pattern of the silver nanocubes synthesized by polyol method (protocol 1) is shown in Figure 2.3. Different batches tested using XRD, generated identical patterns.

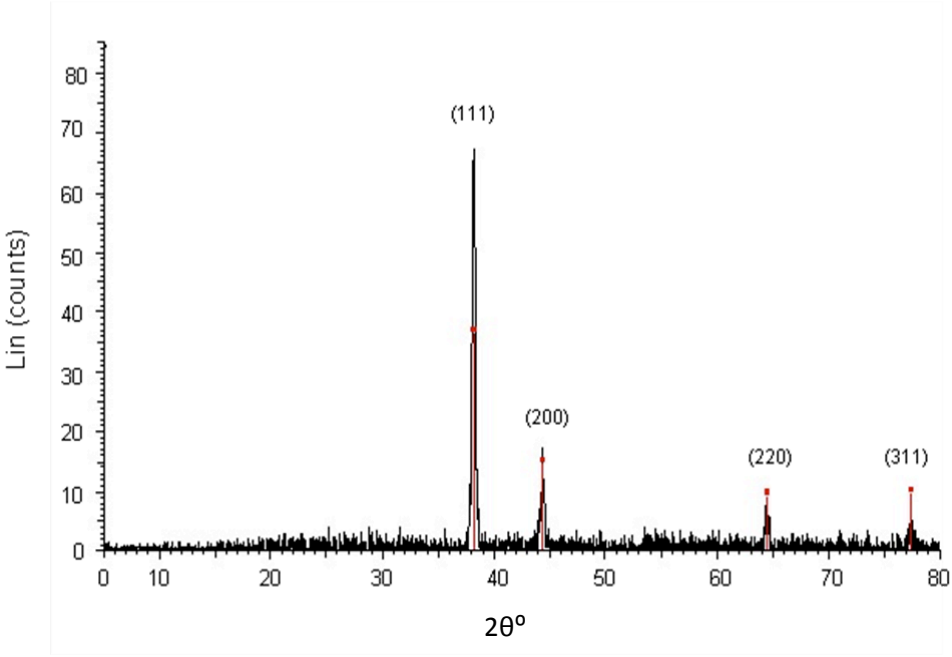

Figure2.3: XRD pattern of silver nanocubes, black peaks representing the synthesized nanocubes and red pattern are standard XRD patterns for silver nanoparticles.

A number of strong Bragg reflections can be seen which correspond to the (111), (200), (220) and (311) reflections of face-centered cubic (FCC) silver[148]. No spurious

diffractions due to crystallographic impurities are observed[149]. All the reflections correspond to pure silver metal with face centered cubic symmetry. The high intense peak for FCC materials is generally (1 1 1) reflection, which is observed in the sample. The intensity of peaks indicates the high degree of crystallinity of the silver nanoparticles. The XRD demonstrates that silver nanoparticles formed are crystalline. Four peaks at 2θ values of 38, 44, 64 and 77 deg. corresponding to (111), (200), (220) and (311) planes of silver are observed and compared with the standard powder diffraction card of Joint Committee on Powder Diffraction Standards (JCPDS) (red color pattern in graph). The XRD study indicates that the resultant particles are (FCC) silver nanoparticles[150]. However, XRD cannot provide information about the shape of the nanoparticles.

2.5.3 Thermogravimetric analysis of Ag nanocubes

Thermogravimetric analysis (TGA) is an analytical technique used to determine a material's thermal stability and its fraction of volatile components by monitoring the weight change that occurs as a specimen is heated. The measurement is normally carried out in air or in an inert atmosphere, such as Nitrogen or Argon, and the weight is recorded as a function of increasing temperature. Pollyvinylpyrolidone (PVP) was used as stabilizer in the synthesis of silver nanocube and PVP has has high affinity with the silver[145], Therefore, thermogravimetric analysis (TGA) was used to determine if any PVP was left on the silver nanocubes after several washings. Sample for the TGA analysis was prepared by freeze drying (Virtis benchtop) of silver nanocubes. Decomposition temperature of pure PVP is 380^0C[151]. Figure 2.4 shows the TGA of synthesized silver nanocubes (protocol 1, SNC-8 batch).

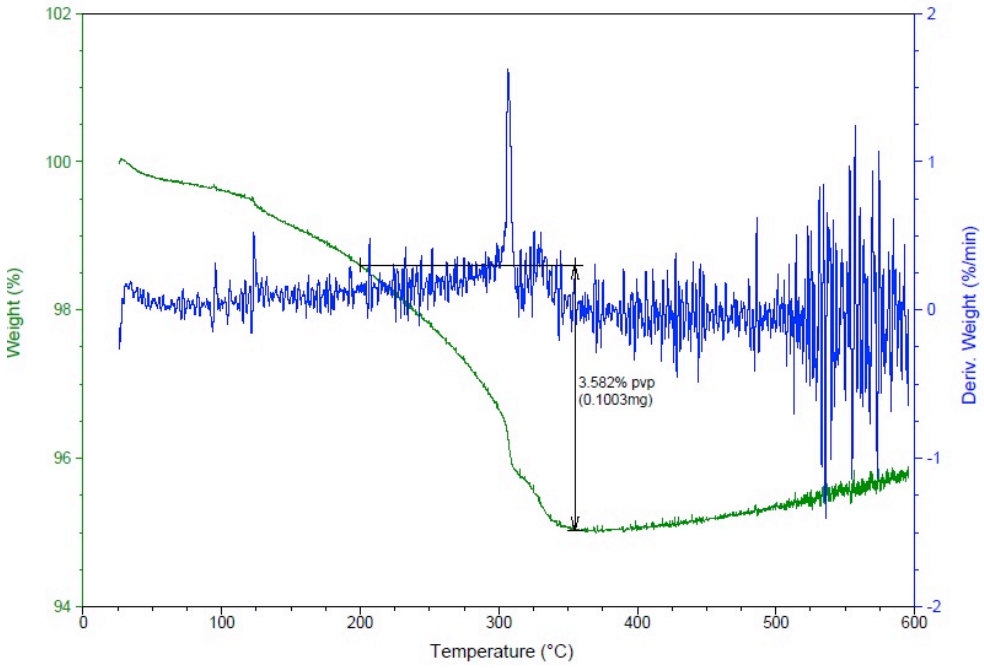

Figure2.4: TGA of silver nanocubes obtained from SNC-8 synthesis batch.

Figure 2.4 shows the continuous decrease in mass of sample with increasing temperature indicating the presence and decomposition of PVP. Decomposition temperature of PVP attached on silver nanocubes is 350^0C according to TGA graph shown in Figure 2.4. Thermogravimetric analysis of PVP coated on Pt was done by Du *et al.*[151] also demonstrate that PVP decomposed at 350^0C which is also 30^0C less than the pure PVP decomposition temperature. The weight loss below 90^0C is due to evaporation of absorbed water and the weight loss starts above 100^0C is attributed to the thermal decomposition of PVP. Thus, TGA confirmed the presence of PVP on silver nanocubes, even after several washings. TGA graph shown in Figure 2.4 demonstrates that only 3.58% (0.1003mg out of 2.8 mg sample) PVP is present which could be ignored and no further washings were done.

2.5.4 Transmission electron microscope imaging (TEM) of Ag nanocubes

The transmission electron microscope uses a high energy electron beam transmitted through a very thin sample to image and analyze the microstructure of materials with high resolution. The beam of electrons from the electron gun is focused into a small, thin, coherent beam by the use of the condenser lens. This beam is restricted by the condenser aperture, which excludes high angle electrons. The beam then strikes the specimen and parts of it are transmitted depending upon the thickness and electron transparency of the specimen. This transmitted portion is focused by the objective lens into an image on phosphor screen or charge coupled device (CCD) camera. Optional objective apertures can be used to enhance the contrast by blocking out high-angle diffracted electrons. The image then passed down the column through the intermediate and projector lenses, is enlarged all the way. The image strikes the phosphor screen and light is generated, allowing the user to see the image. The darker areas of the image represent those areas of the sample that fewer electrons are transmitted through while the lighter areas of the image represent those areas of the sample that more electrons were transmitted through.

In this section of thesis, TEM imaging was conducted to confirm the geometry of synthesized nanoparticles. For the sample preparation, a drop from silver nanocube suspension (Ag nanocubes in DI water) poured on the carbon coated grid and after 1 min extra water was absorbed by a Kimwipes (VWR) and sample was ready to load. As mentioned earlier, two different protocols were followed for the silver nanocube synthesis. Figure 2.5 (a,b,c) shows the TEM images for representative silver nanocubes synthesized using protocol-1[146]. The three figures are from three different synthesis batches (SNC-7, SNC-8 and SNC-9).

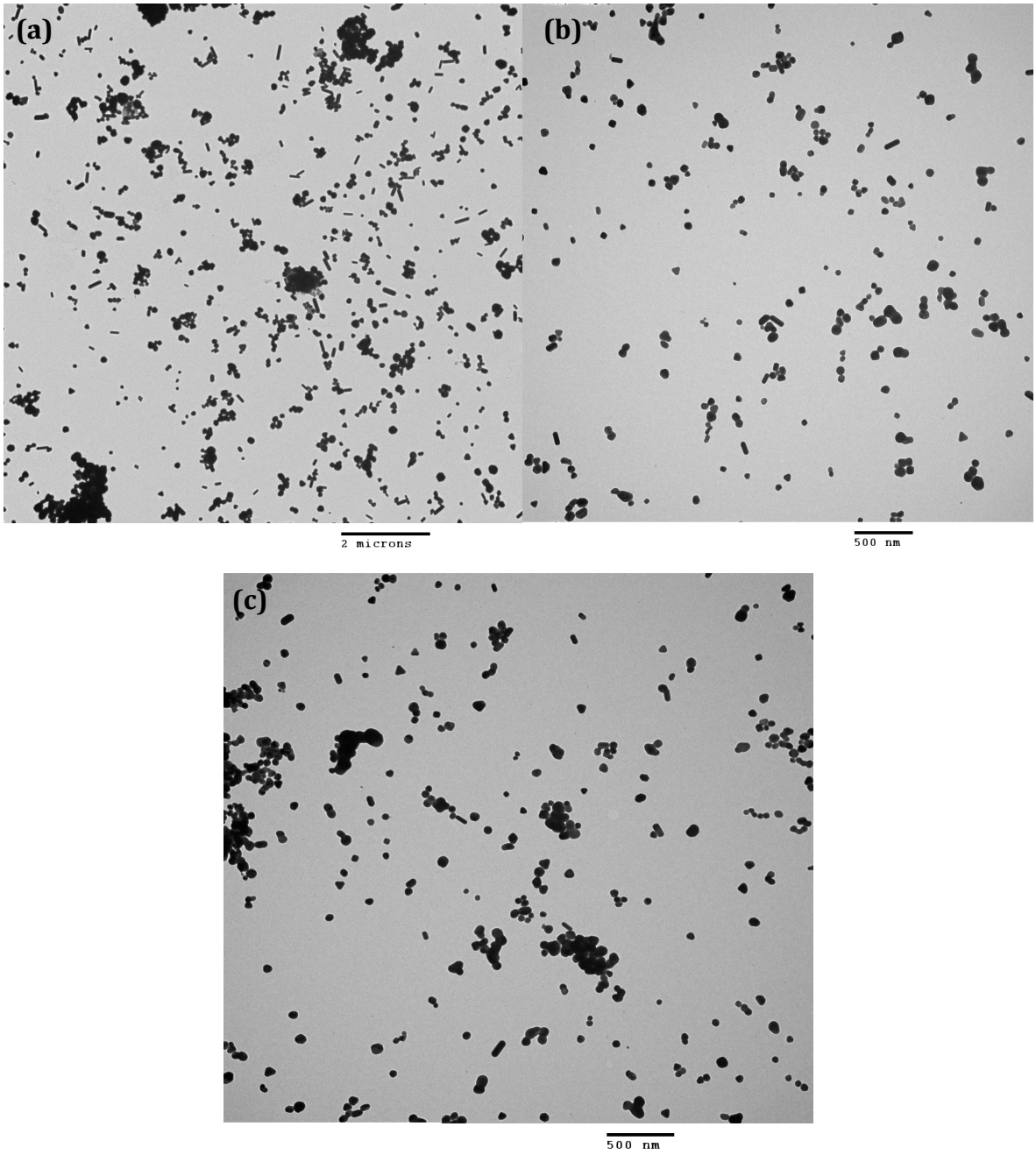

Figure 2.5: TEM images of different synthesis batches of Ag nanocubes following the protocol 1. a) SNC-7, b) SNC-8 and c) SNC-9.

Figure 2.6 (a,b,c) are TEM images of Ag nanocubes synthesized using protocol 2[147]. The three figures are from three different synthesis batches (Exp-25, Exp-26a and Exp-26b).

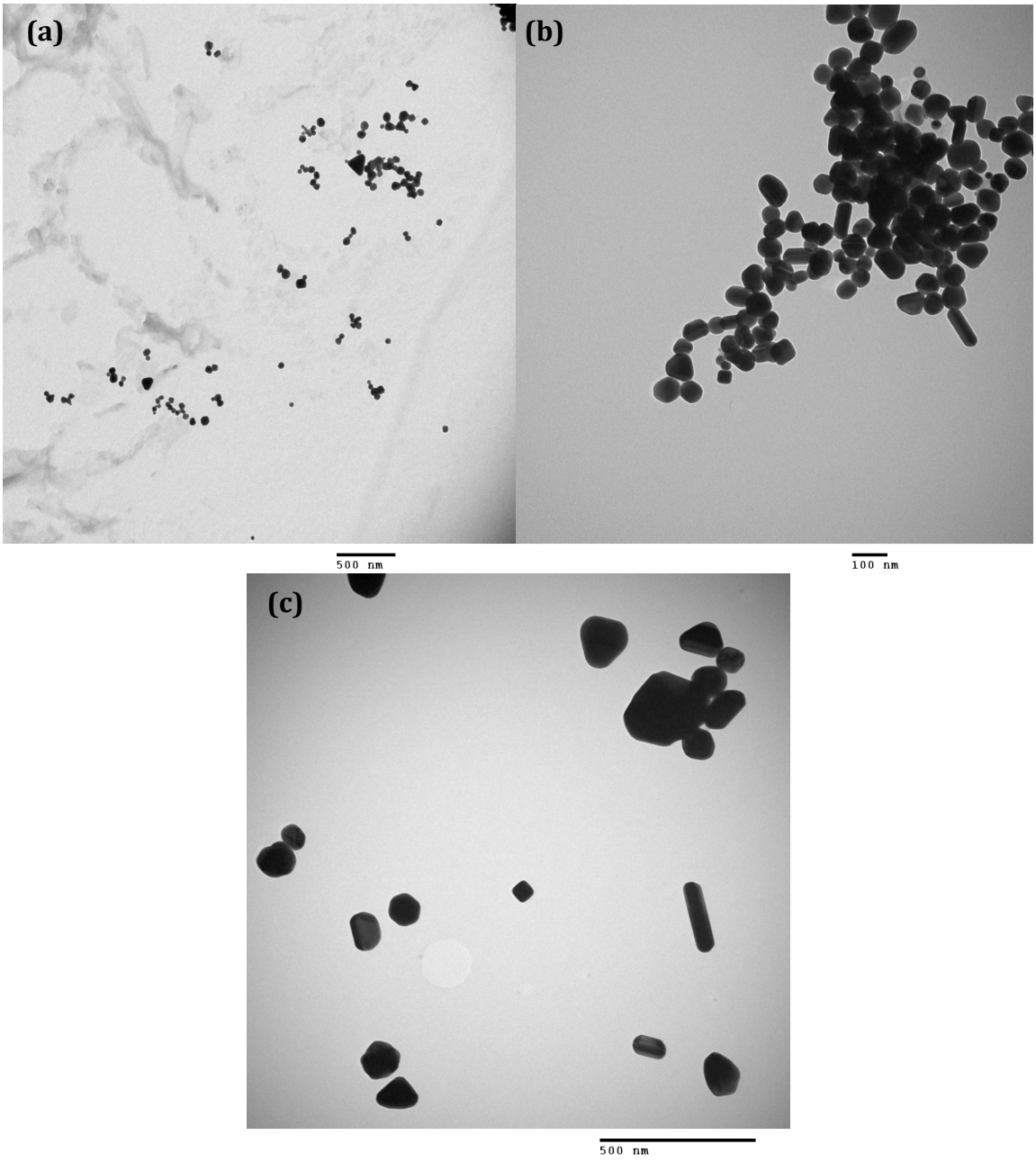

Figure 2.6: TEM images of different synthesis batches of Ag nanocubes following the protocol 2[147]. a) Exp-25, b) Exp-26a and c) Exp-26b.

Figure 2.7 shows the TEM images of the best result batch (Exp-27) synthesized using protocol 2. Figure 2.7c shows the size measurement of cubes present in image. All three images are from same batch but from different part (mesh) of grid. Figure 2.7 a and b have only 2 and 3 nanocubes, as sometime only a few particles are accumulated on a part of the grid and sometime plenty of particles accumulated at the same place, as in Figure 2.7c.

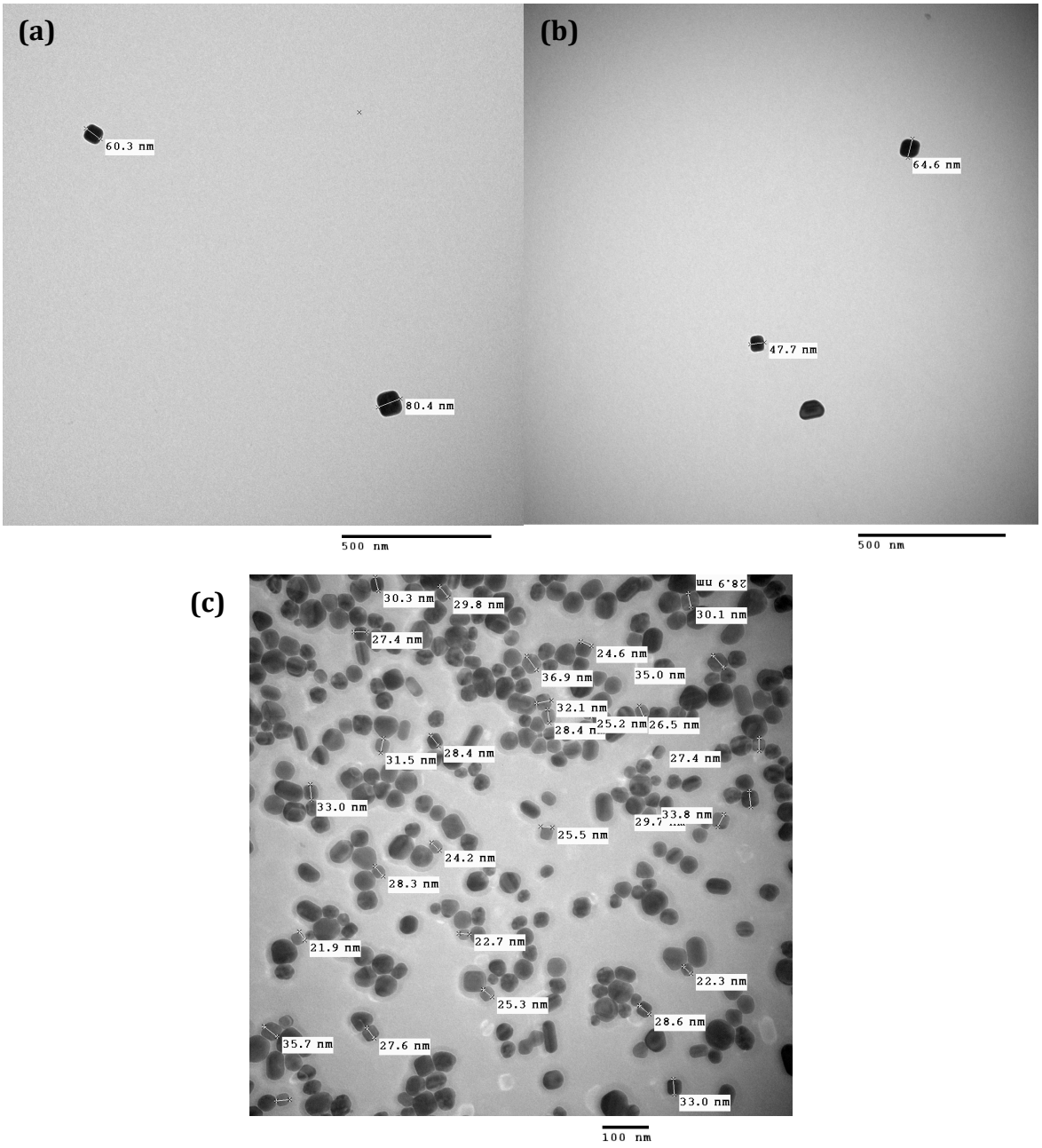

Figure 2.7: TEM images of Ag nanocubes fabricated using protocol 2 shows the size of nanocubes. (a,b and c) different images from same batch (Exp-27).

Figure 2.5 represents the silver nanoparticles synthesized by using $AgNO_3$ as silver precursor (protocol 1). Figure 2.5a confirms that most of the silver nanoparticles are nanorods with some other structures, but no nanocubes are present. Figure 2.5b and c shows nanorods that are lesser in number with most of the structures that are spherical.

Also the batches in Figure 2.5 b and c lacking nanocubes. Figure 2.6 represents the Ag nanoparticles synthesized by using CF_3COOAg as silver precursor (protocol 2). Initial batches (Figure 2.6 a, b) provide silver nanoparticles of different structures, but in the further batches, Ag nanocubes were present but in small numbers (Figure 2.6c).

Out of 38 synthesis batches, protocol 1 was used for initial 32 batches and last 5 batches were synthesized by using protocol 2. The difficulty we faced in using protocol 1 is the addition of sodium sulfide (Na_2S), as it is hygroscopic in nature. Therefore, addition of exact amount was difficult and we used 4 vials in one synthesis with all the other reactants in same number and amount but 4 different amounts (near to required amount) of Na_2S were added (different in each vial) as optimization to enhance the probability of addition of right amount. But even after trying 32 times we were only getting a few nanocubes, nanospheres and nanorods were the main yield. In the protocol 2 we used sodium hydrosulfide (NaHS), which is stable in comparison to Na_2S. After further optimization in the synthesis process (protocol 2), we were able to synthesize 25-30% Ag nanocubes with rest of the mixture containing different structures as shown in figure 2.7.

2.6 Conclusion

To use silver nanocubes as the templates in the synthesis of gold nanocages at least 95% purity is required. Yet after the synthesis of 38 batches (over a period of 4 months) using 2 different protocols, only 30% purity was achieved. At this point it was decided to abandon the synthesis of gold nanocages due to the challenges with optimizing the synthesis process. The reaction is very sensitive, according to Xia [146]. For example, Sodium sulfide (Na_2S) is highly hygroscopic. Therefore, there is an unavoidable uncertainty in the concentration of Na_2S, which may cause reaction to fail. There are many other critical steps in the synthesis, such as temperature control; injection of reagents to ethylene glycol may also cause reaction to fail.

Due to the sensitivity of the reaction, it was taking too long to optimize the protocol for higher purity nanocubes. Our priority in this project was to study the stability and contrast properties of AuNCs. Therefore, instead of investing more time on the synthesis of Ag nanocubes, a collaboration with Xia's Group (Georgia Tech) was initiated and nanocages of 40-45 nm size were acquired and used for the thesis work. Figure 2.8 shows absorption spectra of AuNCs used in thesis work.

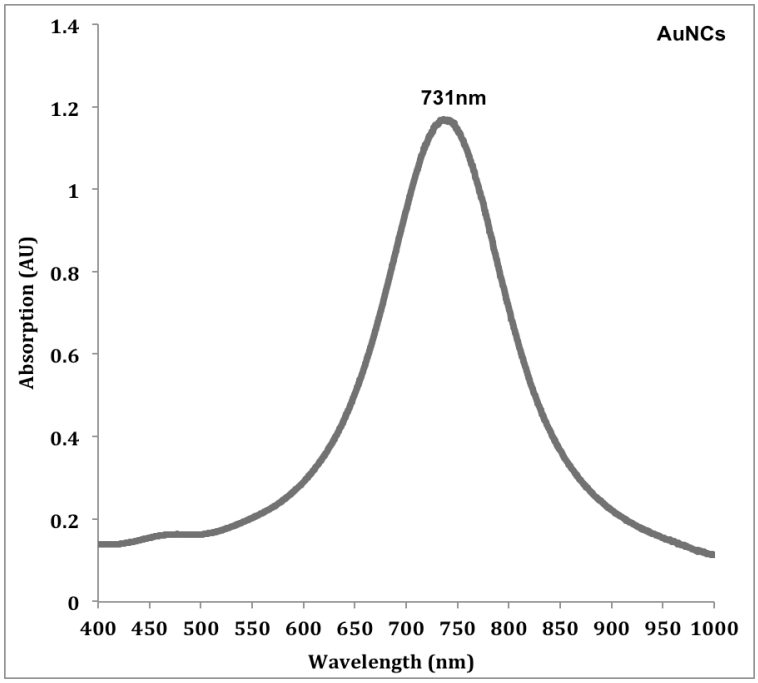

Figure 2.8: Optical absorption spectrum of gold nanocages.

Chapter 3: Stability Measurement of gold nanocages (AuNCs)

Gold nanocages are cubic hollow structures with porous walls with thickness of 5-7nm. Their localized surface plasmon resonance (LSPR) is tunable with the size. AuNCs used in this study are 45-50nm in size and have LSPR of 731nm. Due to small size and thin walls their stability against laser exposer is the point of concern. This chapter describes the stability study of AuNCs performed by illuminating them against different laser energies for different time periods.

3.1 Optoacoustic detection system

A prototype reverse-mode optoacoustic system (SENO Medical, San Antonio, TX) was used in this research work. A schematic of the device is shown in figure (3.1). This system operates at two wavelengths, 1064 nm (Nd: YAG) and 775 nm (Ti: Sapphire) with pulsed laser light (6 ns) coupled to a bifurcated fibre bundle. Maximum energy output falls between 50 and 200 mJ at both wavelengths. The output energy is controlled through a Q-Switch delay, whereby the shortest delay outputs the highest energy

Q-switching also known as quality switching is a method for generating intense short pulses (nanoseconds) of light with a laser. An Nd: YAG crystal is used as a lasing medium, which is optically pumped, by using a flash lamp to excite the atoms of the medium. Both ends of lasing medium have reflecting surfaces, which allows the wave to intensify as it moves back and forth across the active medium. This helps to increase the numbers of pumped atoms and produces a powerful “giant” pulse. In the Seno system, the laser output can be further adjusted through attenuator settings.

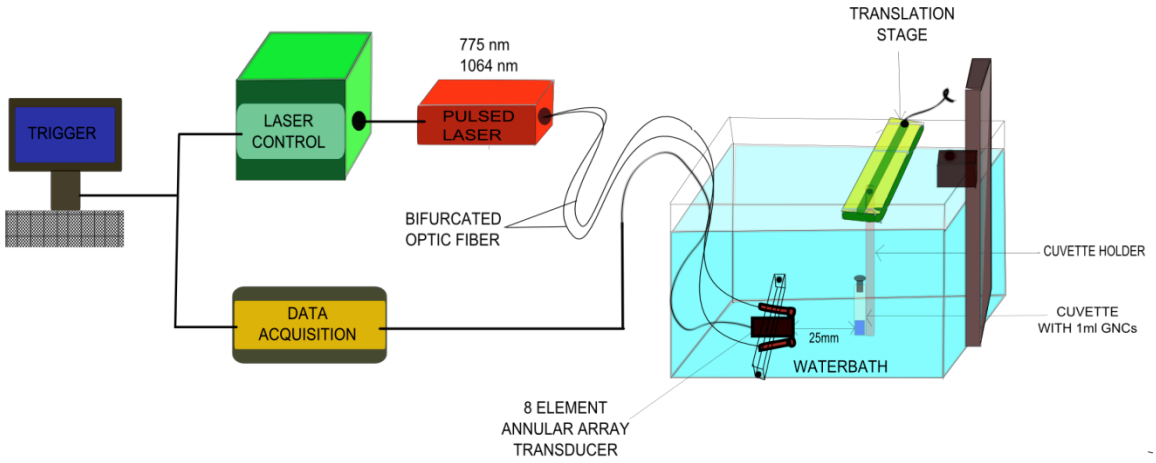

Figure 3.1: schematic representation of prototype reverse-mode Optoacoustic system. Bifurcated fibre bundle located on each side of transducer.

The output laser beam has a pulse width of 6 ns, repetition rate of 10 Hz and a beam diameter of 9 mm at 25 mm. A wavelength of 775 nm was selected for all the optoacoustic experiments. This wavelength is near to the optical absorption wavelength of gold nanocages (731 nm) used in this experiment. The American National Standards Institute (ANSI) sets clinical limits for laser exposure to humans. These limits known as maximum permissible exposures (MPEs) are set to be below hazardous levels. In clinical practice, it is suggested that the exposure level at the MPE may cause discomfort to patients[152]. The ANSI limit for 775 nm wavelength pulsed laser, with 6 ns pulse width, is 10 mJ/cm^2; for 1064 nm, the ANSI limit is 100 mJ/cm^2[153]. Figure 3.2 shows the Seno prototype OA imaging system we used in our lab. The transducer array, fibre bundles, camera and the sample are all submerged in a water-filled Plexi glass container for optimal acoustic coupling.

(a)

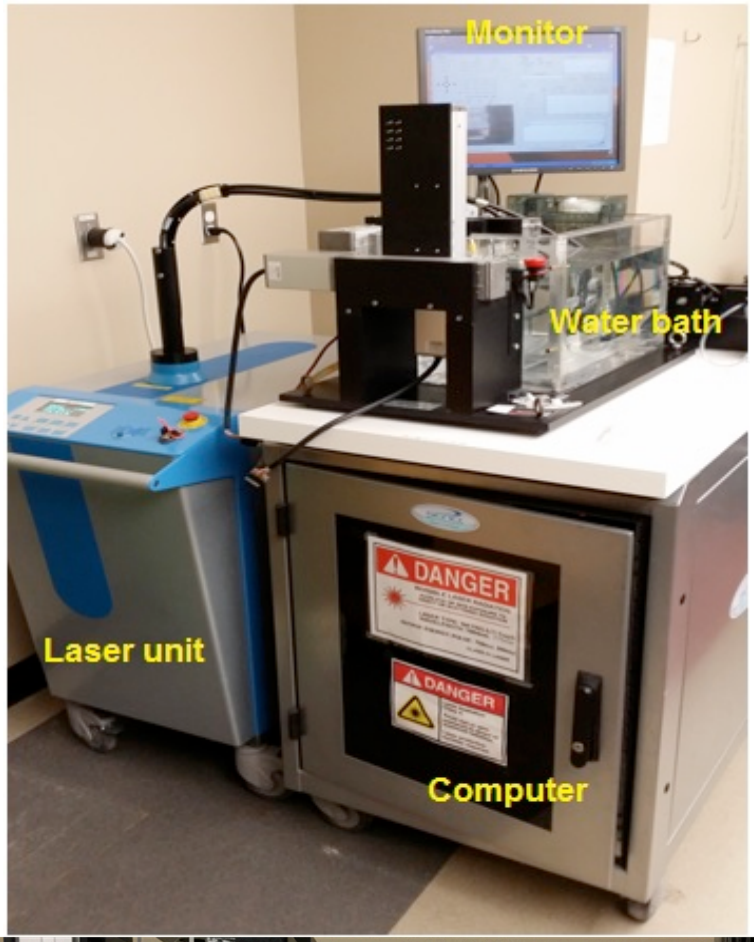

(b)

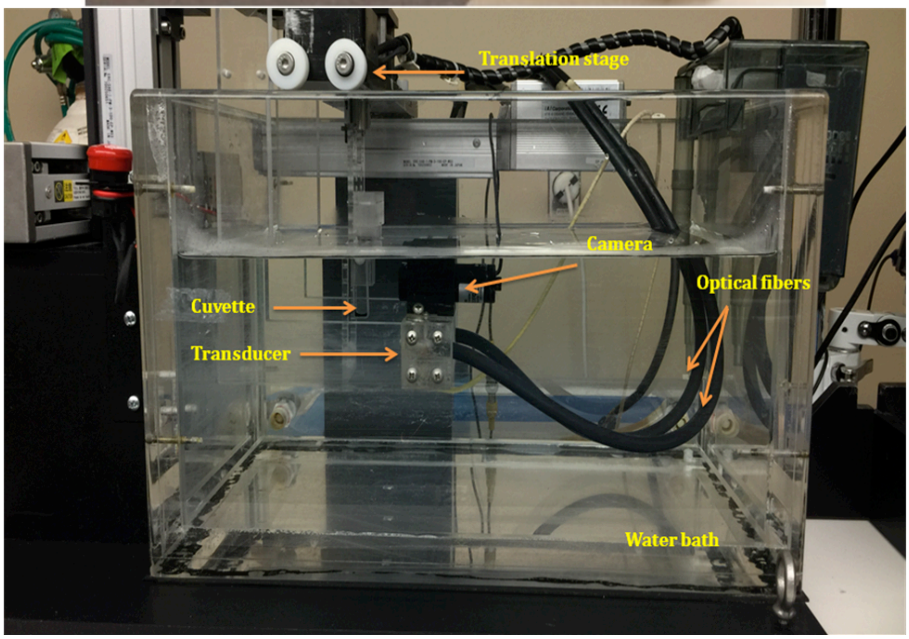

Figure 3.2: a) Seno medical optoacoustic imaging system, view of laser unit, water bath, computer and monitor, b) components of water bath.

An eight-element annular array wideband ultrasound transducer with a nominal central frequency of 5 MHz was used for OA detection. The transducer has a focal width of 0.5 mm, focal point at 25 mm, focal length of 10 mm (about the focal point) and a maximum depth of 60 mm (see figure 3.3). The transducer's focal point corresponds to where the laser beams from each fibre bundle intersect to give a maximum illumination diameter of approximately 9 mm.

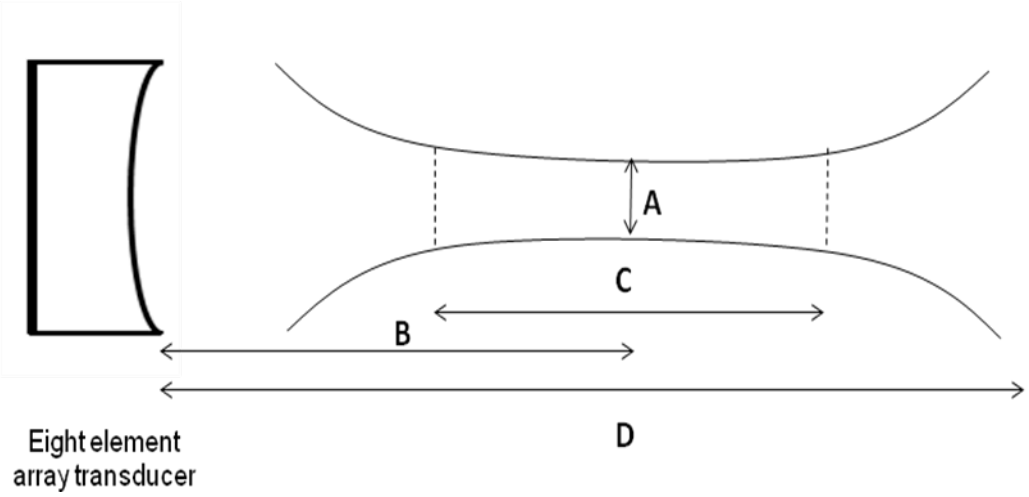

Figure 3.3: Schematic of eight-element annular array transducer response and parameters. A represents the focal width of transducer (0.5 mm); B is the focal point (25 mm); C is the focal length (10 mm) centered about the focal point; and D is the maximum depth (60 mm).

A cuvette (quartz) filled with gold nanocages was fixed to a holder and mounted on a translation stage which can be translated in X, Y and Z direction, under video guidance. The video camera and system motor (which moves both the camera and sample holder) are linked to the data acquisition system. The area of the sample to be scanned is known as a region of interest (ROI) and was selected within the focal length of transducer (25 mm, ± 5

mm from the transducer front). The value of X, Y and Z-axis of the ROI were then selected in their respective scan ranges. Selected ROIs were then scanned for the OA data acquisition.

The additional detection parameters to be selected before scanning includes the speed of sound, OA signal averaging, water bath temperature, time gain control and desired step size.

The laser energy from a Q-Switch laser system has the tendency to fluctuate (from pulse to pulse) and this phenomenon can affect the strength of OA signals. Illuminating one location of the sample with many pulses and averaging the number of OA signals can minimize fluctuations in OA signal due to variable input laser pulse energy. Signal averaging is helpful to improve signal to noise ratio but at the expense of longer scan times.

Optoacoustic targets, which are similar in size, shape, optical absorption and speed of sound, should yield the same OA signal strength no matter the depth. However, due to exponential light attenuation and the attenuation of the generated sound waves with depth, this is not achievable. Time gain controls (TGCs) are signal amplifications functions applied to the OA signals to compensate for these losses at depth[154]. The type of TGC function applied is dependent on the tissue of interest and the application. In this thesis, a TGC with constant amplification, at all the depth, was used for all experiments. Constant TGC was used because the attenuation profile for the cuvette used in our study was not known, such that, an appropriate TGC was not available. Therefore, a constant TGC was used such that, all the OA signals were amplified to a similar level.

Step-size is an important parameter in OA data collection, as it is related to the resolution of OA image. Step size indicates the distance between each OA signal acquisition location. The

smaller the step size, the better the overall resolution of the OA image. The Seno system has a step size range from 0.01 mm to 1 mm. Although the resolution is improved with smaller step sizes, this is at the cost of longer scan-times. A step size of 0.1 mm was used for all experiments as this generated an acceptable spatial data set for analysis.

The temperature of the water in the water tank can be controlled to mimic the temperature of the system of interest. For *in-vivo,* small animal, imaging studies, it is often required that the water remain at core body temperature to avoid shock. The water temperature can be changed and held at a desired temperature through a heater and water pump system. For the experiments in this thesis, the temperature of water bath was at room temperature (24^0C) as no *in-vivo* experiments were completed in this study.

3.2 Optoacoustic detection of gold nanocages

A cuvette holder as shown in figure 3.4, made up of Plexi glass was designed, fabricated and used to mount the sample cuvette with the translation stage. This holder was built specifically to hold a 10 mm path length cuvette. The cuvette fits perfectly in the socket and additionally there are two Teflon screws to fix the cuvette.

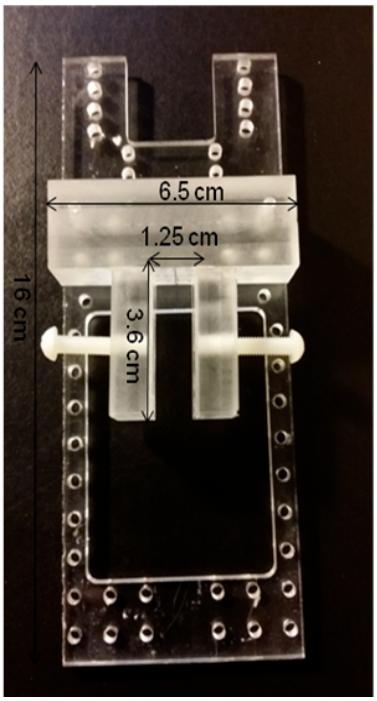

Figure 3.4: Cuvette holder (Plexi glass) with two Teflon screws to hold cuvette firmly.

Pre experimental work was completed to calculate the energy output from the fiber bundles, in order to set the energy level for illumination. All the experimental parameters required were set before each experiment. A screen capture of the graphic user interface (GUI) is shown in figure 3.5.

A constant speed of sound at 1.54 mm/μs and 775 nm (Ti: Sapphire) wavelength were used for all experiments. Two different energies, 10 mJ and 5 mJ were used.

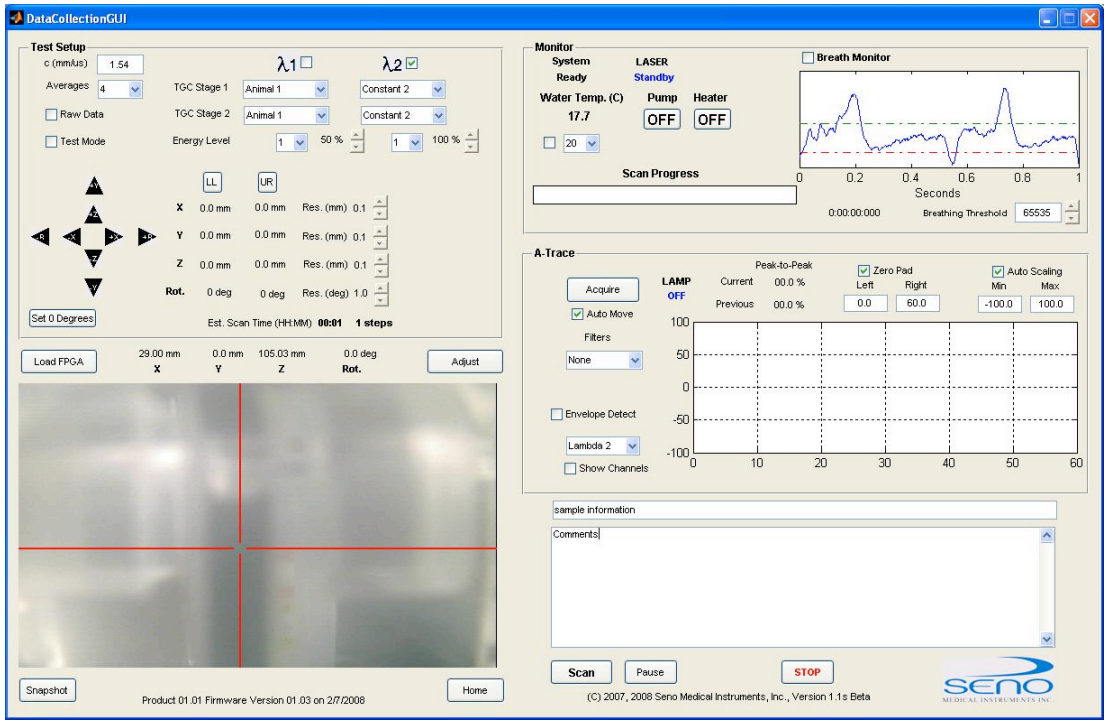

Figure 3.5: Data collection graphic user interface (GUI), with all the required parameters for OA data collection for stability experiment.

The cuvette filled with AuNCs (0.32×10^{11} particles/ml, 1 by 25^{th} of original AuNCs concentration, 8×10^{11} particles/ml) was sealed with paraffin to avoid leakage, and placed in the holder. The holder was then mounted on a translation stage. The scanning area (ROI) was selected to provide a scanning time little more than 5 min (which allows to stop illumination accordingly for 1, 3 and 5 min exposure time). No raster scanning (a pattern of closely spaced rows of dots that form an image) was done. The cuvette was filled to 10 mm level (1 ml of sample), so that the 9 mm diameter laser beam covered almost the whole volume, as shown in figure 3.6. First, with an energy of 10 mJ, three different AuNCs sample were exposed for 1 min, 3 min and 5 min and then the process was repeated for a 5 mJ energy; again with three different samples for 1 min, 3 min and 5 min.

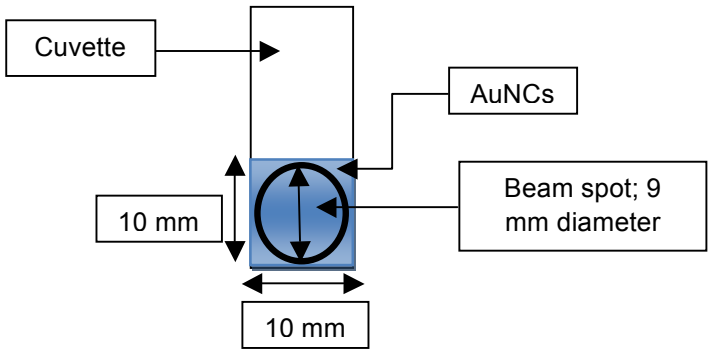

Figure 3.6: Schematic representation of AuNCs sample covered with 9 mm spot of laser beam.

Swirling of AuNCs sample during experiment was needed to avoid any sedimentation of gold nanoparticles and to ensure maximized exposure for all particles. The effects of swirling were investigated for 5, 3 and 1 min exposure. For the 5 min exposure, the illumination was paused twice, first after 90 seconds and then after 180 seconds. For the 3 min and 1 min exposure, the illumination was paused once, after 90 seconds and 30 seconds, respectively. Figure 3.7 shows the difference between swirled and non-swirled samples. A decrease in peak amplitude and a blue shift of the peak in the swirled AuNCs sample demonstrates that with the swirling process more particles were exposed to OA laser light. Further, the laser beams are typically Gaussian (characteristic symmetric "bell curve" shape) and hence the central region of the beam has a higher photon flux. All the AuNCs samples were swirled during the stability study.

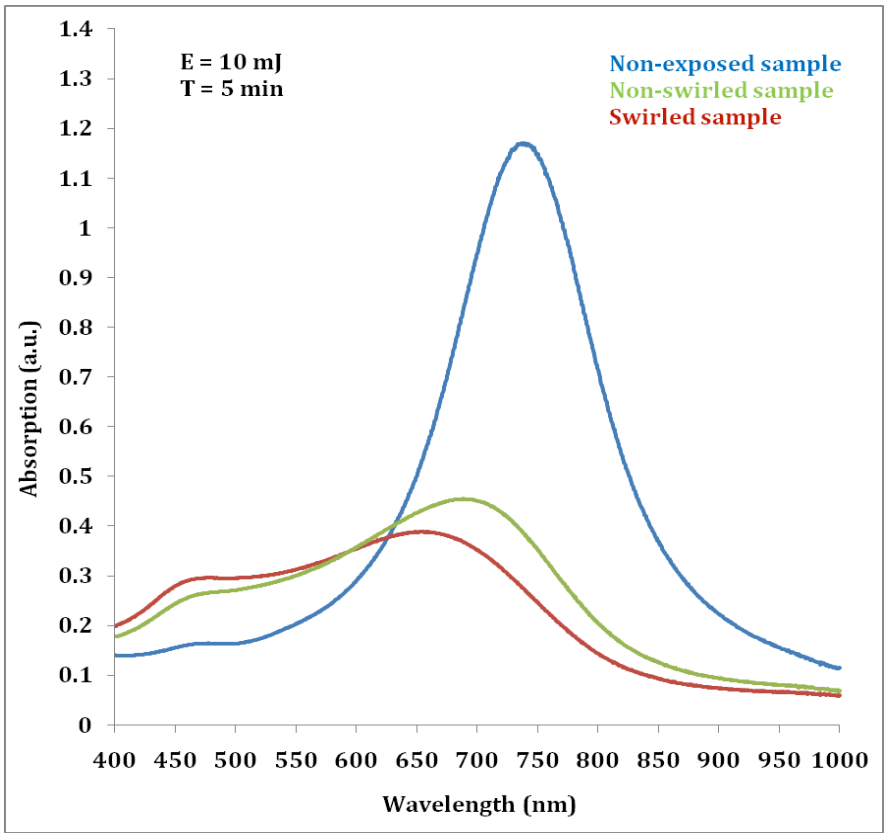

Figure 3.7: UV-Vis absorption graph showing the effect of swirling a gold nanocages in middle of exposure. Blue represents non-exposed AuNCs. Green represents the AuNCs sample, which was not swirled. Red represents the swirled sample.

Three methods were used to characterize the stability of AuNCs against pulsed laser light: optoacoustic detection, TEM imaging and optical absorption spectra. When all six AuNCs samples (3 sample at 10 mJ and 3 samples at 5 mJ) were exposed, 30 µl aliquots of exposed AuNCs were taken out from each cuvette for TEM imaging and the rest of the nanocages samples were diluted with DI water (equal amount of water was added to all the AuNCs samples) for UV-Vis absorption (to an acceptable concentration). For the TEM imaging, carbon coated grids were used and all the images were taken at 80 kV.

3.3 Results and discussion

3.3.1 Optoacoustic signal detection

This section of the thesis focuses on amplitude-based optoacoustic analysis to investigate the effects of laser energy and exposure time on AuNCs stability. OA data was acquired by exposing gold nanocages (0.32×10^{11} particles/ml) at 5 mJ and 10 mJ laser pulse energy for 1 min, 3 min and 5 min (separate AuNCs sample for each exposure time and for every repeat). The optoacoustic imaging system records data every second. Therefore, for 1, 3 and 5 min exposure, 60, 180 and 300 data points were generated, respectively. In this study, the OA signal is integrated over a time delay region (converted to distance) to give the area under the OA data curve. The Hilbert Transform is applied to all OA signals.

For Hilbert transform, data was exported to MATLAB (version R2009b. Natick, Massachusetts: The Math Works Inc., 2009) for individual OA signal inspection and analysis. The Hilbert Transform is a filter that changes the phase of the spectral component of a signal by 90° and it affects only the phase of the signal, has no effect on its amplitude. The original signal and its Hilbert Transform are orthogonal[155] to each other and have same intensity.

Figure 3.8 shows data for the first second of exposure of a gold nanocages sample exposed at 10 mJ for 1, 3 and 5 minutes, figure 3.8a, 3.8b and 3.8c, respectively. The box shows the cuvette (filled with AuNCs) positioned ~ 25 mm from the transducer array.

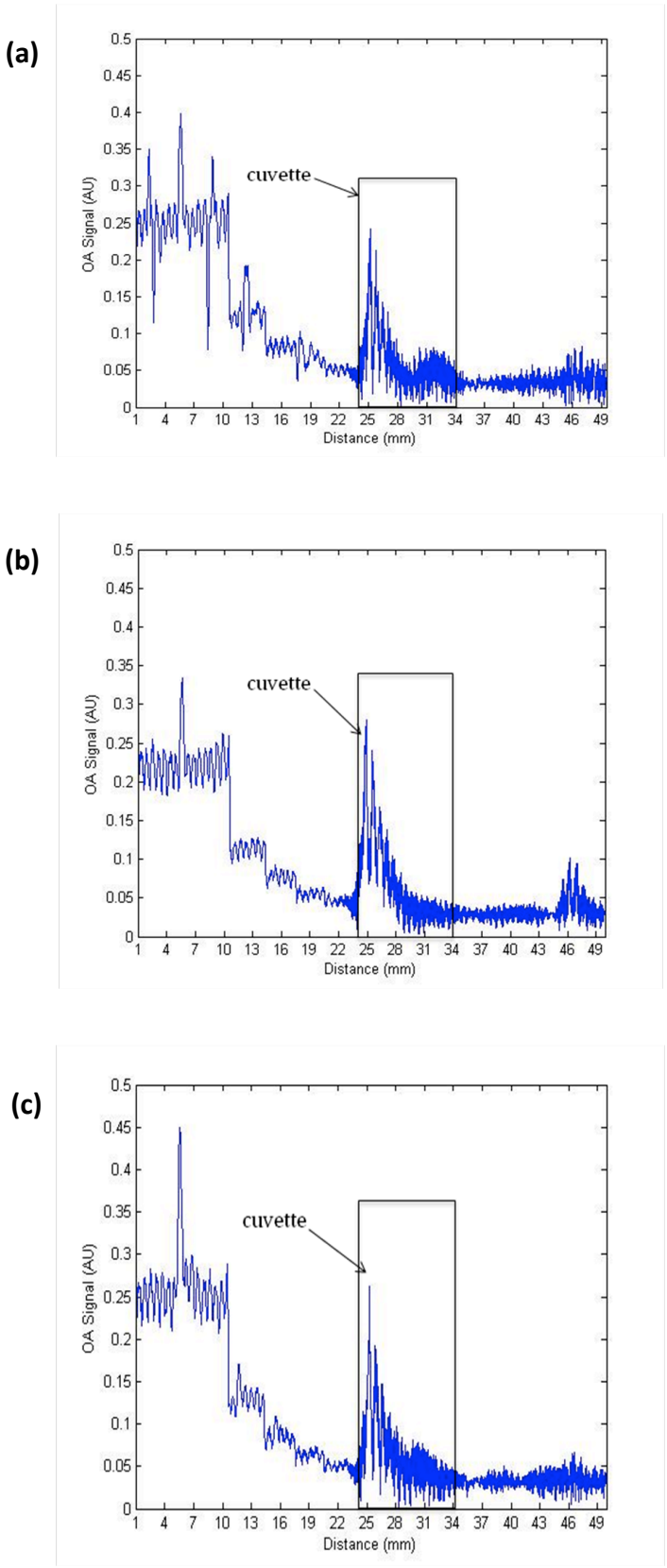

Figure 3.8: OA signals (obtained at t=1sec) from AuNCs exposed at 10 mJ for (a) 1 min, (b) 3 min and (c) 5 min exposure durations. Boxes are representing the position of cuvette from the transducer array.

The unusually higher OA signals prior to the cuvette region, from 0-20mm, are present. However, a constant TGC was applied which means all transducers should have similar amplification. The strong OA signals observed 1 to 20 mm from the transducer are emerging from water and, hence, must be artefacts. This is likely a result of a TGC firmware error.

Figure 3.9 (AuNCs exposed at 10 mJ laser energy for 5 min) shows OA signal over the length of cuvette (from 24 to 34 mm) at t = 1s (fig 3.9a) and at t = 300s exposures (fig 3.9b). This OA plot shows a reduction in OA signal at 300s compared to 1s, which indicates a change in the optical and thermo mechanical properties of AuNCs, results from the laser exposure.

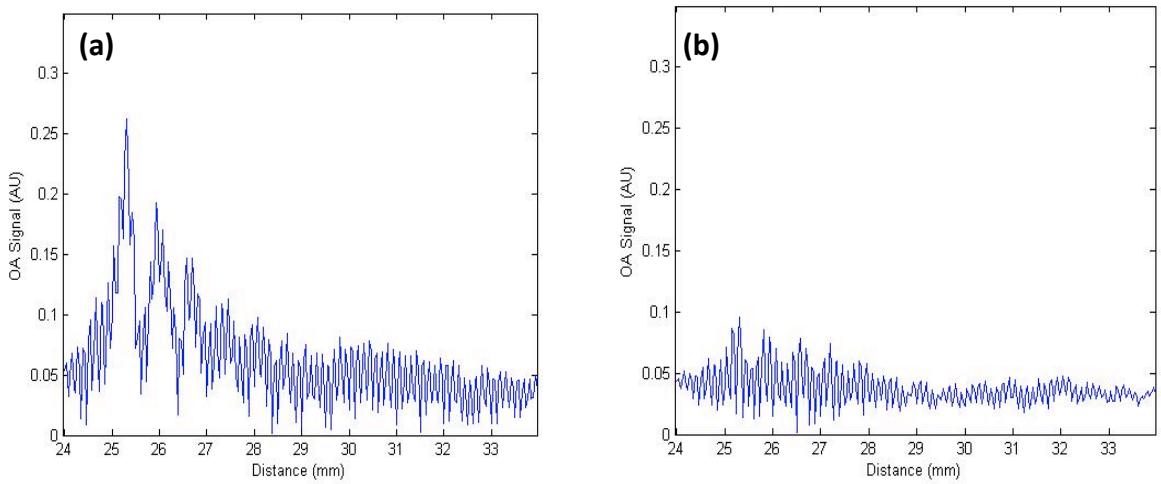

Figure 3.9: OA signal over the length of cuvette (24-34mm from the transducer). (a) at the first second of exposure (b) at the final (300th) second of exposure.

3.3.2 OA signal analysis

The OA signals within the range of the cuvette are integrated to give a single value representing the OA signal from the AuNCs. Figure 3.10 shows the OA signals versus time for 5 mJ and 10 mJ exposures. Figure 3.10a for 1 min, 3.10b for 3 min and 3.10c for 5 min exposure durations. Fig 3.10 shows a decrease in OA signal with exposure time. Error bars show the standard deviation, as three sets of each experiment was done.

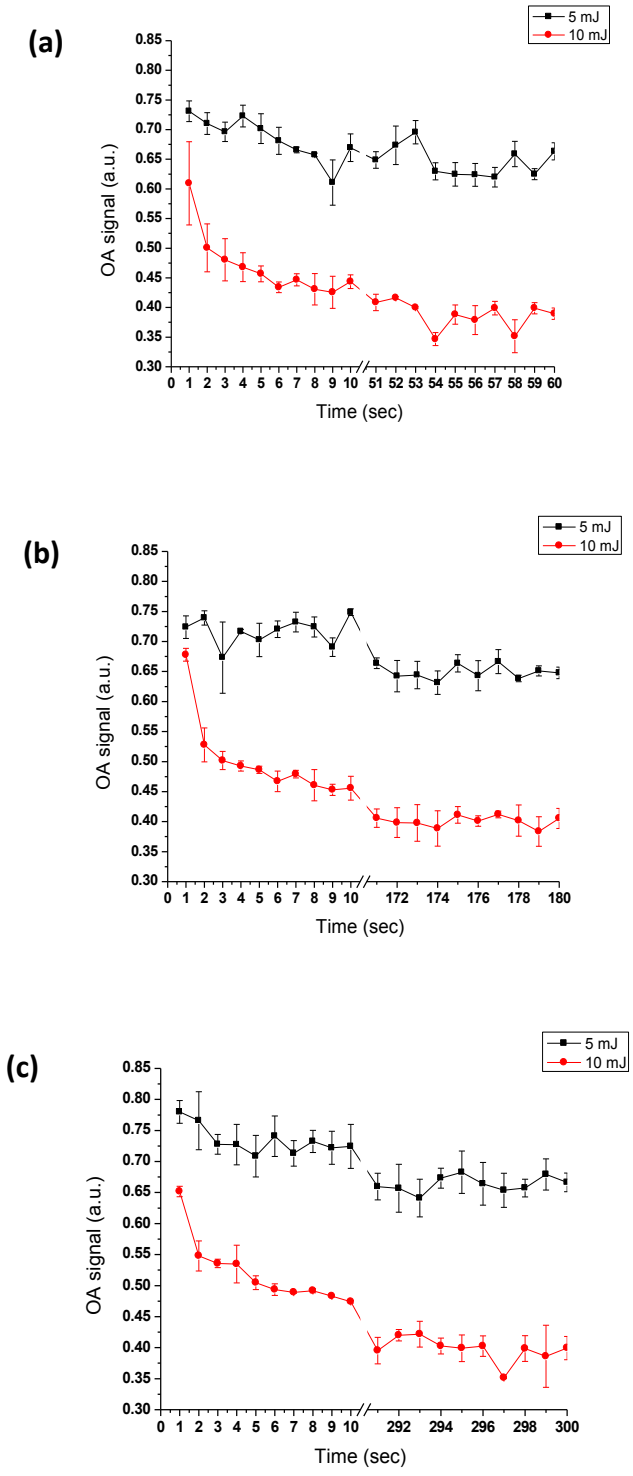

Figure 3.10: Area under curve versus time plot demonstrating the trend of OA absorption drop with time (two slots: initial and final 10 seconds) at two different energies (5 and 10 mJ) (a) 1 minute exposure (b) 3 minute exposure and (c) 5 minute exposure.

The data in fig 3.10 indicates that OA signals are greater for a 5 mJ energy pulse than for a 10 mJ energy pulse. This contradicts our understanding of OA wave generation as described by equation 1.3 in chapter 1. This is unexpected, because it is known that, higher pulse energy means more photons available to be absorbed. Therefore, the OA signals observed at the first second of exposure should be higher for the 10 mJ laser pulse energy. In this study, the OA system records data every second. Therefore the first data point shown in these plots is recorded after 1 second, which for our system corresponds to 10 laser pulses being delivered. Other studies have demonstrated that gold nanoparticles are damaged after 1 pulse at these high energies[156]. Therefore, data shown in figure 3.10 likely underestimates the overall effect of laser exposure on our AuNCs. The trends shown in figure 3.10 also demonstrates that maximum damage done in the initial 10 seconds and the final 10 seconds values shown in these plots are stable and constant for all three exposures sets (OA signal of 0.65 for 5 mJ and OA signal of 0.40 for 10 mJ pulse energy). It is also confirmed with TEM imaging and optical absorption data analysis, that damage at 10 mJ is greater than the 5 mJ pulse energy; therefore, due to the massive destruction at 10 mJ, the OA values for 5 mJ absorption after one second are higher than 10 mJ absorption.

Dependent Variable: score 5mJ

Source	DF	Sum of Squares	Mean Square	F Value	Pr > F
Model	3	0.19327200	0.06442400	38.80	<.0001
Error	176	0.29225740	0.00166055		
Corrected Total	179	0.48552940			

Table 3.1: The One Way ANOVA statistical measurement for 5 mJ energy exposure.

Dependent Variable: score10mj

Source	DF	Sum of Squares	Mean Square	F Value	Pr > F
Model	3	0.42880206	0.14293402	55.35	<.0001
Error	156	0.40281761	0.00258216		
Corrected Total	159	0.83161967			

Table 3.2: The One Way ANOVA statistical measurement for 10 mJ energy exposure.

The data shown in Table 3.1 and 3.2 correspond to the OA signal plots in figure 3.10. A One Way ANOVA was used to determine if the values of initial and final 10 seconds sets for all the experiments were significantly different and there are significant differences in the scores between exposures, and between the AuNCs samples (Appendix F & G). Calculated F-values are given in the Table 3.1 (5 mJ) and Table 3.2 (10 mJ) and indicate that OA signals from the first and last 10 seconds were significantly different.

3.3.3 TEM imaging analysis

TEM imaging was done to confirm the conformational changes in AuNCs exposed to laser pulses. High-resolution (HR) mode was used at 80 kV, a magnification of 50000x to 150000x was used to capture the images of AuNCs. Figure 3.11 shows TEM images of gold nanocages used in this study. All the AuNCs were cubical with sharp edges and corners, only a few other structures (≈5%), such as octagonal, triangle or spherical were present. Figures 3.12, 3.13 and 3.14 show TEM images of gold nanocages after 1, 3 and 5 minutes of exposures at 5 mJ respectively. The corresponding UV-Vis spectra are shown in figure 3.18a, b and c. Figures 3.15, 3.16 and 3.17 show TEM images of gold nanocages after the exposure of 1, 3 and 5 min at 10 mJ respectively. The corresponding UV-Vis spectra shown in figure 3.18d, e and f.

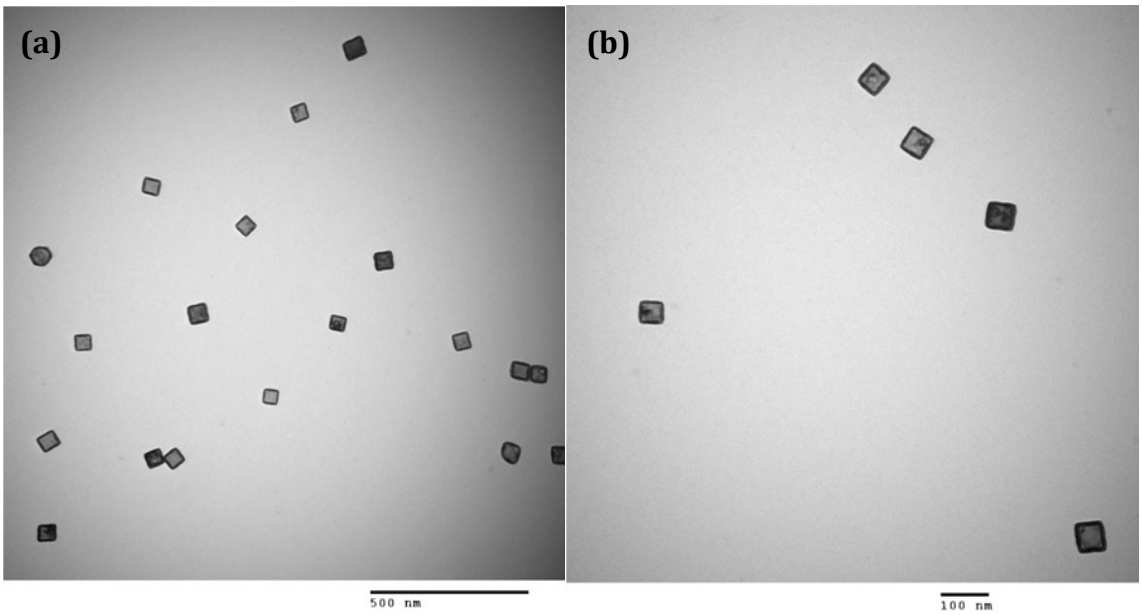

Figure 3.11: (a) TEM images of gold nanocages at 50000x magnification before the exposure to pulsed laser energy, (b) At 150000x magnification.

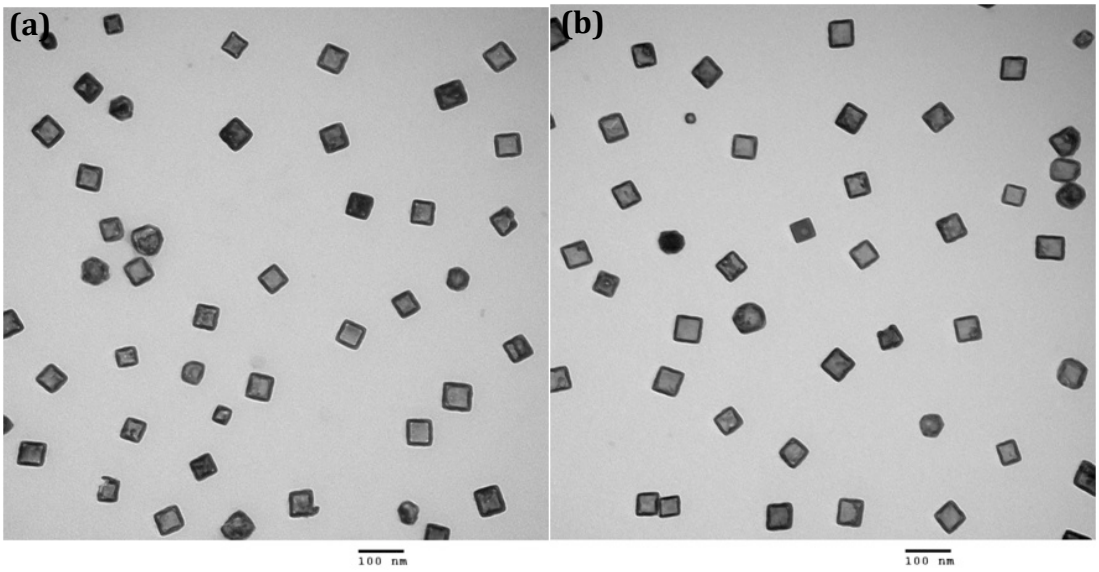

Figure3.12: TEM images of AuNCs exposed at 5 mJ energy for 1 min (a, b are images of the same sample from a different part of a grid).

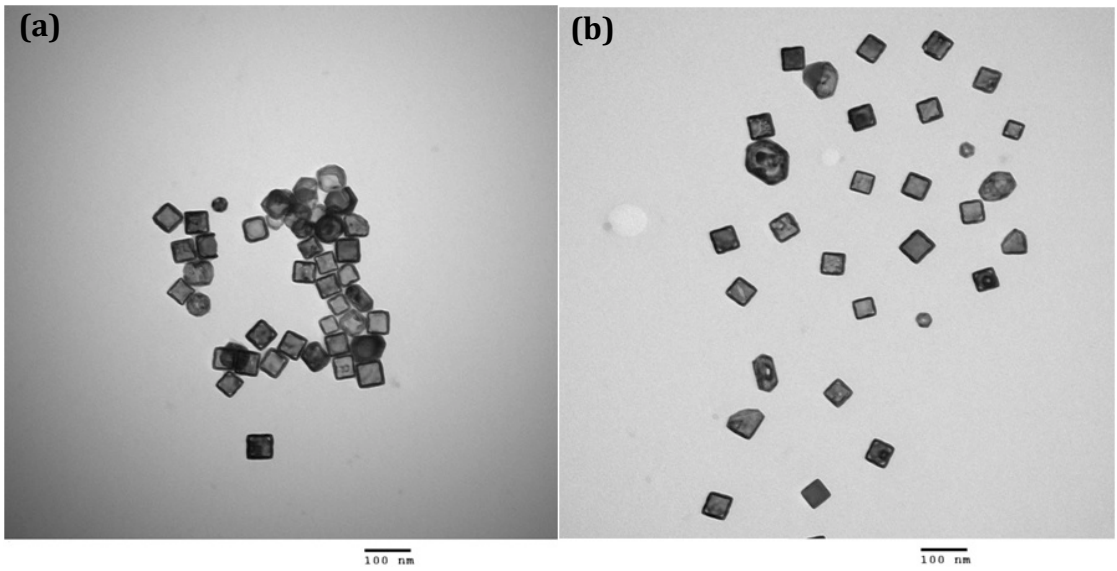

Figure 3.13: TEM images of AuNCs exposed at 5 mJ energy for3 min (a, b are images of the same sample from a different part of a grid).

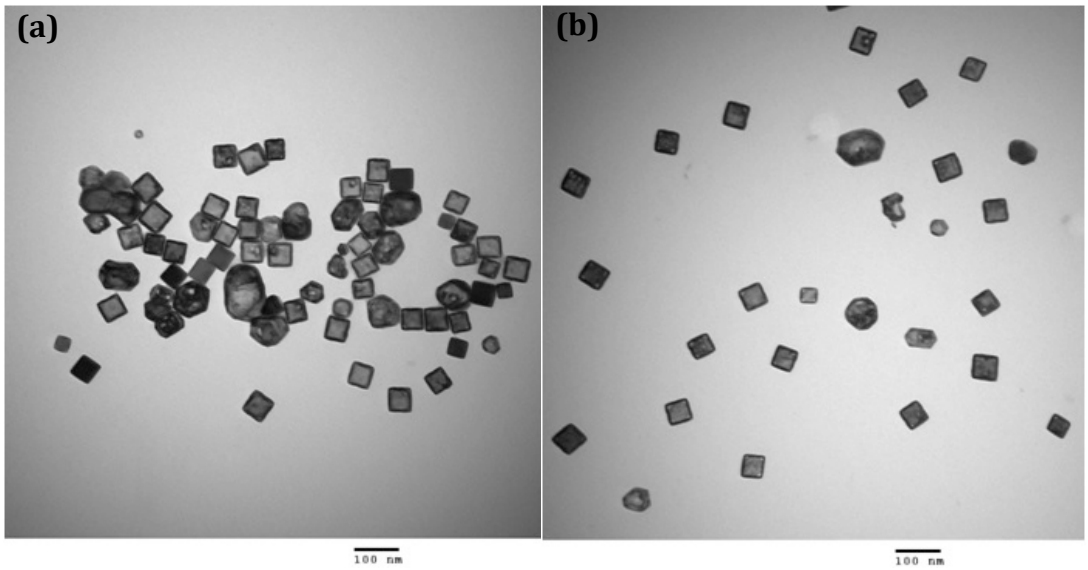

Figure 3.14: TEM images of AuNCs exposed at 5 mJ energy for 5 min (a, b are images of the same sample from a different part of a grid).

After the exposure at 5 mJ of energy, approximately 26% of nanocages lost their cubic shape after 1 min exposure; corners become truncated and the walls of the AuNCs started melting. The percentage values were calculated by manual counting each kind of structures with an individual TEM image of the exposed AuNCs. More structural damage is observed at 5 mJ laser energy for 3 and 5 min exposures. Most of the nanocages are melted (60-70%) and occupied a shape between cubic and sphere.

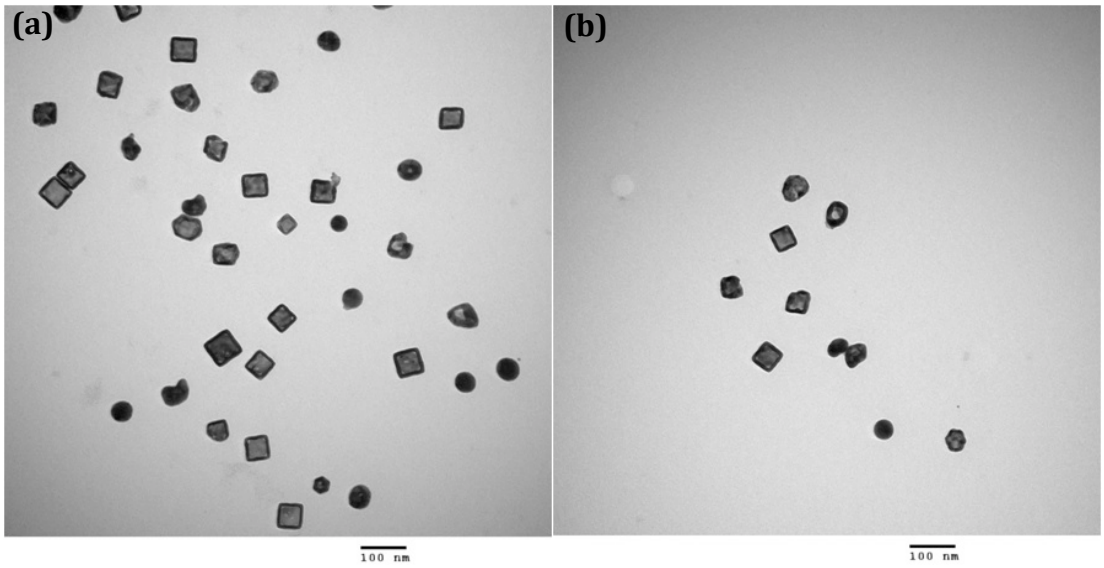

Figure 3.15: TEM images of AuNCs exposed at 10 mJ energy for 1 min (a) and (b) are images of the same sample from a different part of a grid.

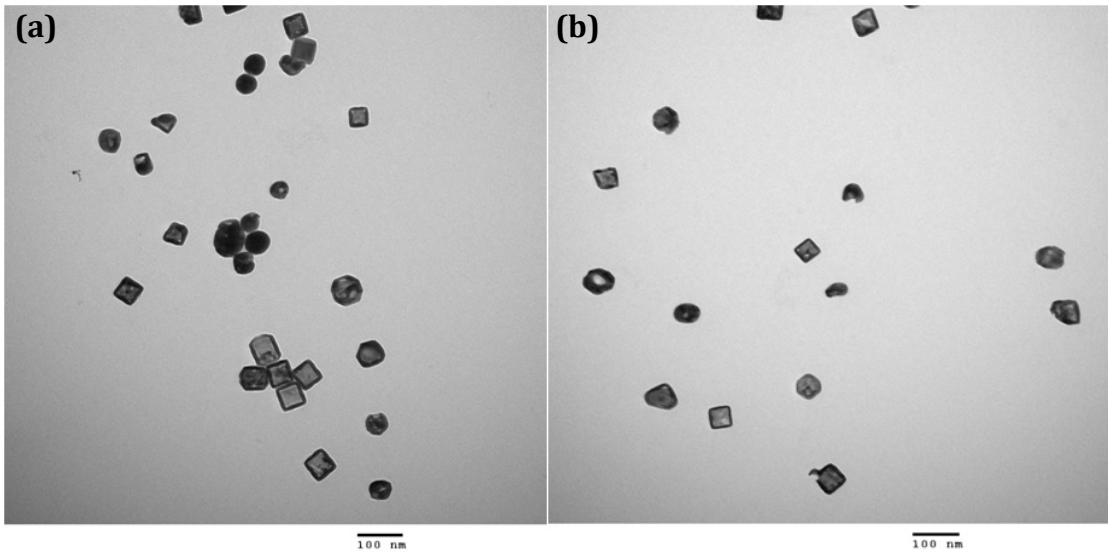

Figure 3.16: TEM images of AuNCs exposed at 10 mJ energy for 3 min (a) and (b) are images of the same sample from a different part of a grid.

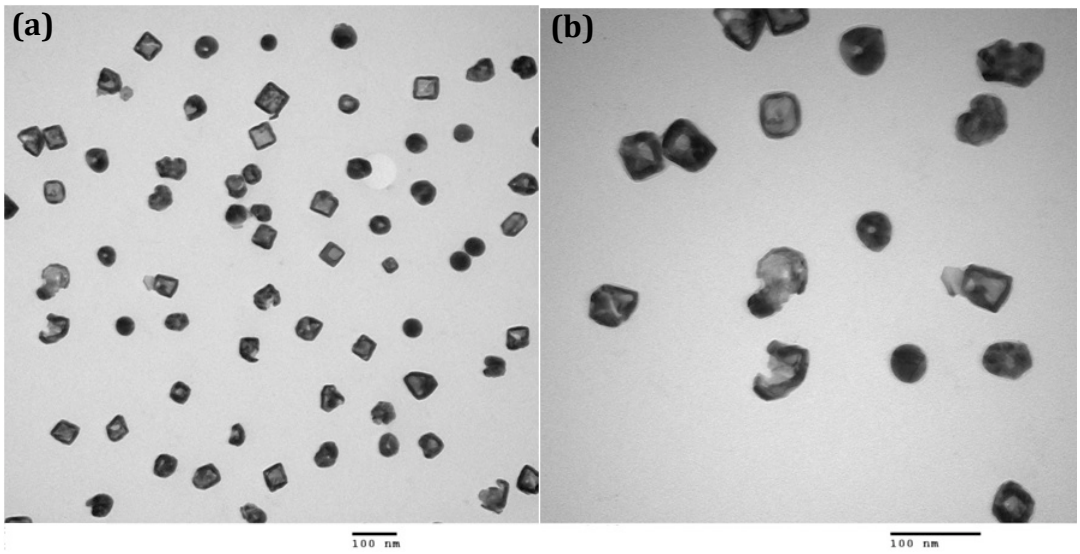

Figure 3.17: TEM images of AuNCs exposed at 10 mJ energy for 5 min (a) and (b) are images of the same sample from a different part of a grid.

Gold nanocages exposed to 10 mJ pulsed laser experience greater damage compared to the 5 mJ laser pulse. AuNCs exposed at 10 mJ for 1 min (figure 3.15) show approximately 58% damage. Exposure at 3 minute (figure 3.16) and 5 min (figure 3.17) shows approximate 80% and 91% damage, respectively. Around 20% to 50 % of the AuNCs turned spherical and fragmentation occurred for all three exposures times. Spheres and other structures, which are less than 20 nm in size, are due to fragmentation. This TEM imaging of exposed AuNCs is consistent with the optical absorption analysis. Optical absorption plots (Figure 3.18d, e and f), corresponding to the 10 mJ exposure showing a shift to the peak position and decrease in amplitude. The decrease in peak amplitude and shift of peak to the lower wavelength is related with melting and fragmentation of AuNCs, as LSPR depends on the shape and size of nanoparticles. Melting and fragmentation converted cubic nanocages into truncated AuNCs and in other structures between cube and spheres, change in peak position strongly depend on the aspect ratio[157].

3.3.4 Optical absorption spectra

Metal nanoparticles have unique optical absorption as a function of their size and shape. This concept has been used in this study to monitor changes in the LSPR to study the stability of AuNCs. Figure3.18 shows the optical absorption spectra for a 0.32×10^{11} particles/ml concentration AuNCs sample before and after the exposure at different energies (5 mJ and 10 mJ) for different time periods (1, 3, 5 min). Each experimental parameter set was repeated three times.

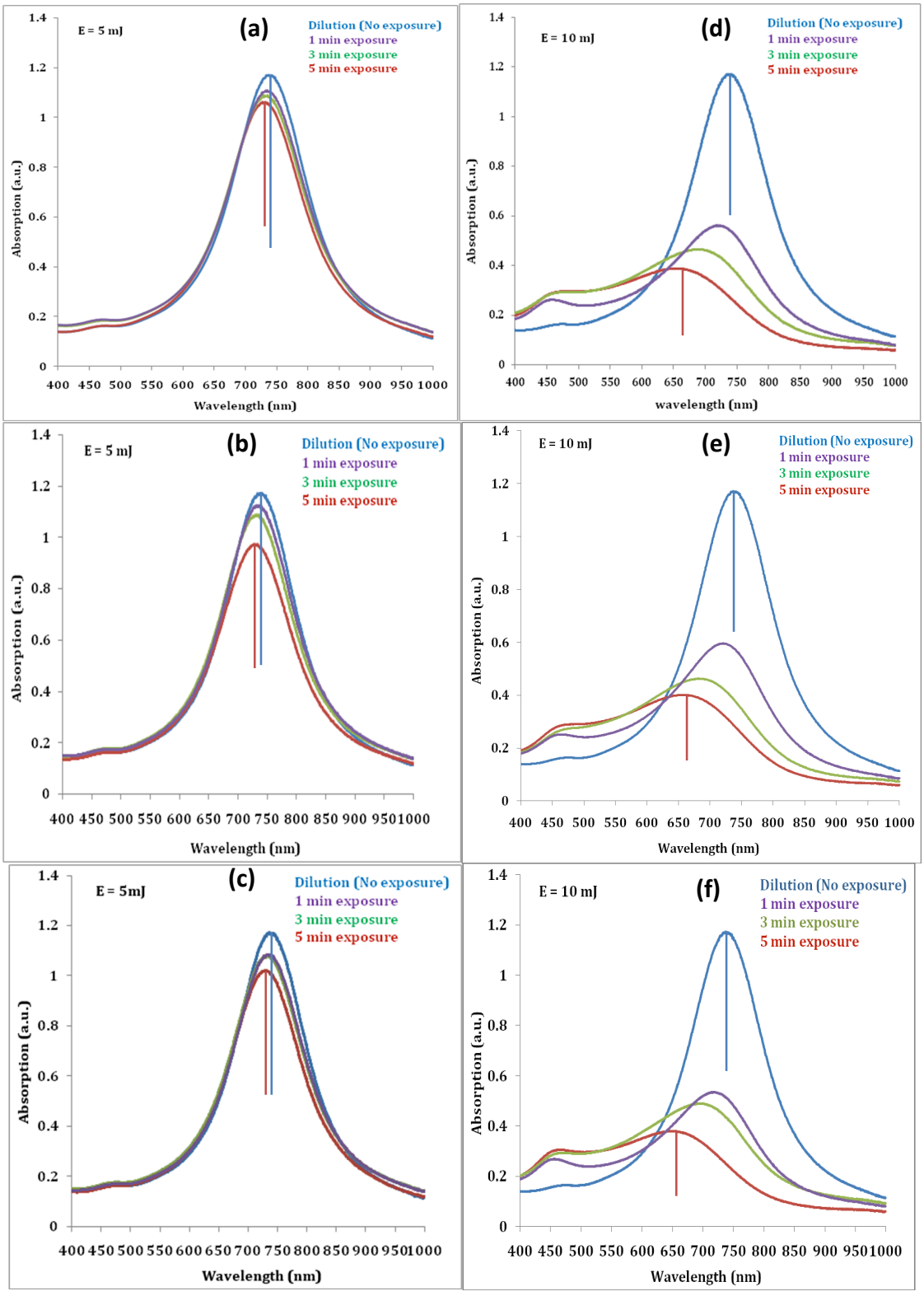

Figure 3.18: (a, b, c) Optical absorption spectra of AuNCs (0.32×10^{11} particles/ml) sample before and after the exposure at 5 mJ laser energy at 775 nm. (d, e, f) at 10 mJ laser energy at 775 nm for 1, 3 and 5 min. vertical lines are showing blue shift of peaks from non exposed sample to maximum exposed.

Figure 3.18a, shows the optical absorption graph for 5 mJ laser pulses. The decrease in peak amplitude is 5.6% for a 1 min exposure and 12.9% for a 5 min exposure. Blue shifts in the absorption peaks of 1.38 nm and 7.95 nm for 1 min and 5 exposures, respectively, are also observed. This experiment was repeated a total of three times and figure 3.18b and c are presenting optical spectra of two other repeats. Optical absorption data from all 3 experiments show similar trend, decrease in peak amplitude with increasing exposure time. A decrease in peak amplitude and blue shift in the peak for 5 mJ is comparatively less than 10 mJ energy (Figure 3.18d, e and f) but noticeable, and indicates conformational changes in AuNCs structure for a 5 mJ laser pulse.

Figure 3.18d shows the optical absorption of AuNCs exposed to 10 mJ laser pulses. For 1 min exposure time, the decrease in peak amplitude is 51.7% and for a 5 minute, the decrease is 66.7%. Blue shifts in the peak absorptions of 16.7nm and 82.91nm for 1 min and 5 min exposures, respectively, are observed. A decrease in peak amplitude, a blue shift and a small bump at 450 nm (gold nanoparticles of approximately 30 nm in size have LSPR at 450 nm)[158] are indicating conformational changes in AuNCs. There are two possible theories for such conformational changes in gold nanocages. First is a result of AuNCs melting due to a generation of substantial internal heat after absorbing laser energy. Second is the fragmentation of AuNCs into smaller pieces after their reshaping. These conclusions are drawn from the research work of S. Link et.al[159] and M. Gordel et. al[160] on the reshaping of gold nanorods. According to Link and Gordel, laser fluence in the order of 0.25 Joule cm^{-2} can melt the gold nanoparticles and higher laser fluence $\sim$ 1 Joule cm^{-2} can fragment the gold nanorods after melting. Link *et al.* also demonstrated that nanosecond pulses can cause fragmentation and femtosecond pulses can cause melting[161].

Figure 3.19 shows the peak optical absorption values (and standard deviations for the 3 repeated experiments) for the AuNCs as a function of exposure time and laser pulse energy. Figure 3.19a and 3.19b show a trend of decreasing peak amplitude at 5 mJ and 10 mJ of energy, respectively. Table 3.3 presents an overview of the changes in the peak amplitude and in wavelength observed for 5 mJ and 10 mJ laser pulses. The change in peak wavelength was calculated by subtracting the peak wavelength for the exposed AuNCs with the peak wavelength for the non-exposed AuNCs. And the percent change in peak amplitude was calculated by averaging 3 values of peak amplitude, divided by peak amplitude of non-exposed AuNCs sample and multiplied by 100.

$$[Peak\ amplitude_{\ exposed} / Peak\ amplitude_{\ non\text{-}exposed} \times 100] \quad (3.1)$$

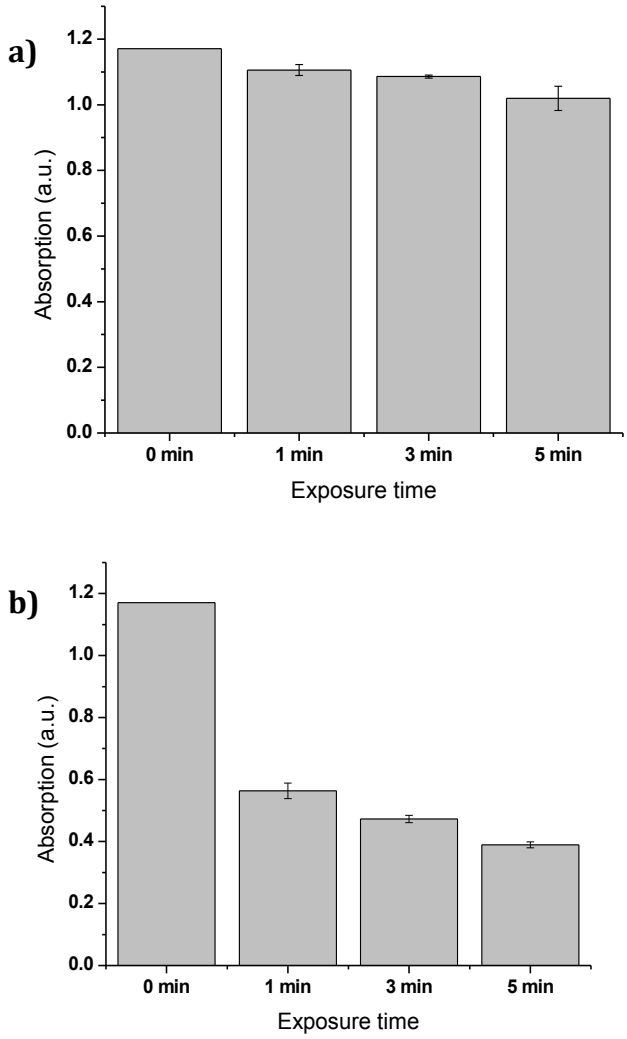

Figure3.19: Peak optical absorption changes as a function of laser exposure duration for a) 5 mJ laser pulse and b) 10 mJ laser pulse.

Exposure time	Average percentage change in peak absorption (±1SD)	
	5 mJ laser pulse	**10 mJ laser pulse**
1 min	5.57 ±1.38	51.7 ±2.20
3 min	7.20 ±0.35	59.6 ±0.99
5 min	12.9 ±3.15	66.7 ±0.80
Exposure time	**Average shift in the peak wavelength (nm) (±1SD)**	
	5 mJ laser pulse	**10 mJ laser pulse**
1 min	1.38±0.23	16.7±1.31
3 min	4.75±0.98	49.0±5.52
5 min	7.95±1.07	80.0± 0.23

Table 3.3: Calculated average change in peak amplitude (from optical absorption graphs) and shift in the peak of AuNCs exposed at 5 and 10 mJ.

The findings indicate that gold nanocages are not stable. During the optoacoustic imaging, gold nanocages were exposed to nanosecond laser pulses of 5 mJ and 10 mJ. The nanocages absorbed a portion of the light and generate substantial heat that leads to nanocages reshaping and an associated reduction in absorption cross-section. This theory is based on previous work [162][163][164][156] shown for melting of nanospheres and nanorods to occur at significantly lower temperatures than bulk melting of the metal [MP of bulk gold is 1064^0C, MP of nanogold (>5nm) is 750-800^0C][165], in part because surface reorganization processes dominate.

The data is consistent with much of the damage occurring in the first second of exposure. TEM data indicate that melting occurred at 5 mJ while both; melting and fragmentation were observed at 10 mJ.

Since results from the 5 mJ energy illumination demonstrate conformational changes in AuNCs, a lower energy, 2.5 mJ, was also tested by exposing AuNCs for 5 minute. Optical absorption data for the AuNCs used in this experiment are shown in figure 3.20, and demonstrate no change in absorption. This indicates that, threshold energy required to damage AuNCs used in this research is higher than 2.5 mJ.

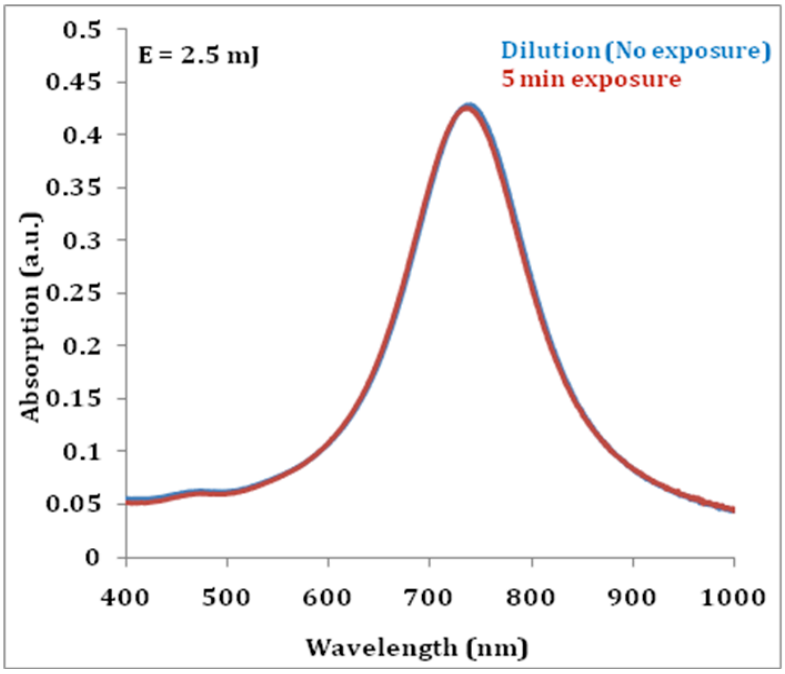

Figure 3.20: Optical absorption plots of AuNCs, before and after the exposure at 2.5 mJ energy.

3.4 Conclusion

In conclusion, we can say that, 5 mJ and 10 mJ laser pulse energy can be problematic for in-vitro studies, as AuNCs losing their primary structure on direct exposure. Furthermore, change in structure can cause a change in OA signals. However, AuNCs can be still used for tissue imaging due to optical attenuation, because most of the light is absorbed or scattered while travelling through a medium.

Chapter 4: Contrast study of gold nanocages (AuNCs)

This chapter includes the preparation of liquid phantom using 1% Intralipid as scattering material and Naphthol green dye as absorber and contrast study of AuNCs using this phantom with different absorption coefficient. The AuNCs stability study in Chapter 3 shows that AuNCs are not stable at 5 mJ and 10 mJ laser exposures. Therefore this phantom study is important to find out their stability when light reached the nanocages after crossing a background medium and to find out their contrast properties.

4.1 Tissue mimicking phantoms

4.1.1 Overview

In medical imaging, phantoms are imaging specimens of known geometric and material composition and are commonly used in the development and characterization of imaging system or algorithms[166]. A tissue-mimicking phantom emulates important properties of biological tissue for the purpose of providing a more clinically realistic imaging environment. Depending on the imaging modality, certain physical properties are of critical importance when constructing a tissue-mimicking phantom. In the case of OA imaging, optical absorption and scattering are two of the most important phantom parameters.

The magnitude of a generated OA signal is related to both the local fluence and optical absorption at the signal-generating source (e.g., blood or plasmonic nanoparticles). Consequently, optical scattering is the dominating optical loss mechanism in soft tissue and becomes important when attempting to achieve biologically realistic local fluence[166]. Scattering also increases the turbidity of a medium, which tends to increase the irradiation volume. Optical absorption tends to be a much less significant loss mechanism in tissue

(when compared to optical scattering), but it does play a critical role in the generation of OA signals. For example, aortic tissues have an optical scattering coefficient of 315 cm^{-1} and an optical absorption coefficient of 0.52 cm^{-1} at 633 nm[167]. The primary endogenous optical absorber in deep tissues are oxygenated hemoglobin (between 10 cm^{-1} and 100 cm^{-1} in the range of 400 nm to 1300 nm)[168] and deoxygenated hemoglobin (between 2 cm^{-1} and 105 cm^{-1} in the range of 400 nm to 1300 nm)[168]. Both optical scattering and absorption have strong wavelength dependence in tissue. To introduce absorption at a specific wavelength, colored dyes are commonly used in phantom preparation, To introduce scattering, Intralipid solution or polystyrene beads are frequently utilized[169][170]. Intralipid is a liquid soybean emulsion that is commonly available in 10% and 20% concentrations. It has been used as a scattering medium in many OA studies[171][172].

Gel phantoms are more commonly used for OA imaging but liquid phantoms prove to be more useful when target positions are to be varied.

4.2 Materials and method

4.2.1 Intralipid phantom preparations

In this study a 1% Intralipid stock solution was used as the scattering medium and Naphthol green dye as the absorbing medium to prepare phantoms. A 1% Intralipid dilution was prepared from a 20% Intralipid stock solution. A 1% Intralipid was selected for this study because its optical properties are well characterized[173]. A 10 ml stock solution of 0.2% Naphthol green was prepared. Different depths of the OA target with in a tissue equivalent background were investigated. But, instead of varying physical depth, the optical depth was varied. A 5 mm layer of Intralipid phantom at front of cuvette sample was used for all the experiments and the optical depth was varied by adding a fixed amount of Naphthol green dye to the background. Optical depth approach was chosen to ensure the target is at the same distance from the transducer for all the experiments as such the transducer response is the same.

Based on the absorption coefficient (μa) range of soft tissues, phantom solutions with six different absorption coefficients were prepared. The list of the phantoms are given in table 4.1 including 1% Intralipid alone (no absorber) used as the seventh phantom.

Phantom	Composition of background medium	μ_a (desired)of background medium
1	11,142 µl 1% IL + 858 µl NG	$\mu_a = 4\ cm^{-1}$
2	11,574 µl 1% IL +426 µl NG	$\mu_a = 2\ cm^{-1}$
3	11,682 µl 1% IL + 318 µl NG	$\mu_a = 1.5\ cm^{-1}$
4	11,790 µl 1% IL + 210 µl NG	$\mu_a = 1.0\ cm^{-1}$
5	11,898 µl 1% IL + 102 µl NG	$\mu_a = 0.5\ cm^{-1}$
6	11,984 µl 1% IL + 16 µl NG	$\mu_a = 0.1\ cm^{-1}$
7	12,000 µl 1% IL + 0.0 µl NG	$\mu_a = 0.03\ cm^{-1}$ (1%IL only)

Table 4.1: Composition of 1% Intralipid and Naphthol green required for desired μ_a of phantom at 775 nm.

To calculate the required amount of Naphthol green needed to prepare a phantom with a desired μ_a, the following equation was used:

$$\mu_{a\,(NG)} = \ln(10) \times \text{Absorption (absorption of NG, 0.01\% at 775 nm)} \quad (4.1)$$

$$\mu_a\,(\text{water}) \times (V_T \times V_{NG}) + \mu_{a\,(NG)} \times V_{NG} = \mu_a\,(\text{desired}) \times V_T \quad (4.2)$$

where NG stands for Naphthol green, V_T for total volume, V_{NG} for volume of Naphthol green and μ_a (desired) is the desired absorption coefficient of the phantom.

The optical absorption of Naphthol green stock solution was measured using a spectrometer (Cary-50). The absorption at 775 nm wavelength was used for the above calculations, as a 775 nm wavelength was used for the OA detection. A stock solution of 0.2% NG was prepared and it was further diluted to 0.01% to measure optical absorption. Total volume of each phantom was 12 ml (total volume of box is 15ml, we chose a lower limit to avoid overflow of liquid due to the insertion of cuvette into the box). The μ_a of water

at 775 nm is 0.024 cm^{-1}. The absorption of Naphthol green (0.01%) at 775 nm was 1.21, used for all calculations.

4.2.2 Target: Gold nanocages

Three different AuNCs concentrations, 8.0×10^{11} particles/ml (original concentration), 2.7×10^{11} particles/ml and 1.6×10^{11} particles/ml were used as the optoacoustic targets in this study. These two dilutions, 1 by 3rd (2.7×10^{11} particles/ml) and 1 by 5^{th} (1.6×10^{11} particles/ml) were prepared by adding appropriate amount of DI water in a portion of original concentration solution of gold nanocages.

4.2.3 Intralipid box

A Plexi glass box (20 mm x 20 mm x 40 mm) was built from a 2 mm thick Plexi glass sheet. The box has only one opening (7.5 mm x 12.5 mm) on the top to pour in phantom material (Intralipid, Naphthol green dye) and to position the 5 mm pathlength cuvette (Quartz, WPI). The distance between the front wall of cuvette and the inner wall of Plexi glass was 5 mm, which provides for 5 mms of 1% Intralipid + Naphthol green dye in front of the cuvette. As shown in figure 4.1, the box was attached with a platform, which was fixed to the translation stage.

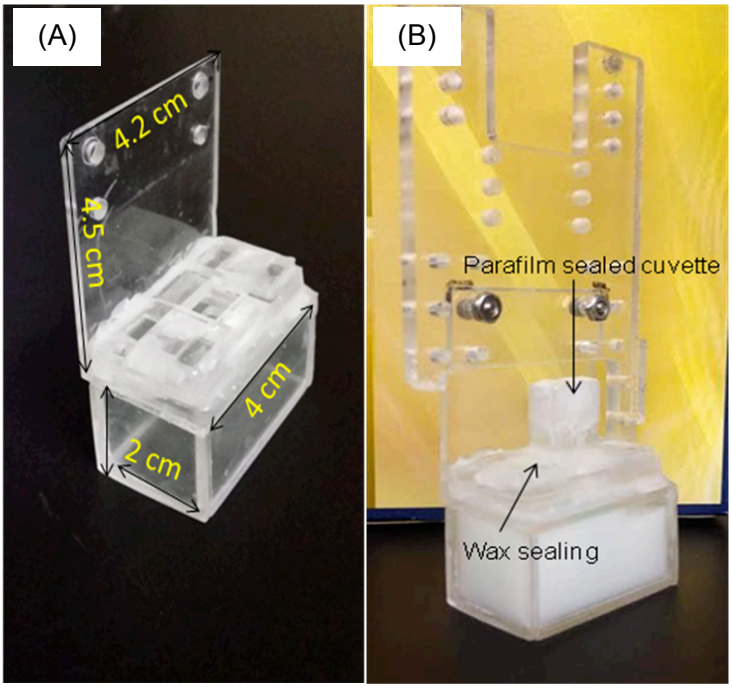

Figure 4.1: (A) Plexi glass box. (B) Box filled with 1% Intralipid phantom; attached with the platform with two screws, cuvette placed in the slit and sealed with paraffin wax.

4.3 Optoacoustic phantom

First, the plexiglass box was filled with the Intralipid + Naphthol green phantom mixture using a single opening at top, then the sample cuvette was sealed with parafilm and inserted into the box through the same opening. The box was then sealed with paraffin wax (Figure 4.1b) to avoid any mixing of water with phantom. Finally, the box was fixed to translation stage of the OA system. Figure 4.2 shows the OA scanning path.

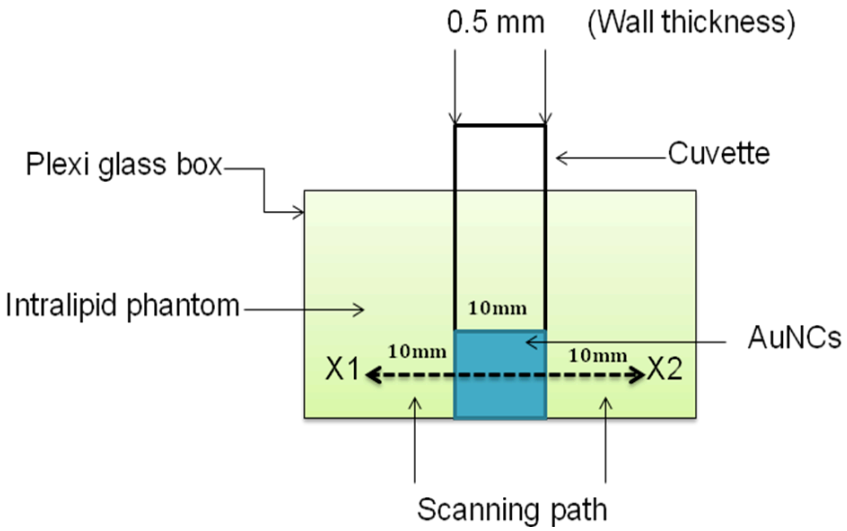

Figure 4.2: Schematic of Intralipid box with cuvette, dashed arrow showing scanning path from X1 to X2 (31 mm).

Three different AuNCs concentrations and a water (blank) target for seven phantoms with different absorption coefficients were used for a total of 28 experiments.

4.4 Phantoms optoacoustic detection

OA data was collected using a reverse-mode optoacoustic imaging system (Seno medical). The phantom was exposed to 10 mJ optical pulses at 775 nm. The time gain control (TGC) was set to constant and a 0.1 mm step size was used for all the experiments. The laser/transducer head scanned across a defined path, 31mm (which includes the thickness of cuvette walls), across the full width of the cuvette target and into the surrounding liquid background for a total of 311 OA measurement points.

4.5 Results and discussion

Figure 4.3 shows a schematic of the scanning path and representative Hilbert transformed OA signals at 5 selected points along the path. The asterisk marks (1-5) represent five specific points whose corresponding OA signal are shown in Figures 4.3b to 4.3f, respectively. Asterisk 1 is the start point and 5 represents the end point of the scanning path the total distance travelled by the OA transducer is 31 mm. Figure 4.3 demonstrates how OA signals changes as the transducer crosses the AuNCs filled cuvette. Figure 4.3d shows the highest OA signal intensity, as the AuNCs particles are illuminated by entire laser beam diameter such that a maximum number of gold particles are exposed.

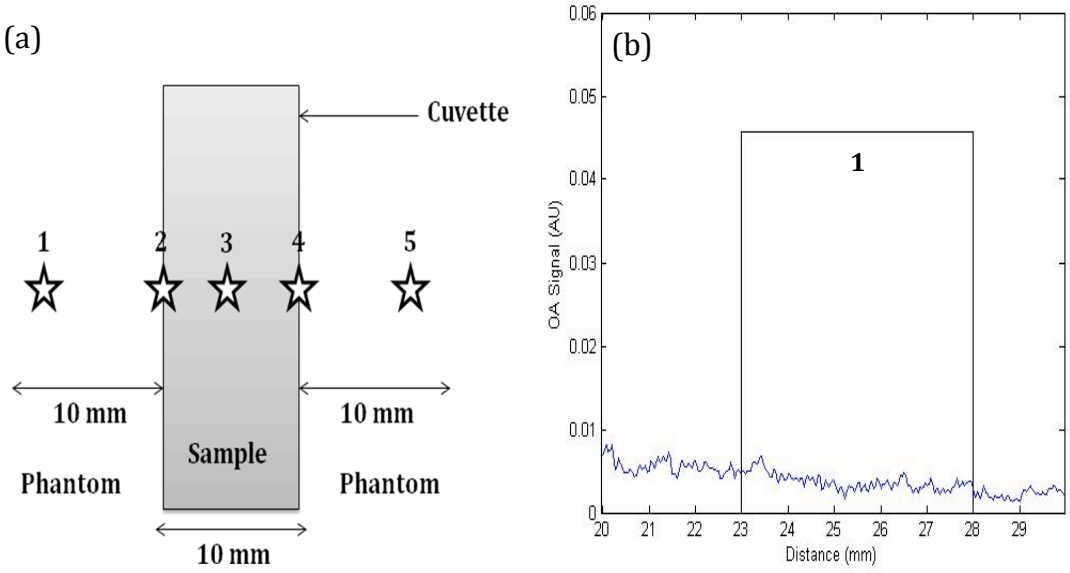

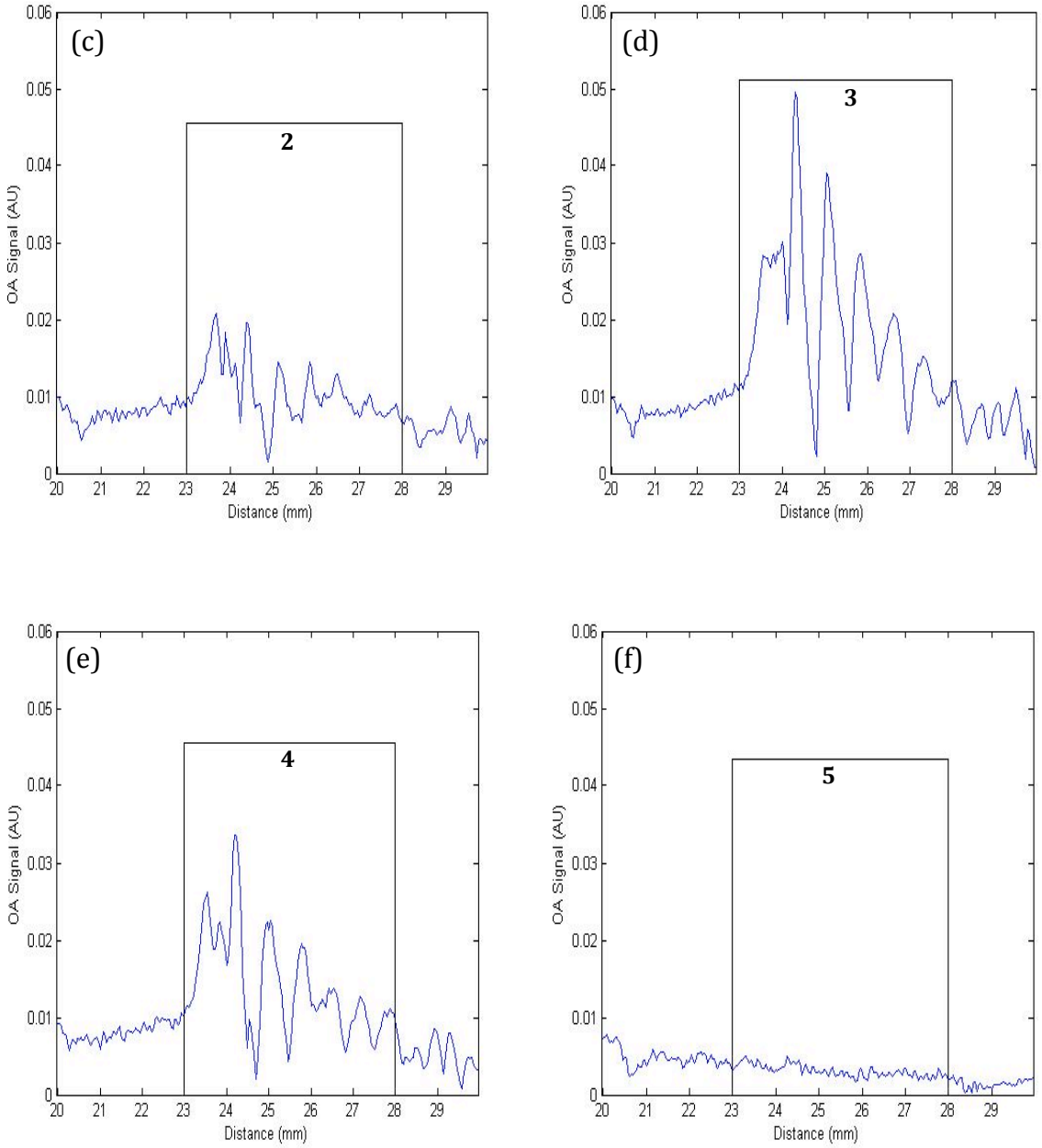

Figure 4.3: (a) schematic of the scanning path, stars are showing the different points whose corresponding OA signals are shown in b, c, d, e and f. The boxes in the figure b, c, d, e and f are representing the position of cuvette and the numbers written in boxes are showing the related data point (figure a).

Figure 4.3b and 4.3f are symmetrical and demonstrate minimum signal intensity because the entire laser beam was directed away from the cuvette, to the left and right, respectively. Figure 4.3c and 4.3e should exhibit symmetry as in both cases the laser beam is partially covering the AuNCs filled cuvette. However, the observed lack of the symmetry difference in the number of AuNCs particle exposed at these two points.

4.5.1 Effect of background medium and AuNCs concentration on OA signal amplitude

Figure 4.4 shows OA signals from three different AuNCs particle concentrations (8.0×10^{11} particles/ml, 2.7×10^{11} particles/ml and 1.6×10^{11} particles/ml) in the seven different background phantoms investigated.

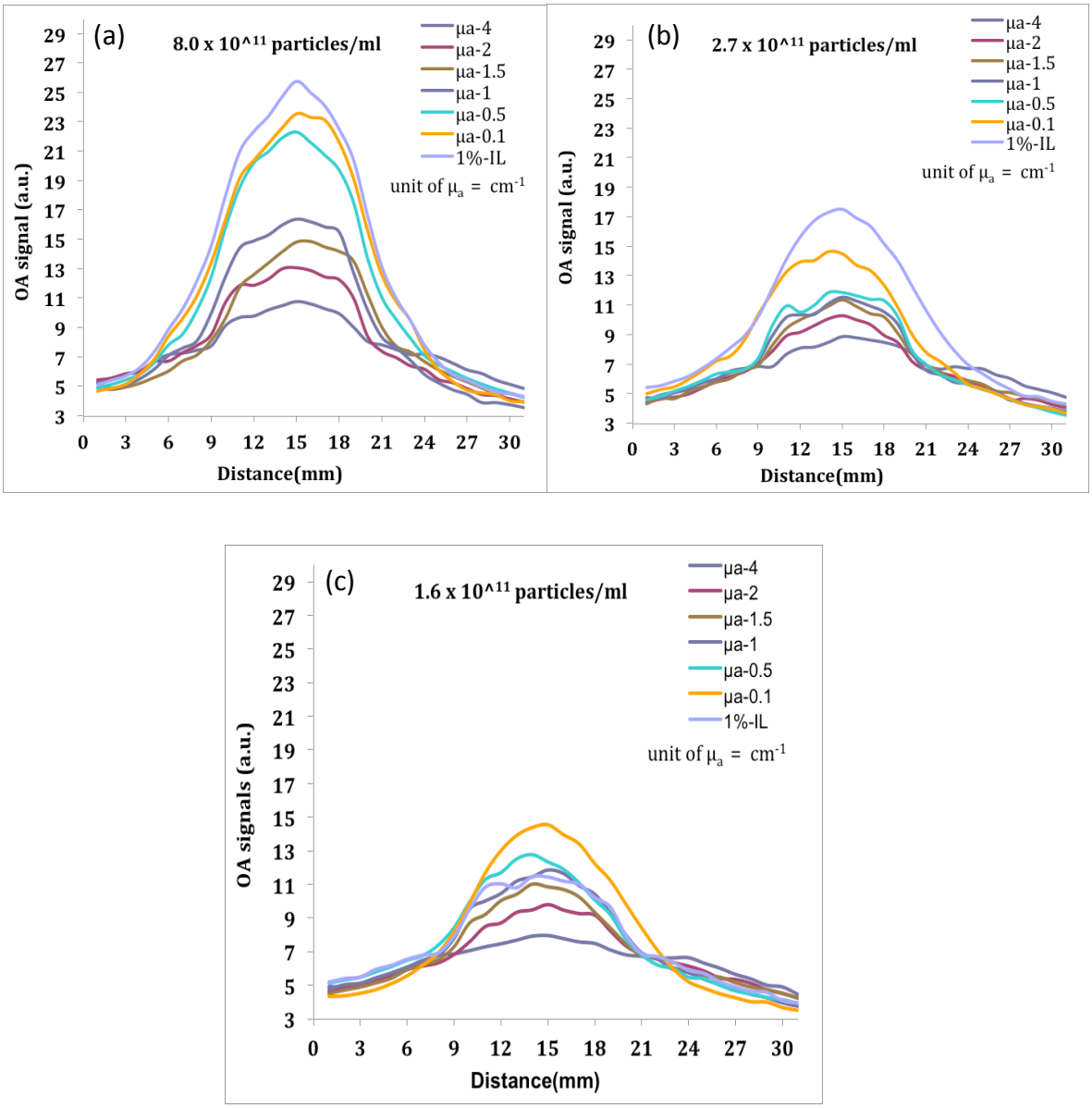

Figure 4.4: OA signals as a function of scanning path for all 7 optical backgrounds investigated for target concentrations of (a) 8.0 ×10^{11} particles/ml, (b) 2.7 × 10^{11} particles/ml and (c) 1.6 × 10^{11} particles/ml.

Data shown in figure 4.4 demonstrate the effect of AuNCs concentrations and changing background absorption on the OA signals. An OA signal amplitude of 11.41 was observed for 1.6 × 10^{11} particles/ml in a 1% Intralipid background and the OA signal increased with

increasing AuNCs concentration. The peak OA signals for 2.7×10^{11} particles/ml and 8.0×10^{11} particles/ml are 17.49 and 25.77, respectively, for the same 1% IL background. Table 4.2 shows all the peak OA signals corresponding to the data shown in figure 4.4. The effect of increasing μ_a (absorption coefficient) in the background is also observed clearly. The peak OA signal decreases with increased background optical absorption. Figure 4.4 shows that the peak OA signal is greatest for the 1% Intralipid background alone, as there is no added absorber. And the OA signals for AuNCs in a highly absorbing background ($\mu_{a=}4cm^{-1}$) are the lowest for all concentrations. The exception is for 1% IL at the lowest AuNCs concentration (figure 4.4c). This is likely due to a cuvette positioning error such that the distance between cuvette and transducer was not consistent and the orientation of the cuvette may not have been vertical. This error does not appear to be present in the other data sets.

Background Absorption (μ_a) (cm^{-1})	AuNCs Concentrations (particles/ml)		
	1.6×10^{11}	**2.7×10^{11}**	**8.0×10^{11}**
	Peak OA signals (a.u.)		
0.03(1% IL)	11.41	17.49	25.77
0.1	14.51	14.62	23.56
0.5	12.75	11.88	22.27
1.0	11.82	11.52	16.36
1.5	10.99	11.39	14.84
2.0	9.79	10.29	13.06
4.0	7.96	8.88	10.74

Table 4.2: The peak OA signals for AuNCs at different concentrations for various backgrounds.

The average of 50 OA data points collected near the center of the cuvette (I_{target}) and the average of 50 OA data points collected from the Intralipid background ($I_{background}$) were used to determine the AuNCs contrast as a percentage change, according to

$$Contrast = \frac{\bar{I}_{target} - \bar{I}_{background}}{\bar{I}_{background}} \times 100 \tag{4.3}$$

Figure 4.5 shows AuNCs contrast versus background absorption for the three different AuNCs concentrations in the 7 background phantoms.

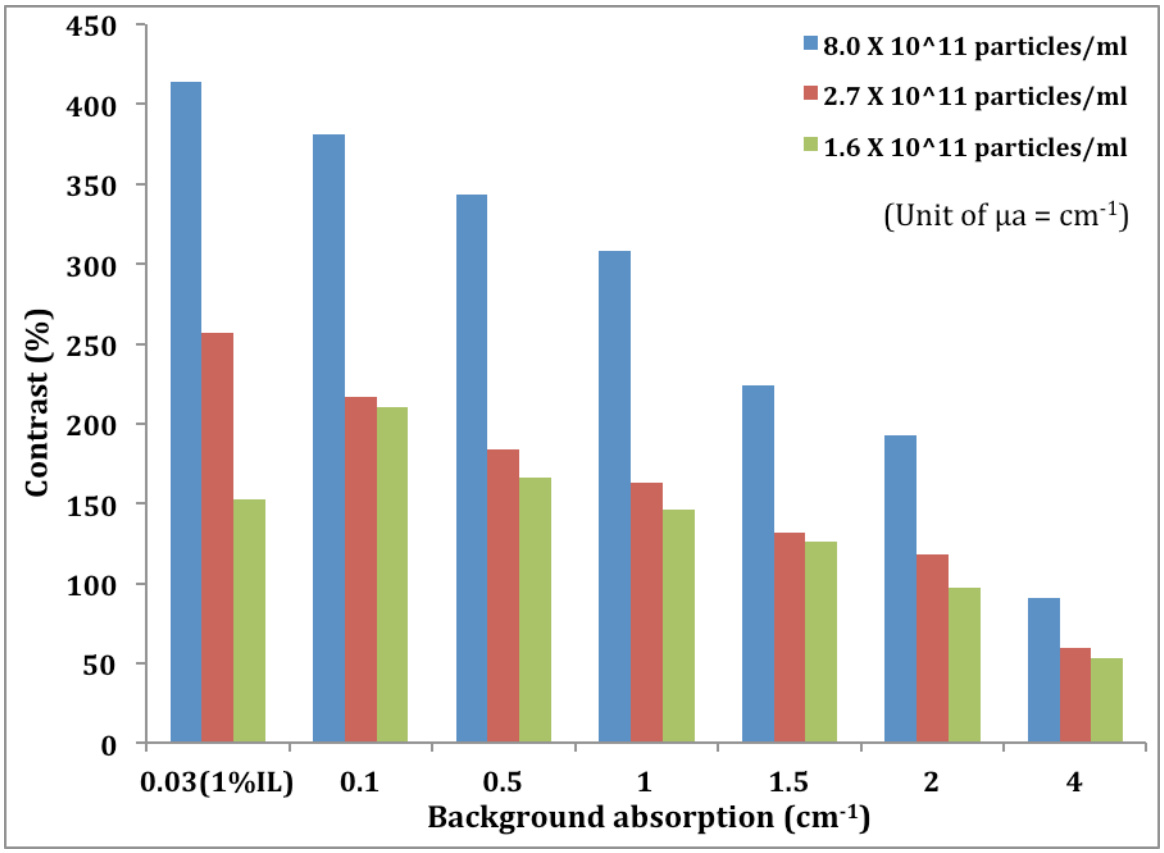

Figure 4.5: OA contrast values for three AuNCs concentrations in 7 different backgrounds absorptions.

Figure 4.5 demonstrates that contrast decreases with increasing background absorption. Two AuNCs target concentrations, 8.0×10^{11} particles/ml and 2.7×10^{11} particles/ml show a consistent decrease in contrast values with increasing background absorption. But for the lowest AuNCs target concentration, 1.6×10^{11} particles/ml, the contrast for Intralipid alone ($\mu_a = 0.03$ cm^{-1}) is lower then the contrast at $\mu_a = 0.1$ cm^{-1}. This is not expected and may be due to cuvette positioning or orientation error. For ease of viewing, the contrast values are shown in Table 4.3 for the different concentrations investigated. This data set also demonstrate that the same contrast can be achieved for different AuNCs concentrations in

varying backgrounds with different absorption properties. For e.g. the % change in contrast for 1.6×10^{11} particles/ml at μ_a= 0.5 cm^{-1} and for 2.7×10^{11} particles/ml at μ_a=1.0 cm^{-1} are similar at 166% and 163%, respectively. In addition, the % change in contrast for 1.6×10^{11} particles/ml at μ_a=2cm^{-1} and for 8.0×10^{11} particles/ml at μ_a= 4cm^{-1} are also approximately equivalent at, 97% and 91%, respectively. This property is important, as it demonstrates that different combinations of AuNCs concentration and background will achieve similar contrast.

Background Absorption (μ_a)(cm^{-1})	**AuNCs Concentrations (particles/ml)**		
	8.0×10^{11}	**2.7×10^{11}**	**1.6×10^{11}**
	% Change in contrast		
0.03(1% IL)	414	257	153
0.1	381	217	210
0.5	343	184	166
1	308	163	146
1.5	224	132	126
2	193	118	97
4	91	60	53

Table 4.3: Contrast of AuNCs at various concentrations for the 7 different background absorption phantoms.

As expected contrast increases with increasing AuNCs concentration and this is consistent for all the backgrounds investigated. As the trend of decreasing contrast with increasing background absorption looks linear, therefore, Linear fit has been done for data shown in Figure 4.5 to get a relationship between contrast and background, μ_a. slope of fit are shown in Figure 4.6.

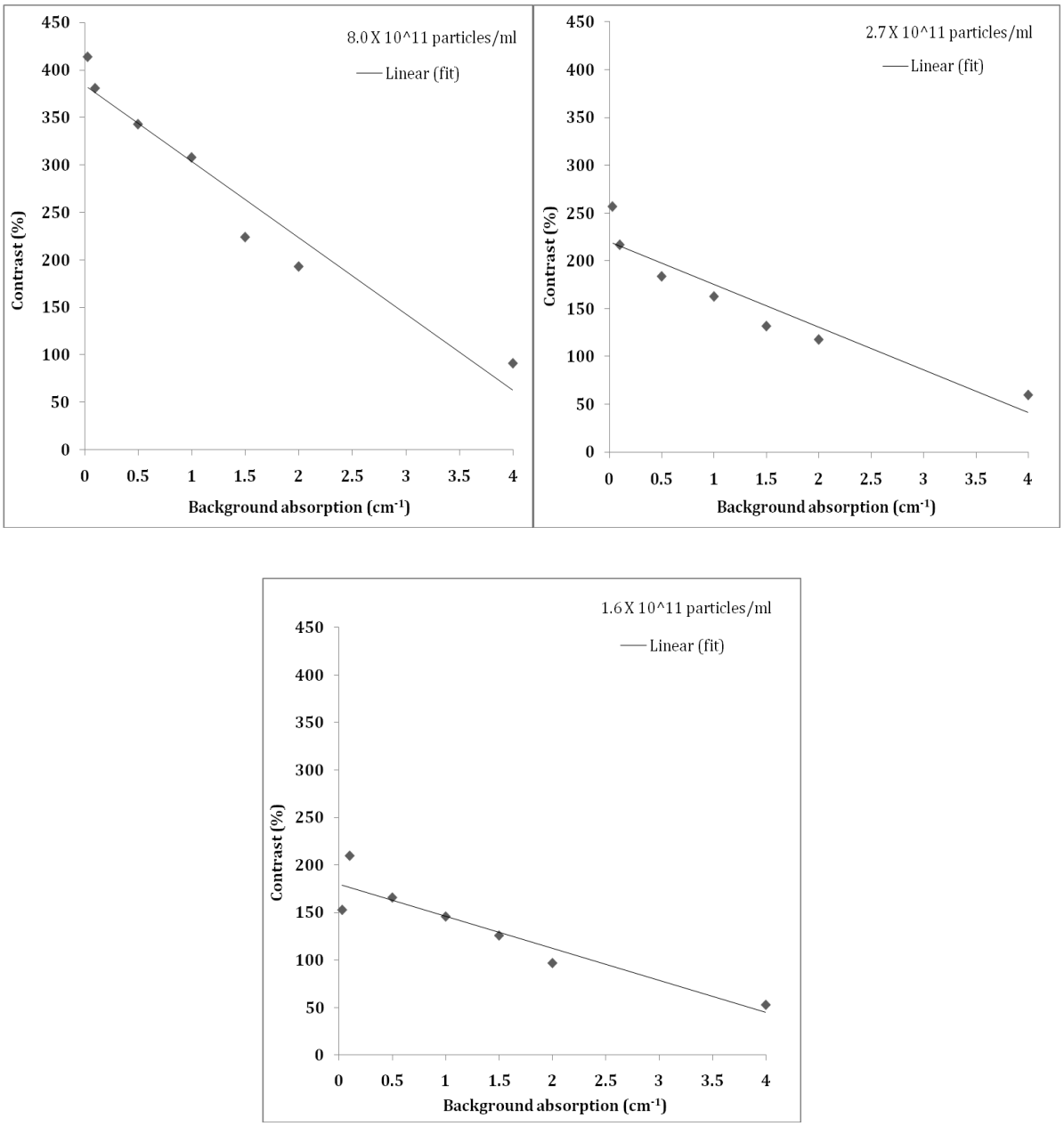

Figure 4.6: Linear fit of AuNCs contrast v/s background absorption for three AuNCs concentrations. a) 8.0 × 10^{11} particles/ml, b) 2.7 × 10^{11} particles/ml and c) 1.6 × 10^{11} particles/ml.

These fit yielded three equations for three AuNCs concentrations:

For 8.0×10^{11} particles/ml

$$y = -80.37x + 383.97 \quad (4.4)$$
$$R^2 = 0.94$$

For 2.7×10^{11} particles/ml

$$y = -44.54x + 219.6 \quad (4.5)$$
$$R^2 = 0.89$$

For 1.6×10^{11} particles/ml

$$y = -33.68x + 179.79 \quad (4.6)$$
$$R^2 = 0.86$$

In the above three equations, values of slope are negative, which indicates that values on Y-axis are decreasing with increasing X axis values. which is true for this data as contrast (Y-axis) is decreasing with increasing background absorption (X-axis). Higher R^2 values indicate that the model fits the data better.

4.5.2 Full width at half max (FWHM) predictions

In this study, we are using a 10 mm known target width. The FWHM approach is used to predict the width of the target using optoacoustic data for each of the AuNCs concentration and background combinations. Figure 4.7 shows the OA data for all AuNCs target and background combinations along with the corresponding FWHM values. In all cases the FWHM applied to the OA data overestimates the true cuvette dimension. For 1% IL background (no absorber) at highest AuNCs concentration (8.0 X 10^{11} particles/ml) the

FWHM is 12.5 mm. This indicates that a 10 mm target will appear 12.5 mm for this combination of background absorption and scattering, and AuNCs concentration. For 2.7×10^{11} particles/ml, the FWHM is 14 mm and for the lowest concentration, 1.6×10^{11} particles/ml at same background the FWHM is 18.2 mm. All three values are greater than the actual width (10 mm). This overestimation of target size was expected and typically increases with increasing imaging depth [[174].

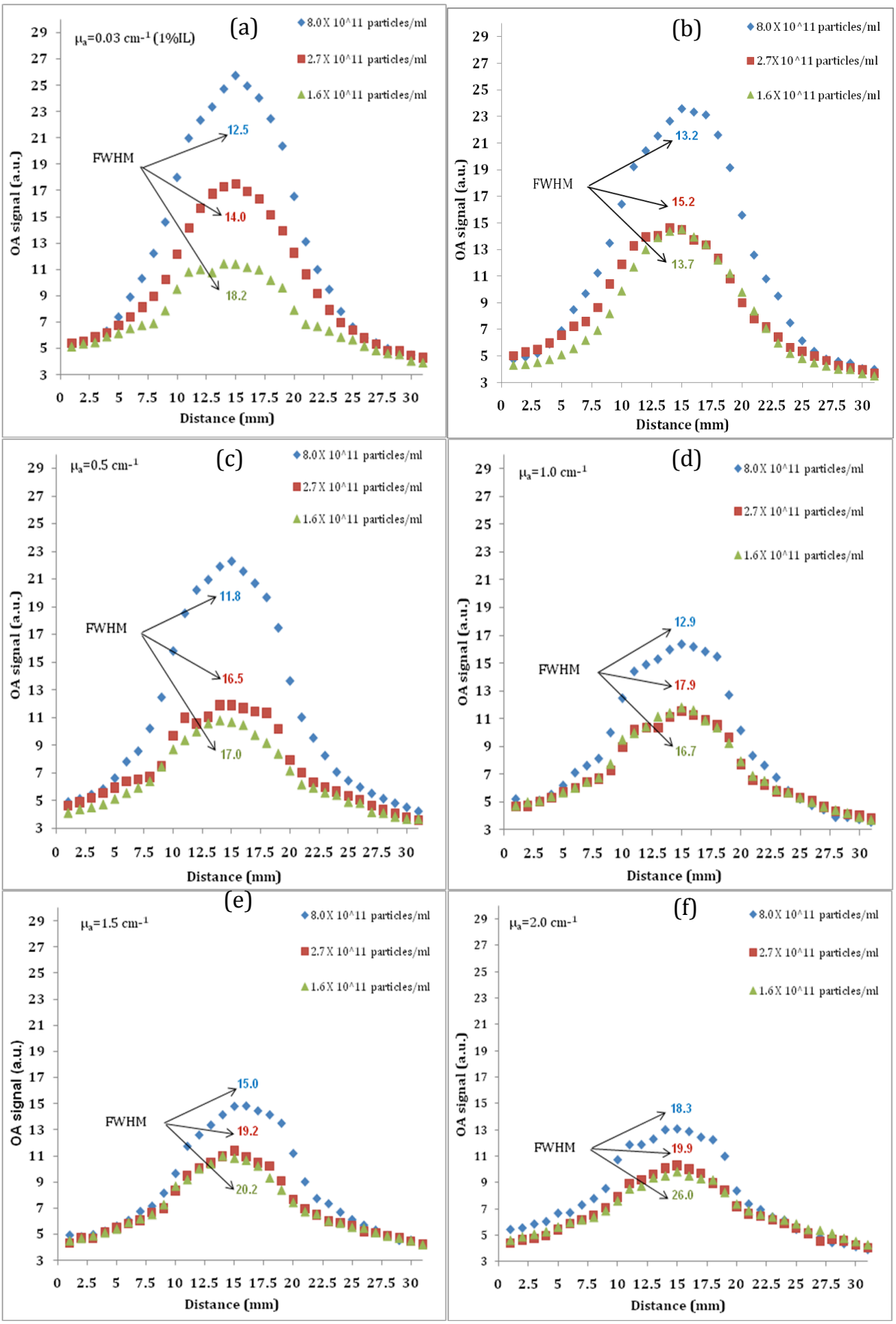
(a)
μa=0.03 cm-1 (1%IL)
8.0X 10^11 particles/ml
2.7X 10^11 particles/ml
1.6X 10^11 particles/ml
FWHM
12.5
14.0
18.2
OA signal (a.u.)
Distance (mm)
(b)
13.2
15.2
13.7
(c)
μa=0.5 cm-1
11.8
16.5
17.0
(d)
μa=1.0 cm-1
12.9
17.9
16.7
(e)
μa=1.5 cm-1
15.0
19.2
20.2
(f)
μa=2.0 cm-1
18.3
19.9
26.0

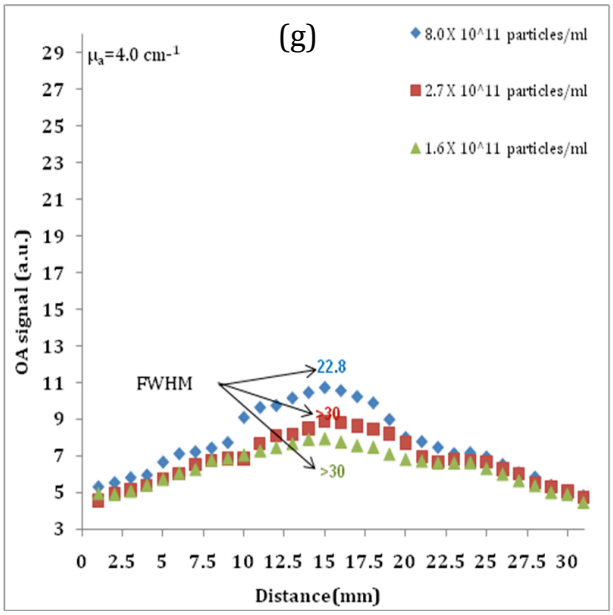

Figure 4.7: OA signal versus distance graph showing the calculated values of full width at half max (FWHM) for all three concentrations at different background absorptions. a) Intralipid alone, b) μ_a = 0.1cm^{-1}, c) μ_a = 0.5cm^{-1}, d) μ_a = 1cm^{-1}, e) μ_a = 1.5cm^{-1}, f) μ_a = 2cm^{-1}, g) μ_a = 4cm^{-1}.

The relationship between predicted cuvette dimension (FWHM), AuNCs concentration and background absorption is shown in figure 4.8. This data set indicates that predicted target dimensions increase with decreasing concentration and increasing background absorption. FWHM values for a background absorption coefficient of 4cm^{-1} were omitted as the value was >30 mm and the FWHM approach is not valid for highly absorbing backgrounds.

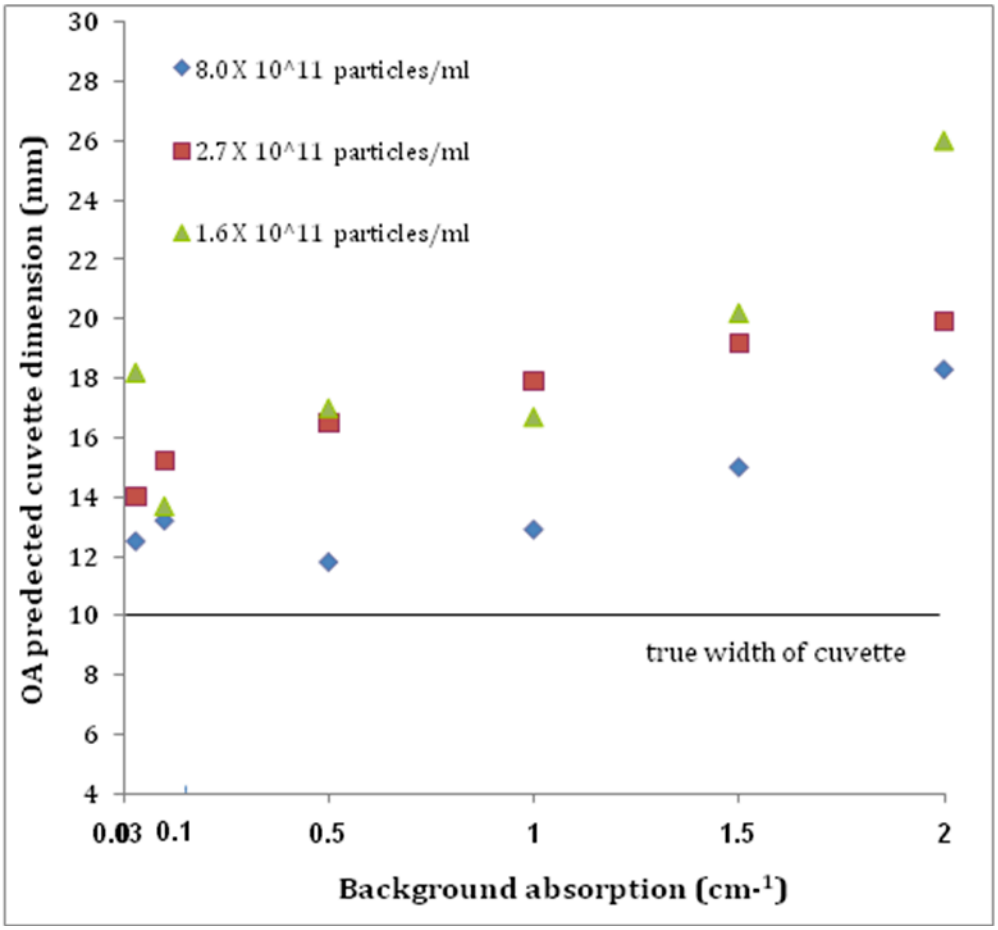

Figure 4.8: OA predicted cuvette dimension (FWHM) plotted against background medium for 3 AuNCs concentrations.

Figure 4.9 shows the optical absorption spectrum for the AuNCs (8.0×10^{11} particles/ml) before and after laser exposure. AuNCs exposed for 1% IL background at highest concentration, as a worse case scenario of the highest AuNCs concentration in the weakest background so as to maximize any potential damaging effect on the AuNCs. The optical absorption data indicates that there were no conformational changes in the AuNCs after the laser exposure at 0.016 J/cm^{-2} during experiments.

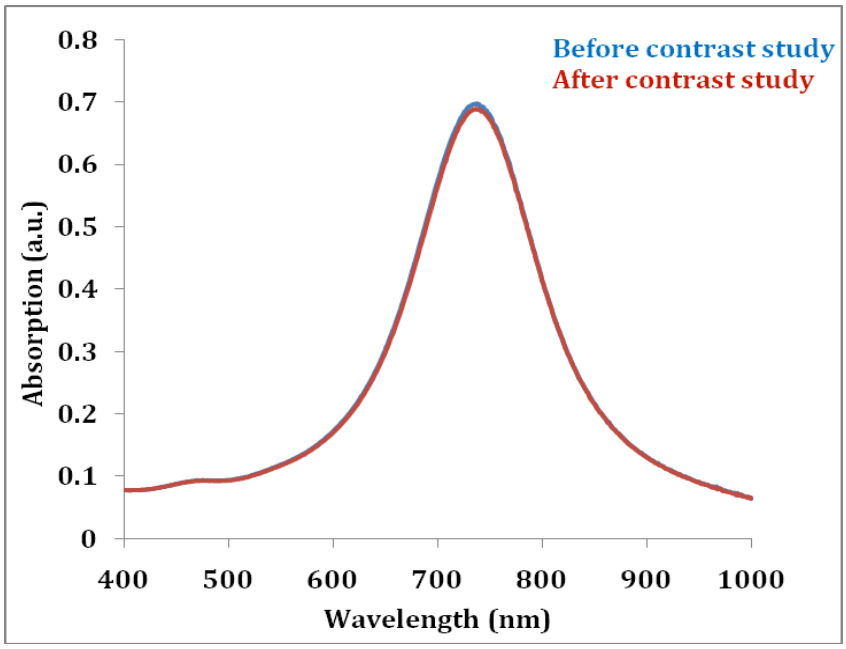

Figure 4.9: Optical absorption spectra for the AuNCs (8.0×10^{11} particles/ml) before and after OA illumination at 0.016 J/cm^{-2}.

Figure 4.10 shows the corresponding TEM image for the AuNCs sample after the exposure and demonstrates that there were no structural changes in AuNCs after the laser exposure. This confirms that the OA signal measured in the contrast study were influenced only by AuNCs concentration and background optical absorption.

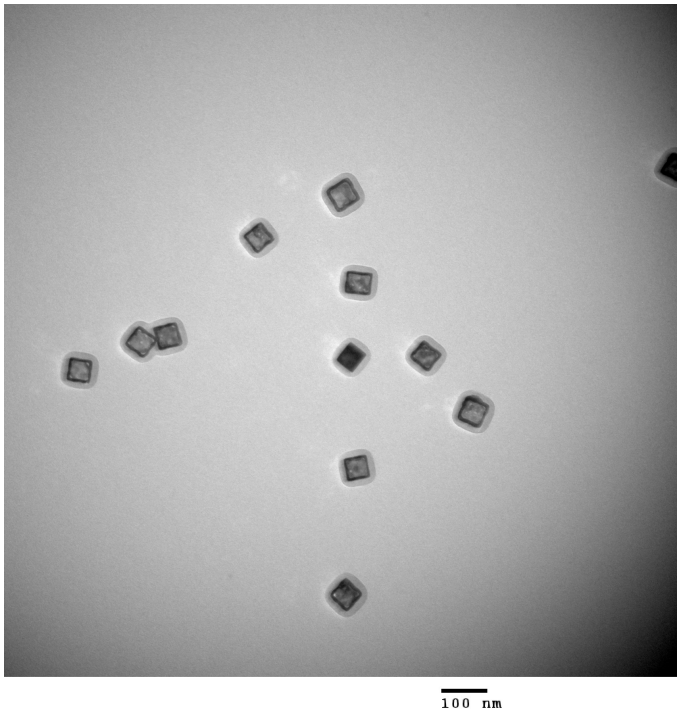

Figure 4.10: TEM image of AuNCs after laser exposure at 0.016 J/cm^{-2} (1% IL background and 8.0 × 10^{11} particles/ml AuNCs concentration).

Furthermore, the potential OA signals coming from the plexiglass box were also investigated. Figure 4.11 shows the OA signals for the plexiglass box and cuvette filled with water. OA signals coming from the box and cuvette are equivalent to the baseline signals, which confirms that the box and cuvette are not generating OA waves. The higher OA signals from 1mm to 20mm distance are due to a TGC artifact. OA signals from 1 to 20 mm distance should be at baseline as there is no target, but TGC amplification of OA signals in this area is observed. Signals/reverberations at the location between 37 to 40 mm may be coming from a spot of glue used to fix the box.

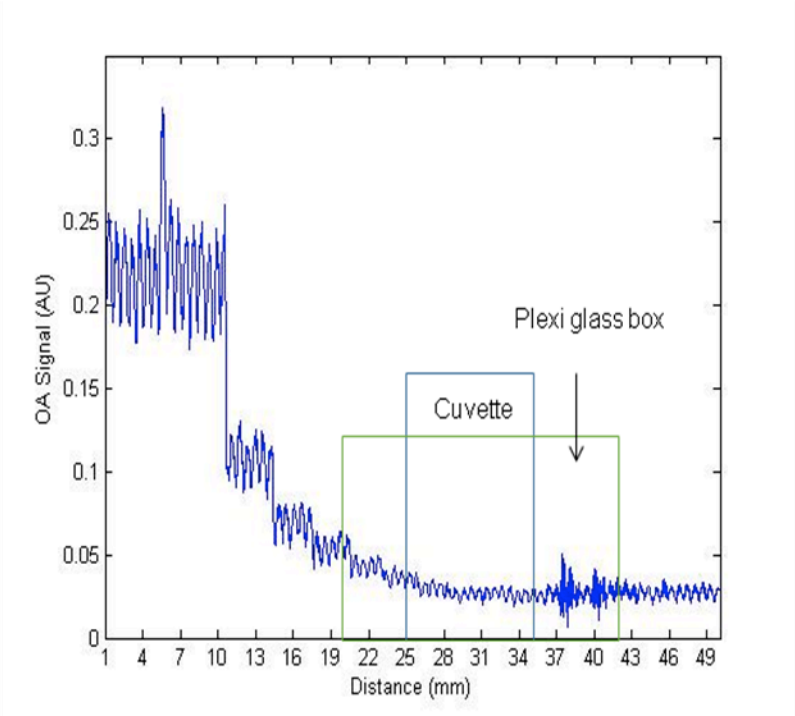

Figure 4.11: Acquired OA signal for the Plexi glass box and cuvette filled with water (i.e. blank). Appropriate location of box and cuvette are indicated in the plot.

4.6 Conclusions

This study investigated that OA signals from tested concentration of AuNCs are detectable up to background absorption coefficient of 4 cm^{-1} at 10 mJ laser energy and a surface fluence of 0.016 J/cm^2. Trend demonstrates that contrast is decreasing with increasing background absorption coefficient. No conformational changes in AuNCs after the laser exposures were observed for a maximum fluence of 0.016 J/cm^2.

As we know that 1% Intralipid based liquid phantom has constant absorption and scattering but in the real tissues these properties varies from sample to sample. Therefore, evaluations in tissue-based phantoms such as comprised of pork loin would be useful.

Chapter 5: Contrast study of AuNCs in *ex vivo* porcine muscle

5.1 Materials and methods

5.1.1 Tissue sample preparation

Pork loin was selected as a tissue phantom in this proof of principle study, as its optical properties were previously investigated by Grabtchak and Whelan[175]. Fresh pork loin was purchased at a local supermarket and left on the lab bench until it reached room temperature. Four pork loin samples were prepared. Two samples were approximately 5 mm (thickness) × 70 mm (length) × 25 mm (width) and two other samples were 10 mm (thickness) × 70 mm (length) × 25 mm (width). Figure 5.1 shows the pork and its dimensions.

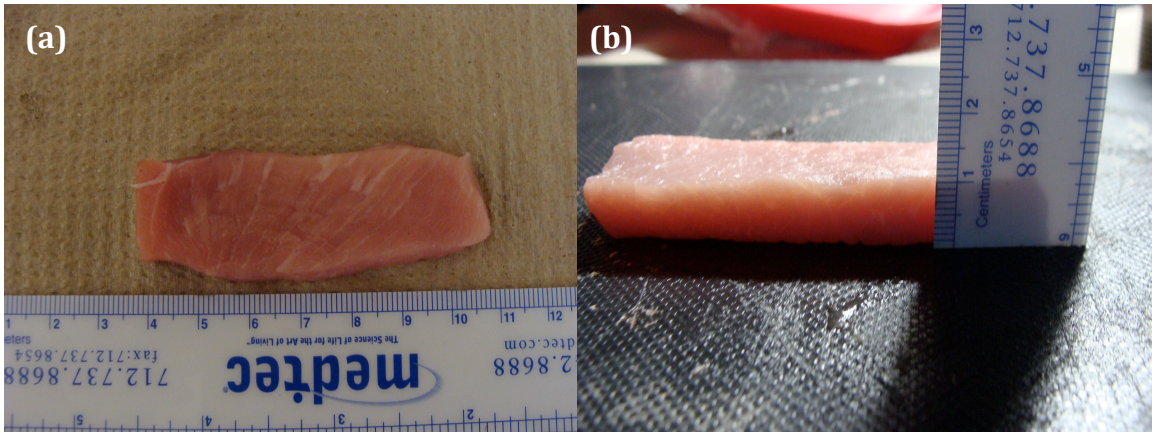

Figure 5.1: Representative pork loin sample a) length and width b) thickness for OA investigation.

All four samples tissues were covered with plastic wrap to avoid direct exposure with water in the water bath. Figure 5.2 shows a cuvette (5 mm path length) with AuNCs (2.7×10^{11} particles/ml) wrapped with the pork tissue. Wrapping was achieved by placing the cuvette at the center of the tissue sample and then drawing both the ends of tissue around the cuvette and fixing the ends with plastic tape on the back side of the cuvette.

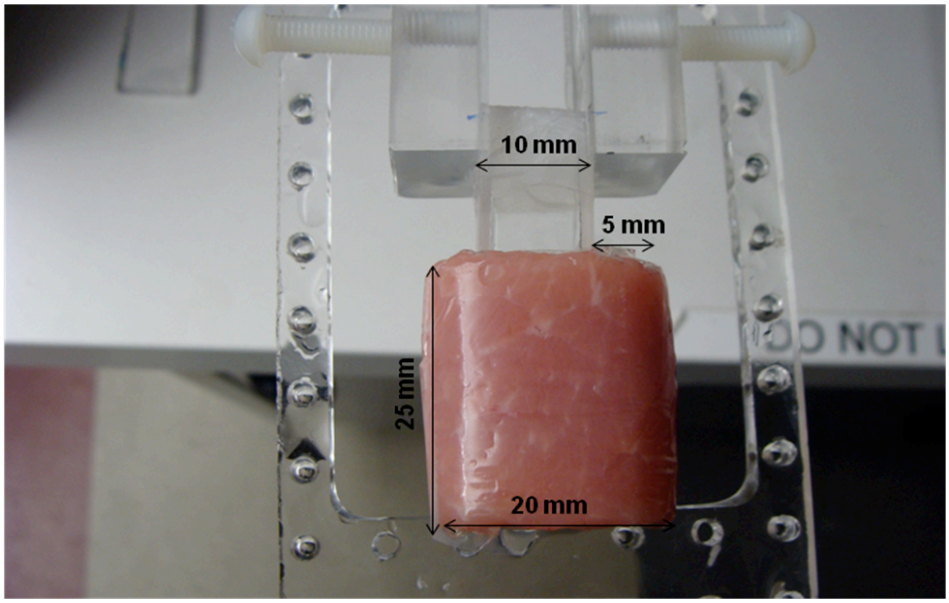

Figure 5.2: Pork loin wrapped sample around the cuvette filled with AuNCs and mounted to a cuvette holder.

The tissue wrapped cuvette was mounted to a holder on a translation stage, and positioned (front wall) 25 mm from the transducer, as shown in figure 5.3. The energy output from the fiber bundle was measured and the water bath was at room temperature (23 ^{0}C). The cuvette was sealed with parafilm to avoid the entry of water.

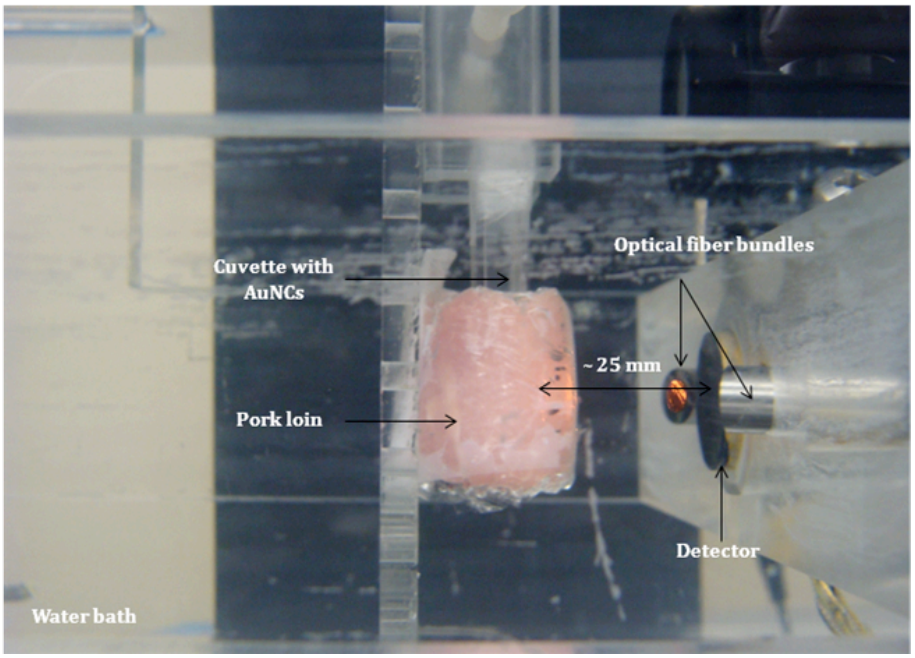

Figure 5.3: Cuvette wrapped with pork loin, mounted on the translation stage, and showing distance between cuvette and transducer (25 mm).

5.2 Optoacoustic detection

A 9.2 mJ laser energy (0.014 J/cm^2) at 775 nm and 0.1 mm step size was used for all experiments. An AuNCs concentration of 2.7 × 10^{11} particles/ml was used for all experiments, e.g. the intermediate concentration used in the contrast study using an Intralipid based background. After mounting the wrapped cuvette on the translation the path length was selected. Four experiments were carried, two with a 5 mm thick pork loin tissue sample and two with a 10 mm thick pork loin tissue sample.

5.3 Results and discussion

5.3.1 Effect of phantom thickness on OA signal generation

Figure 5.4 shows the OA signals generated from the AuNCs (2.7×10^{11} particles/ml) in the cuvette surrounded by a 5 mm pork loin (repeated with a different tissue sample). Figure 5.5a and 5.5b) show the OA signals generated with 10 mm thick pork loin surrounding the AuNCs filled cuvette.

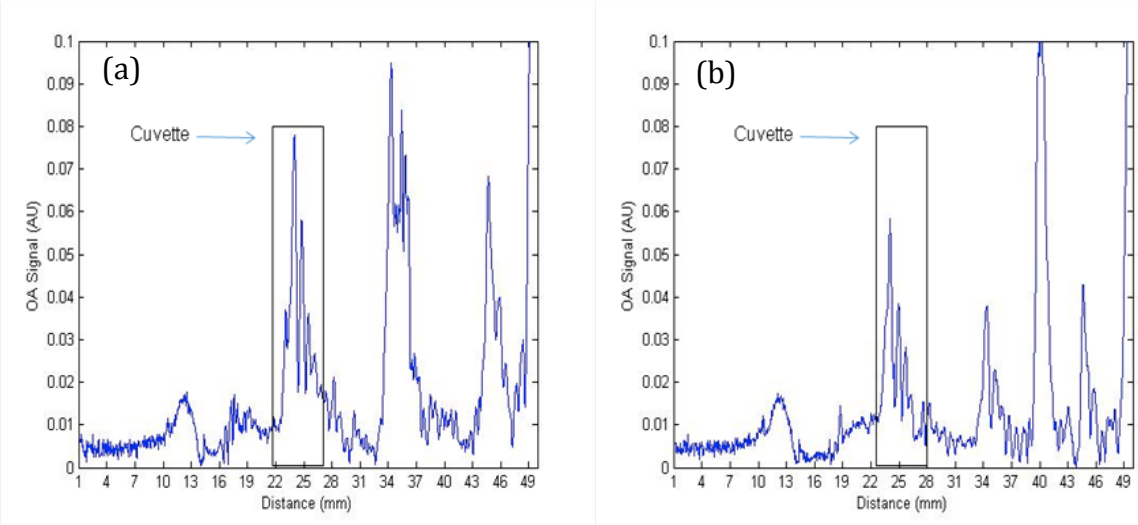

Figure 5.4: OA signals v/s distance from the transducer for AuNCs exposed at 0.014 J/cm^2 through 5 mm of pork loin, (a) Trial 1 and (b) Trial 2. The appropriate position of the cuvette is shown on the plot.

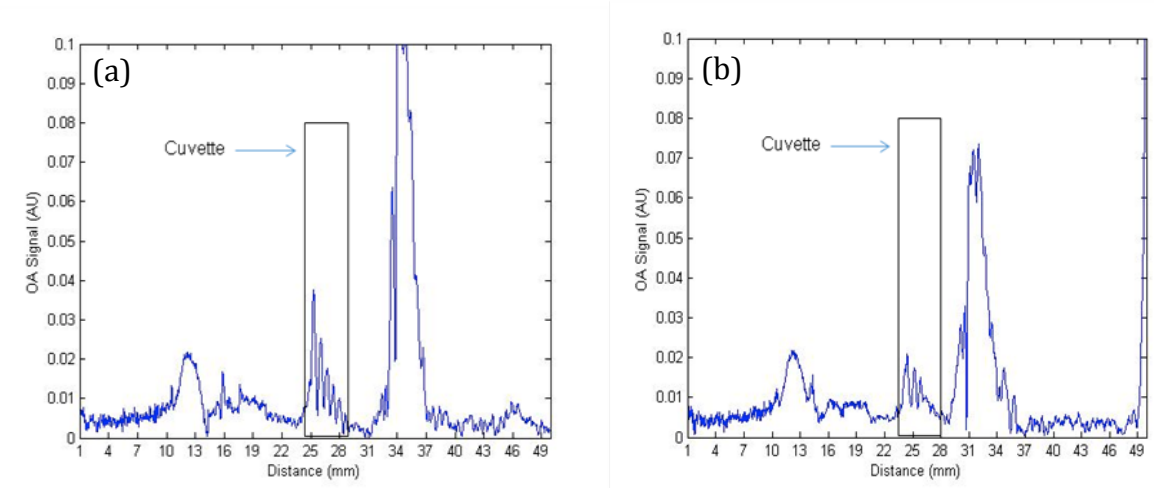

Figure 5.5: OA signals v/s distance from the transducer for AuNCs exposed at 0.014 J/cm^2 through 10 mm of pork loin, (a) Trial 1 and (b) Trial 2. The appropriate position of the cuvette is shown on the plot.

The peak OA signal at the location of the cuvette for the 5 mm of pork, Trial 1 and Trial 2 is 0.08 and 0.06, respectively. The peak OA signal for the 10 mm of pork in Trial 1 and Trial 2 is 0.04 and 0.02, respectively. A broad peak between 10-13 mm from the transducer is present in all contrast study plots including for the Intralipid background (Chapter 4). The exact reason for this broad peak is not known. Stronger OA peaks (amplitude higher than that from the AuNCs) are detected at delay times that correspond to being in the water bath behind the cuvette, e.g. 31-37 mm from the transducer. To try to better understand the large signals observed from this region, OA data was acquired for a water filled cuvette (Figure 5.6). As observed in Figure 5.6, OA peak signals are still present when there are no AuNCs. No confirmed reason is known for these peaks, but the possible explanation is that, these might be the reverberations of the signals coming from the tissue sample.

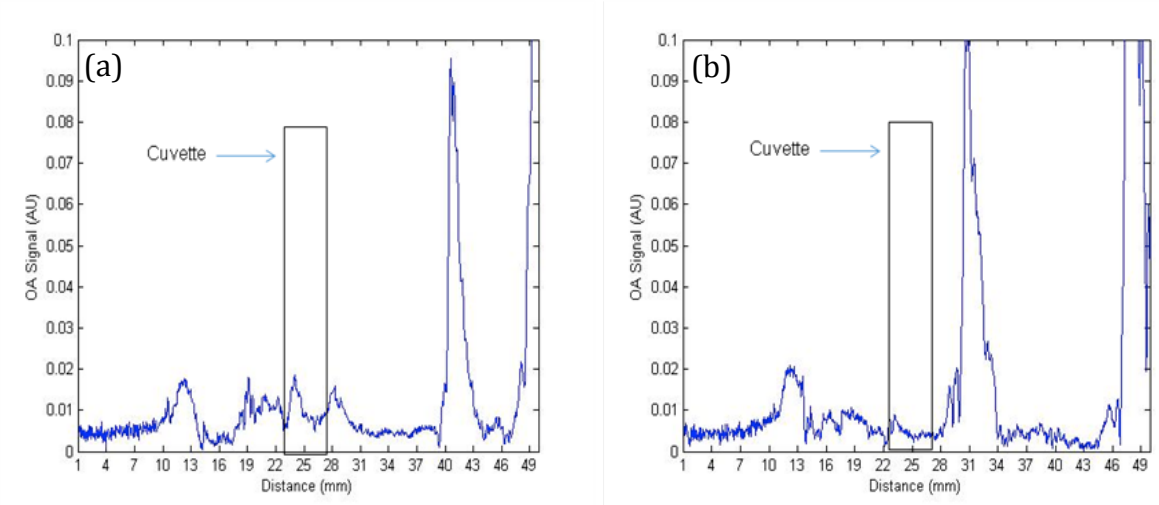

Figure 5.6: OA signals v/s distance from the transducer plot of water (blank run) exposed at 0.014 J/cm^2 using pork loin of 5 mm thickness (a) and 10 mm thickness (b).

Intralipid OA signals of AuNCs in 1% Intralipid background (5 mm physical depth) chapter4, section-1 are average 91% (based on average of Trial 1 and 2 of 5 mm thickness) higher than the OA signal of AuNCs in 5 mm thick pork loin and 137% (based on average of Trial 1 and 2 of 10 mm thickness) higher than the 10 mm thick pork loin background. A tissue of 5 mm thickness shows 46% higher contrast in comparison to 10 mm thick pork loin tissue. Contrast values are given in table 5.1 (calculated by using equation 4.3).

AuNCs concentration = 2.7×10^{11} particles/ml	
Background medium	**Contrast**
1% Intralipid (5mm)	257%
Pork loin, 5 mm A	163%
Pork loin, 5 mm B	156%
Pork loin, 10 mm A	145%
Pork loin, 10 mm B	82%

Table 5.1: Calculated contrast values of AuNCs for different backgrounds.

Peak OA signals of AuNCs are higher in pork loin background compared to the 1% IL phantom background. The effective attenuation coefficient, $\mu_{eff,}$ of 1% IL and pork loin are similar, 1cm^{-1} at 775 nm[173][175]. Hence, we may expect that the peak OA signals from the AuNCs from both background media (5 mm physical depth) should be equal. Even though the, μ_{eff} is equivalent, pork loin has a lower reduced scattering coefficient (μ_s' = 3 cm^{-1}) and higher absorption coefficient (μ_a = 0.1 cm^{-1}) compared to 1% IL (μ_s' = 10 cm^{-1}, μ_a = 0.03 cm^{-1}) at 775 nm. One possible explanation for higher OA signal amplitude from AuNCs in the pork loin background can be its lower scattering coefficient (1/3 lower) compared to 1% IL, which allows more light to reach the AuNCs. The optical absorption in pork loin is also lower.

5.4 Conclusion

The results from this study demonstrate that the OA signals from AuNCs (2.7×10^{11} particles/ml) are detectable up to 10 mm depth in pork loin utilizing a 9.2 mJ laser pulse energy (0.014 J/cm^2) at 775 nm. The OA signals from AuNCs in 5 mm pork loin are approximately double in comparison to AuNCs in 10 mm pork loin phantom. This was expected because 5 mm extra thickness in 10 mm tissue restricted more light from reaching the target.

Chapter 6: Conclusion and future work

6.1 Conclusions

Three objectives had been set for this project: 1) synthesize gold nanocages using silver nanocubes as the templates via galvanic replacement reactions, 2) determine the stability of gold nanocages against pulsed (6ns) laser light at different energies and 3) determine the contrast properties of gold nanocages (different concentrations) using 1% Intralipid and pork loin as background medium.

The polyol method was used to synthesize silver nanocubes to further use them as the templates for AuNCs synthesis. The reaction was highly temperature sensitive such that a fluctuation of ±5 ^{0}C adversely affected the synthesis reaction. The process of adding reactants to the reaction solution also had an effect on the nucleation process of silver nanocube synthesis. It was learned that the equipment used in the process, specifically glassware, should be of a specific brand and catalogue number. For example, the round bottom flask should be from Ace glass Inc. (Cat. No. 4120-21) and disposable vials should be from VWR (cat. No. 66011-143)[146]. Similar rules apply to the chemicals used in reaction, for example; ethylene glycol should be from J.T. Baker (cat. No. 9300). The use of other brands can cause the synthesis to fail. Hence, it was difficult to optimise the reaction parameters in such a short time. After 38 individual batches, we were able to synthesize silver nanocubes with only 20-30% purity, which was not sufficient for use as templates for AuNCs synthesis. Therefore, for the thesis work, AuNCs were acquired from Dr. Younan Xia (Georgia Tech).

Results from all three analysis methods (optoacoustic signal detection, TEM imaging and optical absorption measurements) used to measure the stability of AuNCs demonstrate that on direct illumination (with no background medium) at 5 mJ and 10 mJ laser energy at 775 nm, AuNCs are not geometrically stable. For both energies investigated, conformational changes were observed. Results from this thesis confirms that with increasing energy and exposure time, gold nanocages tend to turn spherical in shape and many other structures between cube and sphere are also formed which leads to a change in surface plasmon resonance. This study also demonstrates that melting of AuNCs can occur at 5 mJ but fragmentation requires a higher energy, 10 mJ. Usually a contrast study is completed with the optically turbid background media (such as phantoms) where most of the light is absorbed or scattered before reaching the target and hence may not destabilize the structure. However, this stability study with no background provides important information for in-vitro studies using gold nanocages. For example to study the effects of contrast agents in comparatively controlled environment, cancerous cells could be extracted from body into a petri dish and loaded with nanoparticles to study the contrast properties. Recently, Zhang et.al[176] labelled AuNCs with human mesenchymal stem cells and carried phantom experiment by imaging suspensions of AuNCs at different concentrations sealed in glass capillaries with a optoacoustic system (deep reflection-mode optoacoustic imaging system utilized a tunable Ti:Sapphire laser pumped by a Q-switched Nd:YAG laser for optoacoustic excitation at a wavelength of 800 nm (pulse width: 5 ns, pulse repetition rate: 10 Hz). Though, Zhang used AuNCs to stem cells tracking but for this kind of *in vitro* experiments, stability of AuNCs should be known.

The OA contrast for AuNCs (8.0×10^{11} particles/ml, 2.7×10^{11} particles/ml and 1.6×10^{11} particles/ml) in 1% Intralipid results confirmed that OA signals from AuNCs were

detectable in the highest absorbing background ($4cm^{-1}$) used in this study. This demonstrates the utility of AuNCs as contrast agents in optoacoustic imaging. Full width at half max calculations provides an estimate of the actual size of target using OA data. Optical absorption measurement indicates no conformational changes in AuNCs, after all the pulsed laser illuminations for contrast study (for all the absorption coefficients). TEM imaging confirmed no damage.

Results from OA contrast study in *ex vivo* muscle demonstrated that AuNCs also have an effective contrast in soft tissue through up to 10 mm. The OA signals from AuNCs in 5 mm pork loin are approximately double in comparison to AuNCs in 10 mm pork loin. Gold nanocages demonstrate a higher contrast (97.5% higher) in 1% Intralipid (no absorber) compared to using pork loin for the same 5 mm thickness (comparison based on AuNCs concentration 2.7×10^{11} particles/ml, because this is the only concentration tested in muscle experiment). AuNCs contrast in 1% Intralipid decreases with increased optical absorption ($\mu_a = 4\ cm^{-1}$) of the background medium. And at highest μ_a, the value of contrast (60%) is lower than the contrast (159.4%) of AuNCs in 5 mm thick pork loin (for AuNCs concentration 2.7×10^{11} particles/ml). The results from this study confirm that AuNCs can be used as contrast agent in the imaging of soft tissues effectively.

On the basis of thesis results, we conclude that AuNCs are relevant contrast agents for optoacoustic imaging.

6.2 Future work

Further investigations are required to study contrast properties of AuNCs and their potential use for specific medical applications as contrast agents. The work described in this dissertation represents a significant step toward better understanding of AuNCs contrast agents for optoacoustic that could provide for deeper tissue imaging with more sensitivity and specificity.

The contrast study of AuNCs required more research using the different concentrations of gold nanocages and at lower fluence values (less than 10 mJ/cm^2, maximum ANSI limit) to find a threshold limit. This will determine what minimum concentration of AuNCs and fluence are required for tissue imaging at clinically relevant depths. The next challenge is to investigate the contrast of AuNCs in *in-vivo* experiments. But *in vivo* imaging is more complex when considering additional factors such as the effect of blood flow, blood water concentration and optical heterogeneity and their effects on OA image contrast. Zhang et.al.[177] used C57/BL6 mice for subcutaneous OA imaging experiments. For tumor imaging experiments, human breast cancer cells, BT474 (ATCC) were implanted on the lower abdominal wall of Nu/Nu mice and allowed to grow to ~1.0 cm in size. They performed, *in vivo* optoacoustic imaging experiments before and after the injection of 20 and 50 nm gold nanoparticles into the subcutaneous abdominal wall of the mice and both 20 nm particles and 50 nm particles were imaged *in vivo* with excellent contrast[177].

There is also the future opportunity to study functionalized gold nanocages. In this way they can be used as contrast agents and as well as effective therapeutic agents. Chen et.al.[178] conjugated 45nm AuNCs with monoclonal antibodies (anti-HER2) to target epidermal growth factor receptors (EGFR) that are overexpressed on the surface of breast

cancer cells (SK-BR-3). Their preliminary photothermal results show that the nanocages strongly absorb light in the NIR region with a minimum intensity threshold of 1.5 W/cm^2 to induce thermal destruction to the cancer cells. In the intensity range of 1.5-4.7 W/cm^2, the circular area of damaged cells increased linearly with the irradiation power density. They concluded that, this new class of bioconjugated gold nanostructures, immuno gold nanocages, could potentially serve as an effective photothermal therapeutic agent for cancer treatment[178]. Khan et.al[179] synthesized AuNCs and conjugated with single walled CNT. This AuNCs-SWCNT hybrid was further conjugated with A9 RNA aptamer to target cancer cells. Khan used 1-2 W/cm^2 of 1064 nm NIR light for 10 min and concluded that AuNCs-SWCNT-A9 RNA aptamer hybrid can potentially serve as an effective photothermal therapeutic agent for cancer treatment.

The Seno system in our lab record data every second (after 10 laser pulses). Yet the data supports that damage to AuNCs structure can occur after the first laser pulse depending on the laser energy. Therefore an upgrade to the Seno system is needed to be able to acquire OA data after individual pulses.

In this research work we varied the optical depth by adding an absorber to a constant scattering medium, as it was not possible to vary the physical depth in our OA protocol. This provided a direct relationship between target depth and contrast. A specially designed box for phantom materials is required to measure contrast of AuNCs by physically varying the depth of target. That box should have the capability to vary the distance of the gold target without removing it from the translation stage and it should be designed in a way that it would be sealed such that water would not enter into box. Another challenge was the instability of Seno system laser energy output. Output laser energy changed day by day,

which required ongoing measurement and correction. Planned upgrades to the Seno OA system will provide for enhanced research on AuNCs as OA contrast agent.

References

[1] “Fundamentals of Computerized Tomography - Image Reconstruction from Projections.” http://www.springer.com/computer/image+processing/book/978-185233-617-2.

[2] G. Katti, S. A. Ara, and A. Shireen, “Magnetic Resonance Imaging (MRI) – A Review,” vol. 3, no. 1, pp. 65–70, 2011.

[3] S. Bauer, R. Wiest, L.-P. Nolte, and M. Reyes, “A survey of MRI-based medical image analysis for brain tumor studies.,” *Phys. Med. Biol.*, vol. 58, no. 13, pp. R97–129, 2013.

[4] A. W. K. Leung, W. C. W. Chu, W. W. M. Lam, V. Lee, and C. K. Li, “Magnetic resonance imaging assessment of cardiac and liver iron load in transfusion dependent patients.,” *Pediatr. Blood Cancer*, vol. 53, no. 6, pp. 1054–9, 2009.

[5] E. A Walker, M. E. Fenton, J. S. Salesky, and M. D. Murphey, “Magnetic resonance imaging of benign soft tissue neoplasms in adults.,” *Radiol. Clin. North Am.*, vol. 49, no. 6, pp. 1197–217, vi, 2011.

[6] M. J. Siegel, “MRI of Bone Marrow.”

[7] “Magnetic Resonance Imaging(MRI).” http://www.healthcentral.com/encyclopedia/408/218.html.

[8] K. K. Shung, “Diagnostic Ultrasound": Past , Present , and Future,” vol. 31, no. 6, pp. 371–374, 2011.

[9] S. Hughes, “Medical ultrasound imaging,” *Phys. Educ.*, vol. 36, no. 6, pp. 468–475, 2001.

[10] Shelly Medical Imaging Technologies, “Shelly Medical Imaging Technologies,” pp. 92–99, 2006.

[11] H. Chiou, Y. Chou, S. Chiou, and H. Wang, “High-resolution Ultrasonography in Superficial Soft Tissue Tumors,” vol. 15, no. 3, pp. 152–174, 2007.

[12] H. Sillesen and V. Fuster, “Predicting coronary heart disease: from Framingham Risk Score to ultrasound bioimaging.,” *Mt. Sinai J. Med.*, vol. 79, no. 6, pp. 654–63, . .

[13] A. F. Fercher, W. Drexler, C. K. Hitzenberger, and T. Lasser, “Optical coherence tomography — principles and,” vol. 66, pp. 239–303, 2003.

[14] “Diffuse Optical Tomography and Imaging PicoQuant.” http://www.picoquant.com/applications/category/life-science/diffuse-optical-tomography-and-imaging.

[15] R. Choe, “Diffuse optical tomography and spectroscopy of breast cancer and fetal brain,” *Dissertations available from ProQuest*. pp. 1 – 226, 2005.

[16] “Diffuse Optical Tomography and Imaging PicoQuant.” https://www.picoquant.com/applications/category/life-science/diffuse-optical-tomography-and-imaging.

[17] “Optical tomography of breast cancer—monitoring response to primary medical therapy Michael Douek - Academia.edu.” http://www.academia.edu/3390573/Optical_tomography_of_breast_cancer-monitoring_response_to_primary_medical_therapy.

[18] S. J. Madsen, Ed., *Optical Methods and Instrumentation in Brain Imaging and Therapy*. New York, NY: Springer New York, 2013.

[19] M. E. Brezinski, G. J. Tearney, B. E. Bouma, J. A. Izatt, M. R. Hee, E. A. Swanson, J. F. Southern, and J. G. Fujimoto, “Optical Coherence Tomography for Optical Biopsy": Properties and Demonstration of Vascular Pathology,” *Circulation*, vol. 93, no. 6, pp. 1206–1213, 1996.

[20] C. Blatter, J. Weingast, A. Alex, B. Grajciar, W. Wieser, W. Drexler, R. Huber, and R. a Leitgeb, “In situ structural and microangiographic assessment of human skin lesions with high-speed OCT.,” *Biomed. Opt. Express*, vol. 3, no. 10, pp. 2636–46, 2012.

[21] J. G. Fujimoto, C. Pitris, S. A. Boppart, and M. E. Brezinski, “Optical Coherence Tomography": An Emerging Technology for Biomedical Imaging and Optical Biopsy 1,” vol. 2, pp. 9–25, 2000.

[22] G. J. Tearney, M. E. Brezinski, B. E. Bouma, S. A. Boppart, C. Pitris, J. F. Southern, and J. G. Fujimoto, “*In vivo* endoscopic optical biopsy with optical coherence tomography,” *Science*, vol. 276, no. 5321, pp. 2037–9, 1997.

[23] S. A. Boppart, “surface modified protien microparticles,” vol. 1, no. 19, 2004.

[24] B. Bouma, G. J. Tearney, S. a Boppart, M. R. Hee, M. E. Brezinski, and J. G. Fujimoto, “High-resolution optical coherence tomographic imaging using a mode-locked Ti:Al(2)O(3) laser source.,” *Opt. Lett.*, vol. 20, no. 13, pp. 1486–8, 1995.

[25] B. E. Bouma, G. J. Tearney, I. P. Bilinsky, B. Golubovic, and J. G. Fujimoto, “Self-phase-modulated Kerr-lens mode-locked Cr:forsterite laser source for optical coherence tomography,” *Opt. Lett.*, vol. 21, no. 22, p. 1839, 1996.

[26] W. Drexler, U. Morgner, F. X. Kärtner, C. Pitris, S. A. Boppart, X. D. Li, E. P. Ippen, and J. G. Fujimoto, “*In vivo* ultrahigh-resolution optical coherence tomography,” *Opt. Lett.*, vol. 24, no. 17, p. 1221, 1999.

[27] S. A. Boppart, B. E. Bouma, C. Pitris, J. F. Southern, M. E. Brezinski, and J. G. Fujimoto, "*In vivo* cellular optical coherence tomography imaging.," *Nat. Med.*, vol. 4, no. 7, pp. 861–5, 1998.

[28] G. J. Tearney, S. A. Boppart, B. E. Bouma, M. E. Brezinski, N. J. Weissman, J. F. Southern, and J. G. Fujimoto, "Scanning single-mode fiber optic catheter-endoscope for optical coherence tomography: erratum," *Opt. Lett.*, vol. 21, no. 12, p. 912, 1996.

[29] S. A. Boppart, B. E. Bouma, C. Pitris, G. J. Tearney, J. G. Fujimoto, and M. E. Brezinski, "Forward-imaging instruments for optical coherence tomography," *Opt. Lett.*, vol. 22, no. 21, p. 1618, 1997.

[30] "Canada Diagnostic Centres." http://www.canadadiagnostic.com/content/about/fee-schedule.php.

[31] "Alexander Graham BELL, Ph.D., 'On the Production and Reproduction of Sound by Light' 2." http://histv2.free.fr/bell/bell2.htm.

[32] V. Zéninari, B. Parvitte, D. Courtois, V. A. Kapitanov, and Y. N. Ponomarev, "Methane detection on the sub-ppm level with a near-infrared diode laser photoacoustic sensor," *Infrared Phys. Technol.*, vol. 44, no. 4, pp. 253–261, 2003.

[33] V. A. Kapitanov, Y. N. Ponomarev, K. Song, H. K. Cha, and J. Lee, "Resonance photoacoustic spectroscopy and gas analysis of gaseous flow at reduced pressure," *Appl. Phys. B Lasers Opt.*, vol. 73, no. 7, pp. 745–750, 2001.

[34] K. Hatanaka, Y. Tsuboi, H. Fukumura, and H. Masuhara, "Nanosecond and Femtosecond Laser Photochemistry and Ablation Dynamics of Neat Liquid Benzenes," *J. Phys. Chem. B*, vol. 106, no. 12, pp. 3049–3060, 2002.

[35] S. M. Park, M. I. Khan, H. Z. Cheng, and G. J. Diebold, “Photoacoustic effect in strongly absorbing fluids,” *Ultrasonics*, vol. 29, pp. 63–67, 1991.

[36] F. Blackmon and L. Antonelli, “Experimental demonstration of multiple pulse nonlinear optoacoustic signal generation and control,” *Appl. Opt.*, vol. 44, no. 1, p. 103, 2005.

[37] M. J. Colles, N. R. Geddes, and E. Mehdizadeh, “The optoacoustic effect,” *Contemp. Phys.*, vol. 20, no. 1, pp. 11–36, 1979.

[38] T. Mitcham, K. Homan, W. Frey, Y.-S. Chen, S. Emelianov, J. Hazle, and R. Bouchard, “Modulation of photoacoustic signal generation from metallic surfaces.,” *J. Biomed. Opt.*, vol. 18, no. 5, p. 56008, 2013.

[39] G. Paltauf and P. E. Dyer, “Photomechanical processes and effects in ablation.,” *Chem. Rev.*, vol. 103, no. 2, pp. 487–518, 2003.

[40] “Evaluation of optoacoustic frequency analysis sensitivity to discriminate healthy and neoplastic tissues and to monitor treatment-induced physiological changes,” Michelle patterson.

[41] “The Application of Compressed Sensing for Photo-Acoustic Tomography: http://eds.a.ebscohost.com.proxy.library.upei.ca

[42] A. A. Karabutov, E. V Savateeva, and A. A. Oraevsky, “Optoacoustic Tomography": New Modality of Laser Diagnostic Systems,” vol. 13, no. 5, pp. 711–723, 2003.

[43] *Photoacoustic Imaging and Spectroscopy*. CRC Press, 2009.

[44] A. Manuscript, “NIH Public Access,” vol. 54, no. 19, pp. 1–52, 2010.

[45] *Biomedical Photonics Handbook*. CRC Press, 2003.

[46] Tissue optics-chapter 2, shodhganga.inflibnet.ac.in/bitstream/10603/6520/.../07_chapter%202.pdf.

[47] L. V. Wang and H. Wu, *Biomedical Optics: Principles and Imaging*. John Wiley & Sons, 2007.

[48] M. Xu and L. V. Wang, "Photoacoustic imaging in biomedicine," *Rev. Sci. Instrum.*, vol. 77, no. 4, p. 041101, 2006.

[49] "Hedrick, Hykes- Starchman- Ultrasound Physics and Instrumentation- Chapter 6." 4th Edition, 2006 .

[50] "Hedrick, Hykes- Starchman- Ultrasound Physics and Instrumentation- Chapter 11." 4th Edition, 2006

[51] "Hedrick, Hykes- Starchman- Ultrasound Physics and Instrumentation- Chapter 10." 4th Edition, 2006

[52] *Handbook of Medical Imaging: Display and pacs*. SPIE Press, 2000.

[53] "Hedrick, Hykes- Starchman- Ultrasound Physics and Instrumentation- Chapter 12."

[54] F. W. Kremkau, *Sonography Principles and Instruments*. Elsevier Health Sciences, 2014.

[55] G. Ku and L. V Wang, "Deeply penetrating photoacoustic tomography in biological tissues enhanced with an optical contrast agent.," *Opt. Lett.*, vol. 30, no. 5, pp. 507–9, 2005.

[56] Y. Zhang, H. Hong, and W. Cai, "Photoacoustic imaging.," *Cold Spring Harb. Protoc.*, vol. 2011, no. 9, 2011.

[57] D. Razansky, N. C. Deliolanis, C. Vinegoni, and V. Ntziachristos, “Deep tissue optical and optoacoustic molecular imaging technologies for pre-clinical research and drug discovery.,” *Curr. Pharm. Biotechnol.*, vol. 13, no. 4, pp. 504–22, 2012.

[58] J. L. Su, B. Wang, K. E. Wilson, C. L. Bayer, Y.-S. Chen, S. Kim, K. A. Homan, and S. Y. Emelianov, “Advances in Clinical and Biomedical Applications of Photoacoustic Imaging.,” *Expert Opin. Med. Diagn.*, vol. 4, no. 6, pp. 497–510, 2010.

[59] C. T. Lim and J. C. H. Goh, Eds., *13th International Conference on Biomedical Engineering*, vol. 23. Berlin, Heidelberg: Springer Berlin Heidelberg, 2009.

[60] M. Friebel, J. Helfmann, U. Netz, and M. Meinke, “Influence of oxygen saturation on the optical scattering properties of human red blood cells in the spectral range 250 to 2,000 nm.,” *J. Biomed. Opt.*, vol. 14, no. 3, p. 034001, 2009.

[61] S. A. Ermilov, T. Khamapirad, A. Conjusteau, M. H. Leonard, R. Lacewell, K. Mehta, T. Miller, and A. A. Oraevsky, “Laser optoacoustic imaging system for detection of breast cancer.,” *J. Biomed. Opt.*, vol. 14, no. 2, p. 024007, 2009.

[62] A. A. Oraevsky, “Detection, diagnostics and image-guided therapy of cancer using laser optoacoustic imaging system and gold nanoparticles,” in *The Second Asian and Pacific Rim Symposium on Biophotonics, 2004. APBP 2004.*, pp. 250–251.

[63] M. Kneipp, J. Turner, S. Hambauer, S. M. Krieg, J. Lehmberg, U. Lindauer, and D. Razansky, “Functional real-time optoacoustic imaging of middle cerebral artery occlusion in mice.,” *PLoS One*, vol. 9, no. 4, p. e96118, 2014.

[64] S. Sethuraman, J. H. Amirian, S. H. Litovsky, R. W. Smalling, and S. Y. Emelianov, "Ex vivo Characterization of Atherosclerosis using Intravascular Photoacoustic Imaging," *Opt. Express*, vol. 15, no. 25, p. 16657, 2007.

[65] S. A. Ermilov, T. Khamapirad, A. Conjusteau, M. H. Leonard, R. Lacewell, K. Mehta, T. Miller, and A. A. Oraevsky, "Laser optoacoustic imaging system for detection of breast cancer.," *J. Biomed. Opt.*, vol. 14, no. 2, p. 024007.

[66] L. Xi, S. R. Grobmyer, L. Wu, R. Chen, G. Zhou, L. G. Gutwein, J. Sun, W. Liao, Q. Zhou, H. Xie, and H. Jiang, "Evaluation of breast tumor margins *in vivo* with intraoperative photoacoustic imaging," *Opt. Express*, vol. 20, no. 8, p. 8726, 2012.

[67] X. Wang, W. W. Roberts, P. L. Carson, D. P. Wood, and J. B. Fowlkes, "Photoacoustic tomography: a potential new tool for prostate cancer.," *Biomed. Opt. Express*, vol. 1, no. 4, pp. 1117–1126, 2010.

[68] V. S. Dogra, B. K. Chinni, K. S. Valluru, J. V Joseph, A. Ghazi, J. L. Yao, K. Evans, E. M. Messing, and N. A. Rao, "Multispectral Photoacoustic Imaging of Prostate Cancer: Preliminary Ex-vivo Results.," *J. Clin. Imaging Sci.*, vol. 3, p. 41, 2013.

[69] E. De Montigny, "Photoacoustic Tomography": Principles and applications," vol. 35, no. 2007, 2010.

[70] R. I. Siphanto, K. K. Thumma, R. G. M. Kolkman, T. G. van Leeuwen, F. F. M. de Mul, J. W. van Neck, L. N. A. van Adrichem, and W. Steenbergen, "Serial noninvasive photoacoustic imaging of neovascularization in tumor angiogenesis," *Opt. Express*, vol. 13, no. 1, p. 89, 2005.

[71] G. Ku, X. Wang, X. Xie, G. Stoica, and L. Wang, "Imaging of tumor angiogenesis in rat brains *in vivo* by photoacoustic tomography," *Appl. Opt.*, vol. 44, no. 5, p. 770, 2005.

[72] A. A. Oraevsky, A. A. Karabutov, S. V. Solomatin, E. V. Savateeva, V. A. Andreev, Z. Gatalica, H. Singh, and R. D. Fleming, "Laser optoacoustic imaging of breast cancer *in vivo*," in *BiOS 2001 The International Symposium on Biomedical Optics*, 2001, pp. 6–15.

[73] Y. Lao, D. Xing, S. Yang, and L. Xiang, "Noninvasive photoacoustic imaging of the developing vasculature during early tumor growth.," *Phys. Med. Biol.*, vol. 53, no. 15, pp. 4203–12, 2008.

[74] J. Laufer, P. Johnson, E. Zhang, B. Treeby, B. Cox, B. Pedley, and P. Beard, "*In vivo* preclinical photoacoustic imaging of tumor vasculature development and therapy.," *J. Biomed. Opt.*, vol. 17, no. 5, p. 056016, 2012.

[75] H.-P. Brecht, R. Su, M. Fronheiser, S. a Ermilov, A. Conjusteau, and A. a Oraevsky, "Whole-body three-dimensional optoacoustic tomography system for small animals.," *J. Biomed. Opt.*, vol. 14, no. 6, p. 064007, 2009.

[76] R. a. Kruger, R. B. Lam, D. R. Reinecke, S. P. Del Rio, and R. P. Doyle, "Photoacoustic angiography of the breast," *Med. Phys.*, vol. 37, no. 11, p. 6096, 2010.

[77] Q. T. Bui, M. Prempeh, and R. L. Wilensky, "Atherosclerotic plaque development.," *Int. J. Biochem. Cell Biol.*, vol. 41, no. 11, pp. 2109–13, 2009.

[78] S. Sethuraman, S. R. Aglyamov, J. H. Amirian, R. W. Smalling, and S. Y. Emelianov, "Intravascular photoacoustic imaging using an IVUS imaging catheter.," *IEEE Trans. Ultrason. Ferroelectr. Freq. Control*, vol. 54, no. 5, pp. 978–86, 2007.

[79] S. Sethuraman, J. H. Amirian, S. H. Litovsky, R. W. Smalling, and S. Y. Emelianov, "Spectroscopic intravascular photoacoustic imaging to differentiate atherosclerotic plaques.," *Opt. Express*, vol. 16, no. 5, pp. 3362–7, 2008.

[80] J. Zhang, S. Yang, X. Ji, Q. Zhou, and D. Xing, “Characterization of lipid-rich aortic plaques by intravascular photoacoustic tomography: ex vivo and *in vivo* validation in a rabbit atherosclerosis model with histologic correlation.,” *J. Am. Coll. Cardiol.*, vol. 64, no. 4, pp. 385–90, 2014.

[81] X. Wang, Y. Xu, M. Xu, S. Yokoo, E. S. Fry, and L. V. Wang, “Photoacoustic tomography of biological tissues with high cross-section resolution: Reconstruction and experiment,” *Med. Phys.*, vol. 29, no. 12, p. 2799, 2002.

[82] Y.-H. Wang, A.-H. Liao, J.-H. Chen, C.-R. C. Wang, and P.-C. Li, “Photoacoustic/ultrasound dual-modality contrast agent and its application to thermotherapy.,” *J. Biomed. Opt.*, vol. 17, no. 4, p. 045001, 2012.

[83] D. Wu, L. Huang, M. S. Jiang, and H. Jiang, “Contrast Agents for Photoacoustic and Thermoacoustic Imaging": A Review,” *Int. J. Mol. Sci.*, pp. 23616–23639, 2014.

[84] X. Yi, F. Wang, W. Qin, X. Yang, and J. Yuan, “Near-infrared fluorescent probes in cancer imaging and therapy: an emerging field.,” *Int. J. Nanomedicine*, vol. 9, pp. 1347–65, 2014.

[85] S. Luo, E. Zhang, Y. Su, T. Cheng, and C. Shi, “A review of NIR dyes in cancer targeting and imaging,” *Biomaterials*, vol. 32, no. 29, pp. 7127–7138, 2011.

[86] P. K. Jain, K. S. Lee, I. H. El-Sayed, and M. A. El-Sayed, “Calculated absorption and scattering properties of gold nanoparticles of different size, shape, and composition: applications in biological imaging and biomedicine.,” *J. Phys. Chem. B*, vol. 110, no. 14, pp. 7238–48, 2006.

[87] M. Matson and A. W. Orbaek, *Inorganic Chemistry For Dummies*. Wiley, 2013.

[88] B. Nikoobakht and M. A. El-Sayed, “Preparation and Growth Mechanism of Gold Nanorods (NRs) Using Seed-Mediated Growth Method,” *Chem. Mater.*, vol. 15, no. 10, pp. 1957–1962, 2003.

[89] S. Manohar, C. Ungureanu, and T. G. Van Leeuwen, “Gold nanorods as molecular contrast agents in photoacoustic imaging: the promises and the caveats.,” *Contrast Media Mol. Imaging*, vol. 6, no. 5, pp. 389–400, 2011.

[90] M. Eghtedari, A. Oraevsky, J. a. Copland, N. a. Kotov, A. Conjusteau, and M. Motamedi, “High sensitivity of *in vivo* detection of gold nanorods using a laser optoacoustic imaging system,” *Nano Lett.*, vol. 7, pp. 1914–1918, 2007.

[91] Y. Wang, X. Xie, X. Wang, G. Ku, K. L. Gill, D. P. O’Neal, G. Stoica, and L. V. Wang, “Photoacoustic Tomography of a Nanoshell Contrast Agent in the *in Vivo* Rat Brain,” *Nano Lett.*, vol. 4, no. 9, pp. 1689–1692, 2004.

[92] L. Xiang, H. Gu, D. Yang, L. Zeng, and S. Yang, “Gold nanoshell-based photoacoustic imaging application in biomedicine,” in *2006 International Symposium on Biophotonics, Nanophotonics and Metamaterials*, 2006, pp. 76–79.

[93] J. R. Cole, N. A. Mirin, M. W. Knight, G. P. Goodrich, and N. J. Halas, “Photothermal Efficiencies of Nanoshells and Nanorods for Clinical Therapeutic Applications,” *J. Phys. Chem. C*, vol. 113, no. 28, pp. 12090–12094, 2009.

[94] J. E. Millstone, S. J. Hurst, G. S. Métraux, J. I. Cutler, and C. A. Mirkin, “Colloidal gold and silver triangular nanoprisms.,” *Small*, vol. 5, no. 6, pp. 646–64, 2009.

[95] D. Pan, M. Pramanik, S. A. Wickline, L. V Wang, and G. M. Lanza, "Recent advances in colloidal gold nanobeacons for molecular photoacoustic imaging.," *Contrast Media Mol. Imaging*, vol. 6, no. 5, pp. 378–88, Jan. .

[96] G. M. Lanza, "Emerging contrast agents for photoacoustic imaging.," *Contrast Media Mol. Imaging*, vol. 6, no. 5, p. 331.

[97] A. De la Zerda, C. Zavaleta, S. Keren, S. Vaithilingam, S. Bodapati, Z. Liu, J. Levi, B. R. Smith, T.-J. Ma, O. Oralkan, Z. Cheng, X. Chen, H. Dai, B. T. Khuri-Yakub, and S. S. Gambhir, "Carbon nanotubes as photoacoustic molecular imaging agents in living mice.," *Nat. Nanotechnol.*, vol. 3, no. 9, pp. 557–62, 2008.

[98] J.-W. Kim, E. I. Galanzha, E. V Shashkov, H.-M. Moon, and V. P. Zharov, "Golden carbon nanotubes as multimodal photoacoustic and photothermal high-contrast molecular agents.," *Nat. Nanotechnol.*, vol. 4, no. 10, pp. 688–94, 2009.

[99] A. de la Zerda, Z. Liu, S. Bodapati, R. Teed, S. Vaithilingam, B. T. Khuri-Yakub, X. Chen, H. Dai, and S. S. Gambhir, "Ultrahigh sensitivity carbon nanotube agents for photoacoustic molecular imaging in living mice.," *Nano Lett.*, vol. 10, no. 6, pp. 2168–72, 2010.

[100] E. Stride and N. Saffari, "Microbubble ultrasound contrast agents: a review.," *Proc. Inst. Mech. Eng. H.*, vol. 217, pp. 429–47, 2003.

[101] J. Jian, C. Liu, Y. Gong, L. Su, B. Zhang, Z. Wang, D. Wang, Y. Zhou, F. Xu, P. Li, Y. Zheng, L. Song, and X. Zhou, "India Ink Incorporated Multifunctional Phase-transition Nanodroplets for Photoacoustic/Ultrasound Dual-modality Imaging and Photoacoustic Effect Based Tumor Therapy.," *Theranostics*, vol. 4, no. 10, pp. 1026–38, 2014.

[102] A. R. Siekkinen, J. M. McLellan, J. Chen, and Y. Xia, “Rapid synthesis of small silver nanocubes by mediating polyol reduction with a trace amount of sodium sulfide or sodium hydrosulfide.,” *Chem. Phys. Lett.*, vol. 432, no. 4–6, pp. 491–496, 2006.

[103] S. E. Skrabalak, L. Au, X. Lu, X. Li, and Y. Xia, “Gold nanocages for cancer detection and treatment.,” *Nanomedicine (Lond).*, vol. 2, no. 5, pp. 657–68, 2007.

[104] W. Li, P. K. Brown, L. V Wang, and Y. Xia, “Gold nanocages as contrast agents for photoacoustic imaging.,” *Contrast Media Mol. Imaging*, vol. 6, no. 5, pp. 370–7.

[105] M. Hu, J. Chen, Z.-Y. Li, L. Au, G. V Hartland, X. Li, M. Marquez, and Y. Xia, “Gold nanostructures: engineering their plasmonic properties for biomedical applications.,” *Chem. Soc. Rev.*, vol. 35, no. 11, pp. 1084–94, 2006.

[106] Y. Xia, “Gold nanocages for optical imaging and therapeutic applications,” Communications and Photonics Conference and Exhibition (ACP), 2009 Asia, IEEE.

[107] J. Chen, B. Wiley, Z.-Y. Li, D. Campbell, F. Saeki, H. Cang, L. Au, J. Lee, X. Li, and Y. Xia, “Gold Nanocages: Engineering Their Structure for Biomedical Applications,” *Adv. Mater.*, vol. 17, no. 18, pp. 2255–2261, 2005.

[108] J. Chen, F. Saeki, B. J. Wiley, H. Cang, M. J. Cobb, Z. Li, L. Au, H. Zhang, and M. B. Kimmey, “Gold Nanocages": Bioconjugation and Their Potential Use as Optical Imaging Contrast Agents,” pp. 1–5, 2005.

[109] K. Carroll, “Core-Shell Nanoparticles": Synthesis , Design , and Characterization,” 2010. Phd Thesis.

[110] K. J. Carroll, M. D. Shultz, P. P. Fatouros, and E. E. Carpenter, “High magnetization aqueous ferrofluid: A simple one-pot synthesis,” *J. Appl. Phys.*, vol. 107, pp. 5–7, 2010.

[111] R. Esparza, A. F. García-Ruiz, J. J. V. Salazar, R. Pérez, and M. José-Yacamán, "Structural characterization of Pt-Pd core-shell nanoparticles by Cs-corrected STEM.," *J. Nanopart. Res.*, vol. 15, no. 1342, 2012.

[112] N. Linares, A. M. Silvestre-Albero, E. Serrano, J. Silvestre-Albero, and J. Garcia-Martinez, "Mesoporous materials for clean energy technologies," *Chem. Soc. Rev.*, pp. 7681–7717, 2014.

[113] H. Yoon, A. Xu, G. E. Sterbinsky, D. a. Arena, Z. Wang, P. W. Stephens, Y. S. Meng, and K. J. Carroll, "In situ non-aqueous nucleation and growth of next generation rare-earth-free permanent magnets," *Phys. Chem. Chem. Phys.*, vol. 17, pp. 1070–1076, 2015.

[114] A. Anzlovar, Z. C. Orel, and M. Zigon, "Morphology and particle size of di(ethylene glycol) mediated metallic copper nanoparticles.," *J. Nanosci. Nanotechnol.*, vol. 8, no. 7, pp. 3516–25, 2008.

[115] Y. Sun, B. Mayers, T. Herricks, and Y. Xia, "Polyol Synthesis of Uniform Silver Nanowires: A Plausible Growth Mechanism and the Supporting Evidence," *Nano Lett.*, vol. 3, no. 7, pp. 955–960, 2003.

[116] D. Larcher and R. Patrice, "Preparation of Metallic Powders and Alloys in Polyol Media: A Thermodynamic Approach," *J. Solid State Chem.*, vol. 154, no. 2, pp. 405–411, 2000.

[117] Y. Hou, H. Kondoh, T. Ohta, and S. Gao, "Size-controlled synthesis of nickel nanoparticles," *Appl. Surf. Sci.*, vol. 241, no. 1–2, pp. 218–222, 2005.

[118] "Rapid synthesis of small silver nanocubes by mediating polyol reduction with a trace amount of sodium sulfide or sodium hydrosulfide." http://www.biomedsearch.com/nih/Rapid-synthesis-small-silver-nanocubes/18496589.html.

[119] F. Fievet, J. P. Lagier, and M. Figlarz, "Preparing Monodisperse Metal Powders in Micrometer and Submicrometer Sizes by the Polyol Process," *MRS Bull.*, vol. 14, no. 12, pp. 29–34, 2013.

[120] C. Ducamp-Sanguesa, R. Herrera-Urbina, and M. Figlarz, "Synthesis and characterization of fine and monodisperse silver particles of uniform shape," *J. Solid State Chem.*, vol. 100, no. 2, pp. 272–280, 1992.

[121] P.-Y. Silvert, R. Herrera-Urbina, and K. Tekaia-Elhsissen, "Preparation of colloidal silver dispersions by the polyol process," *J. Mater. Chem.*, vol. 7, no. 2, pp. 293–299, 1997.

[122] R. Seshadri and C. N. R. Rao, "Preparation of monodispersed, submicron gold particles," *Mater. Res. Bull.*, vol. 29, no. 7, pp. 795–799, 1994.

[123] K. Meguro and K. Esumi, The preparation of colloidal precious metal particles using copolymers of vinyl alcohol-N-Vinylpyrrolidone. Bull.chem.soc.jpn., 61, 347-350 , 1988.

[124] E. G. Campari and G. Levi, "Physical Journal B," vol. 166, pp. 159–166, 2000.

[125] G. Carotenuto, G.P. Pepe, and L. Nicolais, Preparation and characterization of nano-sized Ag/PVP composites for optical applications. Eur. Phys. J. B 16, 2000.

[126] A. Henglein, "Physicochemical properties of small metal particles in solution: 'microelectrode' reactions, chemisorption, composite metal particles, and the atom-to-metal transition," *J. Phys. Chem.*, vol. 97, no. 21, pp. 5457–5471, 1993.

[127] S. M. Heard, F. Grieser, C. G. Barraclough, and J. V Sanders, "The characterization of ag sols by electron microscopy, optical absorption, and electrophoresis," *J. Colloid Interface Sci.*, vol. 93, no. 2, pp. 545–555, 1983.

[128] B. Wiley, Y. Sun, B. Mayers, and Y. Xia, “Shape-controlled synthesis of metal nanostructures: the case of silver.,” *Chemistry*, vol. 11, no. 2, pp. 454–63, 2005.

[129] Y. Sun and Y. Xia, “Shape-controlled synthesis of gold and silver nanoparticles.,” *Science*, vol. 298, no. 5601, pp. 2176–9, 2002.

[130] J. Dundurs, L. D. Marks, and P. M. Ajayan, “Structural fluctuations in small particles,” vol. 57, no. 4, pp. 605–620, 1988.

[131] Z. L. Wang, “Transmission Electron Microscopy of Shape-Controlled Nanocrystals and Their Assemblies,” *J. Phys. Chem. B*, vol. 104, no. 6, pp. 1153–1175, 2000.

[132] “Controlled Nanofabrication: Advances and Applications: Liu Ru-Shi: 9789814316873: Books Amazon.ca.” http://www.amazon.ca/Controlled-Nanofabrication-Applications-Liu-Ru-Shi/dp/9814316873.

[133] X. Lu, J. Chen, S. E. Skrabalak, and Y. Xia, “Galvanic replacement reaction: a simple and powerful route to hollow and porous metal nanostructures,” *Proc. Inst. Mech. Eng. Part N J. Nanoeng. Nanosyst.*, vol. 221, no. 1, pp. 1–16, 2007.

[134] Z. S. Smialowska, *Pitting Corrosion of Metals*. National Assn of Corrosion Engineers, 1986. McGraw-Hill

[135] S. K. Wonnell, J. M. Delaye, M. Bibolé, and Y. Limoge, “Activation volume for the interdiffusion of Ag-Au multilayers,” *J. Appl. Phys.*, vol. 72, no. 11, p. 5195, 1992.

[136] T. Shibata, B. A. Bunker, Z. Zhang, D. Meisel, C. F. Vardeman, and J. D. Gezelter, “Size-Dependent Spontaneous Alloying of Au−Ag Nanoparticles,” *J. Am. Chem. Soc.*, vol. 124, no. 40, pp. 11989–11996, 2002.

[137] X. Lu, J. Chen, S. E. Skrabalak, and Y. Xia, “Galvanic replacement reaction: a simple and powerful route to hollow and porous metal nanostructures,” *Proc. Inst. Mech. Eng. Part N J. Nanoeng. Nanosyst.*, vol. 221, no. 1, pp. 1–16, 2007.

[138] Bukaluk, “Auger electron spectroscopy investigations of the effect of degradation of depth resolution and its influence on the interdiffusion data in thin film Au/Ag, Cu/Ag, Pd/Au and Pd/Cu multilayer structures,” *Appl. Surf. Sci.*, vol. 175–176, pp. 790–796, 2001.

[139] A. Bukaluk, “Auger electron spectroscopy investigations of the effect of degradation of depth resolution and its influence on the interdiffusion data in thin film Au/Ag, Cu/Ag, Pd/Au and Pd/Cu multilayer structures,” *Appl. Surf. Sci.*, vol. 175–176, pp. 790–796, 2001.

[140] W. Mallard, A. Gardner, R. Bass, and L. Slifkin, “Self-Diffusion in Silver-Gold Solid Solutions,” *Phys. Rev.*, vol. 129, no. 2, pp. 617–625, 1963.

[141] Y. Sun, B. T. Mayers, and Y. Xia, “Template-Engaged Replacement Reaction: A One-Step Approach to the Large-Scale Synthesis of Metal Nanostructures with Hollow Interiors,” *Nano Lett.*, vol. 2, no. 5, pp. 481–485, 2002.

[142] J. Erlebacher, M. J. Aziz, A. Karma, N. Dimitrov, and K. Sieradzki, “Evolution of nanoporosity in dealloying.,” *Nature*, vol. 410, no. 6827, pp. 450–3, 2001.

[143] T. Shahrabi, “Stress-Corrosion Cracking of Alpha-Brass Without Copper Oxidation,” *J. Electrochem. Soc.*, vol. 140, no. 2, p. 348, 1993.

[144] A. R. Roosen and W. C. Carter, “Simulations of microstructural evolution: anisotropic growth and coarsening,” *Phys. A Stat. Mech. its Appl.*, vol. 261, no. 1–2, pp. 232–247, 1998.

[145] A. R. Siekkinen, J. M. McLellan, J. Chen, and Y. Xia, "Rapid synthesis of small silver nanocubes by mediating polyol reduction with a trace amount of sodium sulfide or sodium hydrosulfide.," *Chem. Phys. Lett.*, vol. 432, no. 4–6, pp. 491–496, 2006.

[146] S. E. Skrabalak, L. Au, X. Li, and Y. Xia, "Facile synthesis of Ag nanocubes and Au nanocages.," *Nat. Protoc.*, vol. 2, no. 9, pp. 2182–90, 2007.

[147] Q. Zhang, W. Li, L.-P. Wen, J. Chen, and Y. Xia, "Facile synthesis of Ag nanocubes of 30 to 70 nm in edge length with CF(3)COOAg as a precursor.," *Chemistry*, vol. 16, no. 33, pp. 10234–9, 2010.

[148] T. Theivasanthi and M. Alagar, "Electrolytic Synthesis and Characterizations of Silver Nanopowder." Nano BiomedEng. 4 (2) 58-65, 2012.

[149] R. Varshney, S. Bhadauria, and M. S. Gaur, "Biogenic synthesis of silver nanocubes and nanorods using sundried Stevia rebaudiana leaves," *Adv. Mater. Lett.*, vol. 1, no. 3, pp. 232–237, 2010.

[150] A. S. Lanje, S. J. Sharma, and R. B. Pode, "Synthesis of silver nanoparticles: a safer alternative to conventional antimicrobial & antibacterial agents," journal of Chemical and Pharmaceutical Research vol. 2, no. 3, pp. 478–483, 2010.

[151] Y. K. Du, P. Yang, Z. G. Mou, N. P. Hua, and L. Jiang, "Thermal decomposition behaviors of PVP coated on platinum nanoparticles," *J. Appl. Polym. Sci.*, vol. 99, no. 1, pp. 23–26, 2006.

[152] "ANSI Z136 Standards - LIA." https://www.lia.org/store/ANSI+Z136+Standards.

[153] Laser Institue of America, "American National Standard for Safe Use of Lasers ANSI Z136.1—2014," *Laser Inst. Am. Orlando*, 2014.

[154] “Ultrasound Physics and Instrumentation, 4e: Wayne R. Hedrick, David L. Hykes, Dale E. Starchman: 9780323032124: Books - Amazon.ca.” http://www.amazon.ca/Ultrasound-Physics-Instrumentation-Wayne-Hedrick/dp/0323032125.

[155] C. Langton, “Signal Processing & Simulation Newsletter,” *URL http//www. complextoreal. com/tcomplex. htm*, vol. 707, pp. 1–7, 2003.

[156] A. Plech, V. Kotaidis, S. Grésillon, C. Dahmen, and G. von Plessen, “Laser-induced heating and melting of gold nanoparticles studied by time-resolved x-ray scattering,” *Phys. Rev. B*, vol. 70, no. 19, p. 195423, 2004.

[157] Y.-S. Chen, W. Frey, S. Kim, K. Homan, P. Kruizinga, K. Sokolov, and S. Emelianov, “Enhanced thermal stability of silica-coated gold nanorods for photoacoustic imaging and image-guided therapy.,” *Opt. Express*, vol. 18, no. 9, pp. 8867–8878, 2010.

[158] “Gold Nanoparticles: Properties and Applications Sigma-Aldrich.” http://www.sigmaaldrich.com/materials-science/nanomaterials/gold-nanoparticles.html.

[159] S. Link, C. Burda, B. Nikoobakht, and M. A. El-Sayed, “Laser-Induced Shape Changes of Colloidal Gold Nanorods Using Femtosecond and Nanosecond Laser Pulses,” *J. Phys. Chem. B*, vol. 104, no. 26, pp. 6152–6163, 2000.

[160] M. Gordel, J. Olesiak-banska, and K. Matczyszyn, “femtosecond laser,” pp. 71–78, 2014.

[161] S. Link, C. Burda, M. B. Mohamed, B. Nikoobakht, and M. A. El-Sayed, “Laser Photothermal Melting and Fragmentation of Gold Nanorods: Energy and Laser Pulse-Width Dependence,” *J. Phys. Chem. A*, vol. 103, no. 9, pp. 1165–1170, 1999.

[162] S.S. Chang, C.-W. Shih, C.-D. Chen, W.-C. Lai, and C. R. C. Wang, “The Shape Transition of Gold Nanorods,” *Langmuir*, vol. 15, no. 3, pp. 701–709, 1999.

[163] M. B. Mohamed, K. Z. Ismail, S. Link, and M. A. El-Sayed, "Thermal Reshaping of Gold Nanorods in Micelles," *J. Phys. Chem. B*, vol. 102, no. 47, pp. 9370–9374, 1998.

[164] H. Petrova, J. Perez Juste, I. Pastoriza-Santos, G. V Hartland, L. M. Liz-Marzán, and P. Mulvaney, "On the temperature stability of gold nanorods: comparison between thermal and ultrafast laser-induced heating.," *Phys. Chem. Chem. Phys.*, vol. 8, no. 7, pp. 814–21, 2006.

[165] G. Schmid and B. Corain, "Nanoparticulated Gold: Syntheses, Structures, Electronics, and Reactivities," *Eur. J. Inorg. Chem.*, vol. 2003, no. 17, pp. 3081–3098, 2003.

[166] J. R. Cook, R. R. Bouchard, and S. Y. Emelianov, "Tissue-mimicking phantoms for photoacoustic and ultrasonic imaging.," *Biomed. Opt. Express*, vol. 2, no. 11, pp. 3193–206, 2011.

[167] W. F. Cheong, S. a. S. Prahl, and a. J. A. Welch, "A review of the optical properties of biological tissues," *IEEE journal of quantum electronics*, vol. 26. pp. 2166–2185, 1990.

[168] A. Roggan, M. Friebel, K. Do Rschel, A. Hahn, and G. Mu Ller, "Optical Properties of Circulating Human Blood in the Wavelength Range 400-2500 nm.," *J. Biomed. Opt.*, vol. 4, no. 1, pp. 36–46, 1999.

[169] C. J. Moes, M. J. van Gemert, W. M. Star, J. P. Marijnissen, and S. A. Prahl, "Measurements and calculations of the energy fluence rate in a scattering and absorbing phantom at 633 nm.," *Appl. Opt.*, vol. 28, no. 12, pp. 2292–6, 1989.

[170] A. M. De Grand, S. J. Lomnes, D. S. Lee, M. Pietrzykowski, S. Ohnishi, T. G. Morgan, A. Gogbashian, R. G. Laurence, and J. V Frangioni, "Tissue-like phantoms for near-infrared fluorescence imaging system assessment and the training of surgeons.," *J. Biomed. Opt.*, vol. 11, no. 1, p. 014007.

[171] J. R. Cook, R. R. Bouchard, and S. Y. Emelianov, "Tissue-mimicking phantoms for photoacoustic and ultrasonic imaging," vol. 2, no. 11, pp. 2243–2254, 2011.

[172] P. C. Beard and T. N. Mills, "2D line-scan photoacoustic imaging of absorbers in a scattering tissue phantom," in *BiOS 2001 The International Symposium on Biomedical Optics*, 2001, pp. 34–42.

[173] S. Grabtchak, T. J. Palmer, F. Foschum, A. Liemert, A. Kienle, and W. M. Whelan, "Experimental spectro-angular mapping of light distribution in turbid media.," *J. Biomed. Opt.*, vol. 17, no. 6, p. 067007, 2012.

[174] C. Kim, K. H. Song, F. Gao, and L. V Wang, "Sentinel Lymph Nodes and Lymphatic Vessels: Noninvasive Dual-Modality *in Vivo* Mapping by Using Indocyanine Green in Rats Volumetric Spectroscopic Photoacoustic Imaging and Planar Purpose: Methods: Results:," vol. 255, no. 2, 2010.

[175] S. Grabtchak, L. G. Montgomery, and W. M. Whelan, "Optical absorption and scattering properties of bulk porcine muscle phantoms from interstitial radiance measurements in 650-900 nm range.," *Phys. Med. Biol.*, vol. 59, no. 10, pp. 2431–44, 2014.

[176] Y. S. Zhang, Y. Wang, L. Wang, Y. Wang, X. Cai, C. Zhang, L. V Wang, and Y. Xia, "Labeling human mesenchymal stem cells with gold nanocages for in vitro and *in vivo* tracking by two-photon microscopy and photoacoustic microscopy.," *Theranostics*, vol. 3, no. 8, pp. 532–43, 2013.

[177] Q. Zhang, N. Iwakuma, P. Sharma, B. M. Moudgil, C. Wu, J. McNeill, H. Jiang, and S. R. Grobmyer, "Gold nanoparticles as a contrast agent for *in vivo* tumor imaging with photoacoustic tomography.," *Nanotechnology*, vol. 20, p. 395102, 2009.

[178] J. Chen, D. Wang, J. Xi, L. Au, A. Siekkinen, A. Warsen, Z. Y. Li, H. Zhang, Y. Xia, and X. Li, "Immuno gold nanocages with tailored optical properties for targeted photothermal destruction of cancer cells," *Nano Lett.*, vol. 7, pp. 1318–1322, 2007.

[179] S. A. Khan, R. Kanchanapally, Z. Fan, L. Beqa, A. K. Singh, D. Senapati, and P. C. Ray, "A gold nanocage–CNT hybrid for targeted imaging and photothermal destruction of cancer cells," *Chem. Commun.*, vol. 48, p. 6711, 2012.

Appendix : Matlab scripts

Appendix A: Load command

```
%THIS FILE SHOULD BE FOUND IN THE SAME FOLDER AS BETA_BEAMFORMING
%clear
%The purpose of this script is to load the data of an image of one
%wavelength (TiS or YAG). MatLab should be in a directory such that there is
only one
%folder of one wavelength in that directory. The script will also make a
%Hilbert Transform of the data.


%clear


%Parameters
xMax=601;
zMax=1;
MaxX_MaxZvalue=1;
totalscans=(xMax-1)*zMax+MaxX_MaxZvalue;


%Find subfolders. Returns directories, and excludes the '.' and '..'
A = dirc(cd, 'de');
A = A(:,1);


%Sort subfolders (considers embeded numerical order)
[folders b] = sort_nat(A)


%Number of Folders
[a b] = size(folders)


%Current Directory
B= cd
```

```
%Build Directory folder to be loaded

C = '\'

D = folders{1}

E = strcat(B,C, D)



%select data directory

directory_name = E


%This is the script that was taken from the SENO DATA ANALYSIS GUI

%

% Check to see which directory was selected

if ~isvector(strfind(directory_name, '_TiS')) &
~isvector(strfind(directory_name, '_wl2'))

    % this data is wavelength 1

    wl1 = 1;

else

    % This data is wavelength 2

    wl1 = 0;

end


data_files = dir(directory_name);

[pathstr, name, ext, versn] = fileparts(directory_name);

% Load the input_params structure from the first file

acquired_data = [];

load(fullfile(directory_name, data_files(3).name), 'input_params',
'acquired_data');

input_params.parent_folder = pathstr;

input_params.folder_VV = [directory_name '_VV']; %folder for volview
visualization

%[status,message,messageid] = mkdir(input_params.folder_VV);

%input_params.filt = 1; %post-beamforming filtering (None)

input_params.scan_step = input_params.scan_res;
```

```
input_params.Ymax =
input_params.sampling_distance*(input_params.samples_complete - 1); %maximum
distance from the transducer for a single A-line (used in scaling of A-lines)


start_location = 0; %start location (mm)


MaxZ=zMax;

annular_array_data = zeros(xMax, input_params.scan_steps(3),
input_params.no_channels_used, input_params.samples, 'single');

beams = zeros(totalscans, input_params.samples, 'single');

count=0;

for indexx = 1:xMax

    if indexx==xMax;

        zMax=MaxX_MaxZvalue;

    end

    for indexz = 1:zMax

        count=count+1;

        disp(['Loading ' num2str(count) ' out of '
num2str(input_params.scan_steps(1)*input_params.scan_steps(3))]);

        % Here build the filename to load:

        individual_filename = [input_params.filename_rasterscan '_X'
num2str(indexx,'%04.0f') 'Y0001Z' num2str(indexz,'%04.0f') '.mat'];

        if wl1

            individual_file_data = load(fullfile(input_params.parent_folder,
input_params.directory_rasterscan, individual_filename), 'input_params',
'acquired_data');

        else

            individual_file_data = load(fullfile(input_params.parent_folder,
input_params.directory_rasterscan2, individual_filename), 'input_params',
'acquired_data');

        end

        for index_annular_element = 1:input_params.no_channels_used

            annular_array_data(indexx,indexz, index_annular_element, :)  = ...


permute(individual_file_data.acquired_data(index_annular_element, :), [2 1]);

        end

        clear individual_file_data


%%%%%%%%%%%%%%%%%%%%%%%%%%%%%%%%%%%%%%%%%%%%%%%%%%%%%%%%%%%%%%%%%%%%%%%%%%%%
```

```
        %optional beamforming
        input_data = squeeze(annular_array_data(indexx,indexz,:,:));
        OA_data = Beta_beamforming(input_params,input_data);
        indexzfix=(indexx-1)*MaxZ+indexz;
        beams(indexzfix, :) = OA_data(1,:);
%%%%%%%%%%%%%%%%%%%%%%%%%%%%%%%%%%%%%%%%%%%%%%%%%%%%%%%%%%%%%%%%%%%%%%%%%%%%%%%%
%%%%%%%%%%%%%%%%%%%%%%%%%%%%%%%%%%%%%%%%%%%%
    end
end


dimens = size(beams);
spacing = input_params.scan_step;
totalpoints = dimens(1)*dimens(2)*1 %dimens(3);
%End of Seno Loading



%Change orrientation of beams 3D matrix
%beams = permute(beams,[1 3 2]);


%Perform Hilbert Transform of 3D matrix and call resulting matrix Hilbt
[q, s] = size(beams)


for x = 1:q


Hilbt(x, :) = abs(hilbert(beams(x, :)));


end;
```

Appendix B: Beta beam forming

```
function [OA_data] = Beta_beamforming(input_params,acquired_data)


array_element_ximvals = zeros(input_params.no_channels_used,1); %x-coordinates
of the rings

array_element_zimvals = zeros(input_params.no_channels_used,1); %z-coordinates
of the rings

radius_of_ring = zeros(input_params.no_channels_used, 1); %radius value for
the ring

z_displacement_of_ring = zeros(input_params.no_channels_used, 1); %time
direction offset due to curved array

curvature_radius = input_params.focus; %(mm) radius of curvature


for index_element = 2:input_params.no_channels_used %


    radius_of_ring(index_element)                                          =
mean(input_params.annular_diameters(index_element,:))/2; %(mm)

    z_displacement_of_ring(index_element) = curvature_radius - ...

        sqrt(curvature_radius2 - radius_of_ring(index_element)2); %(mm)


    array_element_ximvals(index_element) = radius_of_ring(index_element);
%(mm)

    array_element_zimvals(index_element)                                   =
z_displacement_of_ring(index_element); %(mm)

end


OA_data = acquired_data(1,:); %initialization of the formed beam as the signal
from the central transducer


for index_sample = 1:input_params.samples

    % Here calculate the distance (d) of the given sample on the given beam

    % (there is only one beam for annular arrays)

    d          =          (input_params.added_samples+index_sample          -
1)*input_params.sampling_distance; %(mm)

    Nrings_used = 1; %number of rings used in reconstruction
```

```
    for index_channel = 2:input_params.no_channels_used

        % Now calculate the f# condition

        if    (    d    /    (2    *    array_element_ximvals(index_channel))    >
input_params.fnumber_cutoff)

            % First calculate the distance between [beam_sample_x_position

            % beam_sample_z_position] and the channel base

            distance_from_beam_sample_to_channel_base =
sqrt(array_element_ximvals(index_channel)2 + ...

                (d - array_element_zimvals(index_channel))2);

            samples_from_channel_data = round(
distance_from_beam_sample_to_channel_base / input_params.sampling_distance)-
input_params.added_samples+1;

            if (samples_from_channel_data <= input_params.samples)

                OA_data(index_sample) = ...

                    OA_data(index_sample) + ...

                    acquired_data(index_channel,samples_from_channel_data);

                Nrings_used = Nrings_used+1; %used another ring

            end % if (round( distance_from_beam_sample_to_channel_base *
input_params.fs / input_params.c) <= input_params.samples - shift)

        end % if ( d / (2 * channel_aperture_distance) <
input_params_temp.array_SE_fnumber_cutoff)

    end %     for index_channel = channel_start:channel_stop

    OA_data(index_sample) = OA_data(index_sample)/Nrings_used; %normalize
signal to the number of rings used

End
```

Appendix C: Plot Hilbert

```
t=25; %time measurement
d1=22; %distance(mm) 0.0385 is min
d2=30; %distance(mm) 59.136 is max
step=1; %x-axis step size (mm)



%%%%%%%%%%%%%%%%%%%%%%%%%%%%%%%%%%%%%%%%%%%%%%%%%%%%%%%%%%%%
x1=int32(d1/.0385); %convert distance to slices (mm)
x2=int32(d2/.0385); %convert distance to slices (mm)



%plot(Normbeams(t,:));          % to print all slices
%set(gca, 'XTick',0:150:1600,'XTickLabel',0:150*0.0385:1600*0.0385);
figure
plot(HilbtSAMPLE(t,x1:x2));     %for selectected slices
%set(gca, 'XTick',1:int32(step/.0385):x2-x1+1,'XTickLabel',d1:step:d2);
xlabel('Distance (mm)');        %sets the label of the x axis
ylabel('OA Signal (AU)');       %sets the label of y axis
%grid on % for grid

axis([0,x2-x1,-10,150]);        %set the limits of x & y axis
```

Appendix D: Plot integrated area

```
t=200 %time measurement
d1=25; %distance(mm) 0.0385 is min
d2=30; %distance(mm) 59.136 is max
step=3; %x-axis step size (mm)



x1=int32(d1/.0385); %convert distance to slices (mm)
x2=int32(d2/.0385); %convert distance to slices (mm)



plot(Hilbt(t,x1:x2));
set(gca, 'XTick',1:int32(step/.0385):x2-x1+1,'XTickLabel',d1:step:d2);
xlabel('Distance (mm)');        %sets the label of the x axis
ylabel('OA Signal (AU)');       %sets the label of y axis

area=sum(Hilbt(t,x1:x2))*0.0385



axis([0 130 0 0.4]);
%grid on
```

Appendix E: Plot beams

```
t=200 %time measurement
d1=1; %distance(mm) 0.0385 is min
d2=50; %distance(mm) 59.136 is max
step=3; %x-axis step size (mm)


x1=int32(d1/.0385); %convert distance to slices (mm)
x2=int32(d2/.0385); %convert distance to slices (mm)


plot(beams(t,x1:x2));
set(gca, 'XTick',1:int32(step/.0385):x2-x1+1,'XTickLabel',d1:step:d2);
xlabel('Distance (mm)');       %sets the label of the x axis
ylabel('OA Signal (AU)');      %sets the label of y axis


axis([0 1273 0.5 -0.05]);
```

Appendix F: One Way ANOVA (5 mJ Energy)

Comparison for nanocages scores for 5 mJ

The GLM Procedure

Class Level Information		
Class	**Levels**	**Values**
initfin	2	1 2

Number of Observations Read	180
Number of Observations Used	180

Dependent Variable: score5mj

Source	DF	Sum of Squares	Mean Square	F Value	Pr > F
Model	3	0.19327200	0.06442400	38.80	<.0001
Error	176	0.29225740	0.00166055		
Corrected Total	179	0.48552940			

R-Square	Coeff Var	Root MSE	score5mJ Mean
0.398064	5.970689	0.040750	0.682499

Source	DF	Type I SS	Mean Square	F Value	Pr > F
initfin	1	0.15711736	0.15711736	94.62	<.0001
exp	1	0.03333000	0.03333000	20.07	<.0001
sample	1	0.00282464	0.00282464	1.70	0.1939

Source	DF	Type III SS	Mean Square	F Value	Pr > F
initfin	1	0.15711736	0.15711736	94.62	<.0001
exp	1	0.03333000	0.03333000	20.07	<.0001
sample	1	0.00282464	0.00282464	1.70	0.1939

Appendix G: One Way ANOVA (10 mJ Energy)

Comparison for nanocages scores for 10 mJ

The GLM Procedure

Class Level Information		
Class	**Levels**	**Values**
initfin	2	1 2

Number of Observations Read	160
Number of Observations Used	160

Dependent Variable: score10mj

Source	DF	Sum of Squares	Mean Square	F Value	Pr > F
Model	3	0.42880206	0.14293402	55.35	<.0001
Error	156	0.40281761	0.00258216		
Corrected Total	159	0.83161967			

R-Square	Coeff Var	Root MSE	score10mj Mean
0.515623	11.43444	0.050815	0.444403

Source	DF	Type I SS	Mean Square	F Value	Pr > F
initfin	1	0.39058605	0.39058605	151.26	<.0001
exp	1	0.02419358	0.02419358	9.37	0.0026
sample	1	0.01402244	0.01402244	5.43	0.0211

Source	DF	Type III SS	Mean Square	F Value	Pr > F
initfin	1	0.39058605	0.39058605	151.26	<.0001
exp	1	0.01538038	0.01538038	5.96	0.0158
sample	1	0.01402244	0.01402244	5.43	0.0211